



The author(s) shown below used Federal funding provided by the U.S. Department of Justice to prepare the following resource:

Document Title: Identification of Minor Dye Components of Fibers via Integrating-Cavity-Enhanced Raman Spectroscopy

Author(s): Hergen Eilers, Ph.D.

Document Number: 305810

Date Received: January 2023

Award Number: 2018-DU-BX-0178

This resource has not been published by the U.S. Department of Justice. This resource is being made publicly available through the Office of Justice Programs' National Criminal Justice Reference Service.

Opinions or points of view expressed are those of the author(s) and do not necessarily reflect the official position or policies of the U.S. Department of Justice.

FINAL RESEARCH REPORT

Prepared by: Dr. Hergen Eilers

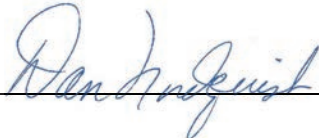
Federal Agency and Organization Element to Which the Report is Submitted	Department of Justice National Institute of Justice
Federal Grant or Other Identifying Number Assigned by Agency	2018-DU-BX-0178
Project Title	Identification of Minor Dye Components of Fibers via Integrating-Cavity-Enhanced Raman Spectroscopy
Project Director	Dr. Hergen Eilers Research Professor & Associate Director eilers@wsu.edu 509-358-7681
Name of Submitting Official, Title and Contact Information (e-mail address and Phone number), if other than PD/PI	Dan Nordquist Associate Vice President Office of Research Support & Operations orso@wsu.edu 509-335-9661
Submission Date	30 June 2022
DUNS	
EIN	
Recipient Organization	Washington State University PO Box 641060 Pullman, WA 99164-1060
Recipient Identifying Number or Account Number, if any	ORSO - 131506
Project/Grant Period	01/01/2019 to 06/30/2022
Reporting Period End Date	06/30/2022
Report Term	Final
Final Report	Yes
Signature of Submitting Official (signature shall be submitted in accordance with agency-specific instructions)	

Table of Contents

EXECUTIVE SUMMARY 9

ACCOMPLISHMENTS 11

 What are the major goals of the project? 11

 What was accomplished under these goals? 13

 PREPARATION AND CHARACTERIZATION OF DYED FABRIC SAMPLES..... 13

 Quality control (QC) of commercial dye by high-resolution mass spectroscopy 13

 Production of single-color and black fabrics with disperse and acid dyes..... 18

 Detection of disperse dye from polyester fabrics via Direct Analysis of Real-Time (DART) and
 Quadrupole Time-Of-Flight (QTOF) mass spectrometry 22

 Production of single-color, dichromatic trichromatic fabrics with disperse and reactive dyes..... 25

 Direct Analysis on Real-Time (DART) mass spectrometry of polyester dyed fabrics..... 29

 PREPARATION AND CHARACTERIZATION OF INTEGRATING CAVITIES 33

 Aerosil Powder..... 33

 Aerosil Powder with Binder..... 34

 Reflectivity of Aerosil..... 51

 Variability and processing 52

 Calculated Enhancement..... 53

 Aerosil Cavities..... 54

 Photoluminescence Measurements 56

 Cavity improvements 59

 Control samples 62

 OPTICAL MEASUREMENTS 63

 Raman spectroscopy of dyes and dye fabrics without the use of an integrating cavity..... 63

 Near-IR Raman spectroscopy with 785 nm laser..... 66

 Raman spectroscopy of mixed dye samples..... 68

 Reference Raman Measurements..... 72

 Fluorescence Measurements 76

 Optical Cavity 76

 Cavity Ringdown with Lens Assembly 78

 Cavity Raman/Fluorescence Measurements 79

 Raman Measurements 81

 Fluorescence Measurements 89

 Optical Cavity 89

 Cavity Work..... 93

 Cavity Top Design 94

 Reconditioning Cavity 95

Influence of Fiber Raman Scattering	96
iCERS of Dyed Fabrics.....	98
iCERS of Transparent Materials	98
DUV Measurements.....	99
Pulsed DUV Raman.....	100
REFERENCES	105

Table of Figures

Figure 1. Diagram explaining the design and ionization mechanism of DART ionization source.	22
Figure 2. Photo showing threads mounted on IonSense® Quick Strip™ sample card after DART-QTOF analyses.	23
Figure 3. Mass spectra obtained from DART-QTOF analyses on single color PET threads.	24
Figure 4. Mass spectra obtained from DART-QTOF analyses on single color PET threads.	25
Figure 5. FTIR of Aerosil OX 50 before and after bake-out.	33
Figure 6. Aerosil powder pressed into 0.5” diameter pellets for 5 min at different pressures: (a) 500 lb, (b) 1000 lb, and (c) 2000 lb.	34
Figure 7. Aerosil powder pressed into 1” diameter pellets for 5 min at different pressures: (a) 500 lb, (b) 1000 lb, and (c) 2000 lb.	34
Figure 8. Aerosil powder pressed at various pressures for 5 min to yield a part with a cavity: (a) 500 lb, (b) 1000 lb, and (c) 2000 lb.	34
Figure 9. Aerosil powder with 5% binder pressed into 1” diameter pellets for 5 min at different pressures: (a) 500 lb, (b) 1000 lb, and (c) 2000 lb.	35
Figure 10. Pictures showing: (a) four-part die used to produce the cylindrical part with a cuboid cavity, (b) as-prepared and (c) baked (600 °C for 6 h) Aerosil/binder.	35
Figure 11. FTIR spectra of pure Aerosil, pure binder, and unbaked and baked Aerosil/binder powder. ..	36
Figure 12. 4" diameter part during pressing (left) and temperature profile for subsequent bake-out (right).	36
Figure 13. Image of different cavities. From left to right: Accuratus, Heraeus, Aerosil + 5% binder w/o sintering, Aerosil + 5% binder + 1050 °C, 1 hr sintering.	37
Figure 14. Thorlabs 2” IS 200 integrating sphere used for reference measurements.	37
Figure 15. Heraeus HOD-500 cavity with attached optical fibers. This material is very hard and machining takes extra time.	38
Figure 16. Accuratus Accuflect cavity with attached optical fiber. This material is significantly softer than the Heraeus material and easier to machine.	38
Figure 17. Aerosil OX 50 cavity w/5wt% binder with attached optical fiber. Without sintering, this material is very brittle and tends to crumble.	39
Figure 18. Aerosil OX 50 cavity w/5wt% binder, sintered at 1050 °C for 1 hr, with attached optical fiber. The sintered material is more stable and easier to machine.	40
Figure 19. Comparison of diffuse reflectance of various cavity materials with respect to Spectralon (right).	41
Figure 20. FTIR of Aerosil OX 50 processed under different conditions. No changes in the material can be observed after the addition of 5 wt% PVBA (Poly(vinyl butyral-co-vinyl-alcohol-covinyl acetate)) binder and after sintering at 1050 °C for 1 hour.	41
Figure 21. FTIR comparison of the various cavity materials.	42
Figure 22. Raman spectra of various integrating cavity materials collected under 532 nm irradiation. The spectra are scaled and offset to show differences.	42
Figure 23. Raman spectra obtained when using an optical fiber made of fused quartz (left) and sapphire (right) under 532 nm irradiation.	43
Figure 24. Crushing and grinding Aerosil OX 50 following incorporation of 5% binder.	44
Figure 25. Sieved Aerosil OX 50+5wt% added to quartz mold with Plexiglas bottom.	44
Figure 26. Cavity pressed at 5,000 lbs for 15 minutes.	45
Figure 27. Cavity sintered at 1,050 °C for 6 hours (left) vs. 1 hour (right).	45
Figure 28. Comparison of cavities sintered at 1,050 °C as a function of soaking times of 6 hours (left), 3 hours (center), 1 hour (right).	46
Figure 29. Assembled cavity.	46
Figure 30. Reflectivity of various Aerosil samples relative to a new calibrated Spectralon standard whose reflectivity was normalized to 100%,	47

Figure 31. Preparation and processing of the Aerosil cavity material. Aerosil sintered in quartz mold with weighted top plates (left). Cavity and through ports prepared with various end mills (center), and flat mating faces prepared by grinding and polishing with SiC paper. 48

Figure 32. Reflectivity of Spectralon and sintered Aerosil samples (left) and zoomed-in view (right). The side of the Aerosil sample that was in contact with a quartz substrate shows higher reflectivities in the UV region. 48

Figure 33. SEM images of as-received Aerosil powder (left) and Aerosil powder mixed with binder (right). 49

Figure 34. Heating profile used for the preparation of Aerosil cavities. 49

Figure 35. SEM images of the two sintered Aerosil sides, in contact with quartz (left) and exposed to air in furnace (right). 50

Figure 36. Cavity prepared in September of 2020. 51

Figure 37. Cavity prepared in December of 2020. 51

Figure 38. Absolute reflectivity of Spectralon and Aerosil measured using a UV/VIS Spectrophotometer. 52

Figure 39. Multiple measurements of the reflectivity show the good level of reproducibility of our data. After polishing, the reflectivity below about 230 nm increased somewhat. The reflectivity of the Spectralon sample is shown for comparison. 52

Figure 40. Calculated enhancement as a function of reflectivity. 54

Figure 41. Example pulse ringdown curves for the Sep 2020 cavity. The calculated reflectivity is 98.7%. 54

Figure 42. Pulse measurements on different days in December 2020. Between the Dec 17/18 measurements and the 22nd and 23rd measurements the cavity was stored in a heated vacuum oven. 55

Figure 43. PL signal from empty cavity. 56

Figure 44. PL Intensity spectra measured in three difference scenarios. 57

Figure 45. DSC and TG/DTG curves of Aerosil OX 50 + binder in nitrogen atmosphere (40 mL min⁻¹) and heating rate 20 °C min⁻¹. 58

Figure 46. DSC and TG/DTG curves of Aerosil OX 50 + binder in zero air atmosphere (40 mL min⁻¹) and a heating rate 20 °C min⁻¹. 59

Figure 47. New Aerosil cylinder prepared to enlarge existing cavity volume. 60

Figure 48. Post sintering weight of new cavity cylinder, 238 g for weight loss of 12 g or 4.8% weight loss. 60

Figure 49. Cavity center modified to 2" x 2" square. 60

Figure 50. Cavity volume increased by the addition of a second hollow segment. A new top was fabricated to accommodate a kinematic mound to correct for beam offset. 61

Figure 51. Cavity component bakeout. 61

Figure 52. Pellets prepared for determination of spurious fluorescence. 62

Figure 53. Schematic diagram of the Raman setup. Green lines represent the incident 532 nm laser light and Raleigh scattering while the red lines represent all other signals from the sample. 63

Figure 54. a) The Stokes and antiStokes Raman spectrum of nylon fabric both uncorrected and corrected. b) The uncorrected Stokes and antiStokes Raman spectra of Telon Yellow FG01 (olive) and Acid Yellow 049 (yellow). c) A comparison of the corrected Stokes and antiStokes Raman spectra of dye Acid Yellow 049, Telon Yellow FG01 and Nylon fabric under 532 nm irradiation. Dashed lines are added for comparison of common spectral features. 64

Figure 55. The baseline corrected Raman spectra of dyes Acid Yellow 049, Acid Blue 260 and Acid Red 337 sampled directly from powders in the antiStokes (a) and Stokes (b) spectral regions, respectively. The Raman spectra of the same dyes deposited on Nylon fabric are presented as Telon Yellow FG01, Eroinyll Blue AR and Telon Red FLRS in the antiStokes (c) and Stokes (d) regions, respectively. 65

Figure 56. The corrected, overlaid and scaled spectrum of Acid Red 337 (red, top), Telon Red FLRS (red, lower), Nylon Black (black) and Nylon fabric (purple). Dashed lines are added to highlight similarities between spectra. 65

Figure 57. The normalized absorption spectrum of acid dyes dissolved in water. The Stokes and antiStokes Raman spectra of cyclohexane is overlaid when excited with 532 nm laser light (green dashed line). 66

Figure 58. Comparison of CCD and PMT response. 67

Figure 59. Raman signals collected for a dyed “Black Fabric” showing the strong, periodic etaloning which becomes more persistent further to the red. 67

Figure 60. Etaloning effect becomes strikingly more persistent with more reflective materials such as powder dyes Acid Orange 67 (AO67) and Acid Yellow 49 (AY49)..... 68

Figure 61. Fabrics prepared with different amounts of AY49 and AO67. The 50:50 dyed sample is very orange, becoming increasingly lighter as the orange concentration is decreased. When only 1% AO67 is used, the fabric becomes a vibrant yellow. 69

Figure 62. Raw spectra of dyed fabrics presented in Figure 55. As the relative dye concentrations change, the stray scattered light entering the spectrograph changes in shape and amplitude. 70

Figure 63. Microscope images (2x magnification) of commercial dye powder Permasil Rubine. The left image shows the dye as purchased. The right image shows the same dye after trying to solvate it. 70

Figure 64. 8x magnification images of recrystallized dye samples of AR337 and AY49. The relative ratio of AR337 to AY49 are 50:50 (left), 25:75 (center), and 7:93 (left)..... 71

Figure 65. Corrected Raman spectra of pure dyes AR337 and AY49 as well as the three mixtures. 72

Figure 66. Molecular structures of AR337 (left) and AY49 (right). Reproduced from PubChem (<https://pubchem.ncbi.nlm.nih.gov/>). 73

Figure 67. Standard 532 nm Raman measurements of various dyed nylon fabric swatches. 74

Figure 68. Standard 532 nm Raman spectra of AR337 powder, solution, and dye fabric, as measured (right) and normalized (left)..... 75

Figure 69. Standard 532 nm Raman spectra of AY49 powder, solution, and dye fabric, as measured (right) and normalized AY49 powder and solution spectra (left). 75

Figure 70. Filtered fluorescence spectra of nylon fibers dyed with AR337 and AY049. 76

Figure 71. Ray trace diagram of lens stack. 77

Figure 72. Fluorescence spectra of tape. 78

Figure 73. Comparison of cavity and electrical tape fluorescence demonstrating that the peaks are not the same. 78

Figure 74. Fluorescence spectra of DO11 dye-doped polymer measured using cavity and standard spectrometer..... 79

Figure 75. Fluorescence spectra of AY049 dissolved in methanol measured using the standard spectroscopy system and the cavity system. Note that the sharp peak near 680 nm arises from the crucible..... 80

Figure 76. Emission measured from empty cavity and cavity containing BaSO4. Inset: difference spectra showing weak BaSO4 Raman peak. 81

Figure 77. Schematic of THz Raman spectrometer. The Reflective Bragg Grating (RBG) narrows the laser line and has a peak efficiency at a 20-degree incidence angle and a spec'd spectral bandwidth of $< 7 \text{ cm}^{-1}$. Each Bragg Notch Filter (BNF) is spec'd to be OD3 with a notch width of $< 10 \text{ cm}^{-1}$ 82

Figure 78. Laser line spectrum. The bandwidth is spectrometer limited. 83

Figure 79. Transmission curve for bandpass filters and laser line for reference..... 84

Figure 80. THz Raman spectra of several crystalline test samples. 84

Figure 81. Example THz Raman spectra from different dyed nylon samples. The observed peaks are consistent with either the background (air) or nylon peaks. 86

Figure 82. Bonding between AY 49 with nylon (left) and AR 337 with nylon (right)..... 86

Figure 83. Normalized Raman spectra of clean blank nylon and various AY 49 and AR 337 dyed nylon samples..... 87

Figure 84. Peak positions based on Lorentzian fits..... 87

Figure 85. Visible absorption spectra of nylon and dyed nylon samples..... 87

Figure 86. Raman spectra of Ar 337 and AY 49 in 50% MeOH/50% DI water and the solvent without a dye..... 88

Figure 87. Raw spectra collected from AR337 and AY049 fibers using 100 mW of 532 nm excitation (left). Background subtracted Raman spectra for AY049 (right). In this set of experiments the AY049 provided excellent Raman signal, while the AR337 signal was overwhelmed by fluorescence. This result is opposite to experiments with lower laser powers. 88

Figure 88. Fluorescence measured from edge of Thorlabs lens. 89

Figure 89. Emission spectrum measured from empty Aerosil cavity excited at 532 nm. Inset: small peak at 2329 cm⁻¹, which is associated with atmospheric nitrogen. 90

Figure 90. Comparison of nitrogen peaks measured using Thorlabs Spectralon cavity and our Aerosil cavity. Note that while the Aerosil cavity appears to have a better signal to noise ratio than the Thorlabs cavity, its volume is also 3.25 times larger, which means that there is more air (sample) in the cavity. ... 91

Figure 91. Comparison of background subtracted nitrogen peaks for Aerosil and Thorlabs cavity as well as in a standard spectrometer. Note that while the cavity measurements used the same spectrometer, the standard measurements used a different spectrometer, so direct comparisons are not easy. 91

Figure 92. Raman spectra measured from different configurations. The cavity difference spectrum is determined by subtracting the BaSO₄ spectra from the background measurements. 92

Figure 93. Comparison of cavity background for 5 different assemblies. 92

Figure 94. Emission from NIJ cavity both with and without Thorlabs lenses. 93

Figure 95. Comparison of emission from lenses from different vendor. 93

Figure 96. Emission from different aerosil pellets. 94

Figure 97. Fluorescence spectra of dye-doped polymer with different lens configurations. 95

After working on the cavity top design, we next checked the cavity's reflectivity as the cavity has been sitting in open air for some time and collected some dust contamination and may have absorbed some water. Doing so we found that the reflectivity dropped to $R = 98.600 \pm 0.070$, which is below the 99% reflectivity threshold we determined for sufficient cavity enhancement. Given the observed decrease in reflectivity we next cleaned and baked out the cavity, which resulted in improved reflectivity $R = 99.460 \pm 0.065$. See Figure 98 for a comparison of ringdown pulses before and after reconditioning of the cavity. 95

Figure 99. Comparison of ringdown measurements before and after cavity reconditioning. 95

Figure 100. Raman spectrum from input fiber which displays all the typical features of fused silica²³... 96

Figure 101. Raman spectra of sugar water in cavity with either no filters, 355 nm notch filter on output fiber, or a 355 nm bandpass filter on the input fiber and 355 nm longpass filter on output fiber. 97

Figure 102. Raw Raman spectra of various fibers in cavity for 532 nm (a) and 355 nm (b) excitation. ... 98

Figure 103. Comparison of standard and cavity Raman spectra for sugar water at 30% (a) and 3% (b) w/v concentration. Note that the cavity signal is significantly brighter demonstrating the cavity enhancement effect. 99

Figure 104. DUV Raman spectra of reference materials using OPO (a) and THG from MIRA (b). The peaks using the MIRA laser system are significantly broadened due the laser being a femtosecond system. 100

Figure 105. Raw (a), background (b), and background subtracted (c) Raman spectra from dye-doped nylon using 266 nm excitation. 101

Figure 106. Comparison of background measurements using different excitation wavelengths. 102

Figure 107. Background measured using MIRA third harmonic at 266 nm. 102

Figure 108. DUV Raman spectra of nylon fibers (a) and dye powders (b) with clean nylon's spectra for reference. 103

Figure 109. Comparison of fluorescence from pristine and photodamaged fabrics for AR337-dyed nylon (a), AY049-dyed nylon (b) and neat nylon (c). 104

Table of Tables

Table 1. Quality control results on selected commercial acid dyes.....	13
Table 2. Quality control results on selected commercial disperse dyes	14
Table 3. Quality control results on selected commercial disperse dyes	15
Table 4. Quality control results on selected commercial acid dyes.....	15
Table 5. Quality control results on selected commercial reactive dyes.....	15
Table 6. Quality control results on selected commercial acid dyes.....	16
Table 7. Quality control results on selected commercial disperse dyes.	17
Table 8. Quality control results on selected commercial dyes.	18
Table 9. Single and dichromatic dyed fabrics.	21
Table 10. Dyes to be investigated in mixtures.	25
Table 11. Initial binary reactive dye mixtures (ratio in 3% total).	26
Table 12. Initial ternary reactive dye mixtures (weight percent).	26
Table 13. Initial binary disperse dye mixtures (ratio in 3% total).....	26
Table 14. Initial ternary disperse dye mixtures (weight percent).....	26
Table 15. Initial binary acid dye mixtures (ratio in 3% total).	27
Table 16. Initial ternary acid dye mixtures (weight percent).	27
Table 17. Combined reactive and disperse dye mixtures on poly-cotton blend fabric (A4) and grid fabric (A5) (ratio in 3% total).	27
Table 18. Fabrics dyed with a single dye for initial readings.....	27
Table 19. Cotton fibers dyed using mixtures of reactive dyes (ratio in 3% total) combined table.	28
Table 20. Polyester fibers dyed using mixtures of disperse dyes (ratio in 3% total) combined table.....	28
Table 21. Nylon fibers dyed using mixtures of acid dyes (ratio in 3% total) combined table.	28
Table 22. High-Res LCMS ESI Mass Spectrometry Results: m/z ratio and characteristic information for fiber reactive dyes with confirmed identity and exact mass.	30
Table 23. High-Res LCMS ESI Mass Spectrometry Results: m/z ratio and characteristic information for disperse dyes with confirmed identity and exact mass.	31
Table 24. High-Res LCMS ESI Mass Spectrometry Results: m/z ratio and characteristic information for acid dyes with confirmed identity and exact mass.....	32
Table 25. Measured ringdown time and calculated reflectivities measured on different days.....	55
Table 26. Ringdown repeatability measurements.	56
Table 27. Relevant specs for spectrometer components.	82
Table 28. Measured wavelength errors for lines of Hg and Ne in the 500 nm - 600 nm range. The average error is 0.011 nm (0.335 cm ⁻¹) and the rms error is 0.003 nm.	82

EXECUTIVE SUMMARY

The characterization and analysis of trace evidence such as fibers, hair, soil, wood, gunshot residue, etc. is part of the standard protocol during forensic investigations. Trace evidence can potentially be used to link a suspect with a victim, or a suspect/victim with a location. Because of the importance of trace evidence, the National Institute for Justice seeks “to improve and enhance the ability of the forensic science community to identify, analyze and interpret evidence.”¹

Textile fibers are one type of trace evidence, and color of the fiber is one of the most important properties.² ³ Fibers are typically analyzed using a variety of techniques and compared with a reference. The goal of the analysis is to reject the null hypothesis that the fibers originated from the same source. First, nondestructive techniques such as light microscopy (e.g., bright field and fluorescence) and UV/Vis microspectrophotometry (MSP) are used. If these don’t yield conclusive results, destructive techniques (dye is extracted from fiber) such as thin-layer chromatography (TLC) and gas-chromatography mass spectrometry (GCMS) are used.⁴⁻⁷ Modified approaches that limit the amount of sample needed for destructive techniques have been developed.⁸⁻¹²

More recently, Raman spectroscopy has been evaluated as a non-destructive analytical tool for the characterization of fibers.^{5, 13-18} Besides its non-destructive nature, Raman spectroscopy offers other advantages such as: requiring almost no sample preparation, yielding more distinctive spectra than UV/VIS/NIR absorption/reflectance spectra, and providing unique sample information. In fact, “Raman Spectroscopy of Fibres” is now a main chapter in the most recent edition of *Forensic Examination of Fibres*, the go-to reference in this field, edited by J. Robertson, et al.⁷

While Raman spectroscopy has been identified as a promising tool that can supplement other analytical techniques, it has its own set of limitations, with the main one being sample fluorescence which is typically orders of magnitude stronger than the actual Raman signal.^{5, 13-15, 17, 18} In addition, if the selected laser power is too high, the sample to be investigated can be significantly heated, leading to spectral changes, and possibly irreversible thermal damage and photodegradation.¹⁹

Garment fibers are often colored using a mixture of dyes. Due to the limitations described above, however, Raman spectroscopy can often only identify the dye with the highest concentration or the one resulting in the strongest Raman scattering peaks. Although, changing the wavelength of the Raman laser can sometimes help in identifying a secondary dye.^{16, 20} Given that there exists thousands of dyes, the ability to identify only one or two dyes within a dye composition can severely limit the usefulness of Raman spectroscopy for forensic purposes.

Several approaches have been investigated to address these limitations with limited success. The goal of this project was to evaluate integrating-cavity-enhanced Raman spectroscopy (ICERS) for its potential to significantly enhance the signal strength while simultaneously removing the fluorescence, thus enhancing the signal-to-noise ratio (S/N), allowing for the identification of minor dye components on fibers. The main objectives were:

1. To determine and compare the respective S/N of standard Stokes Raman spectra and ICERS anti-Stokes Raman spectra of red, blue, and black dyes and mixtures thereof.
2. To determine and compare the respective S/N of standard Stokes Raman spectra and ICERS anti-Stokes Raman spectra of cotton and polyester fibers dyed with red, blue, and black dyes.
3. To determine and compare the respective S/N of standard Stokes Raman spectra and ICERS anti-Stokes Raman spectra of cotton and polyester fibers dyed with mixtures of red, blue, and black dyes, and to determine the minimum detectable dye concentrations that can be identified.

Cavity-enhanced spectroscopy techniques have been developed for the ultrasensitive identification and characterization of materials. The basic concept behind this approach is the multifold interaction between the excitation light and the sample, which enhances the effective pathlength. At the same time, this approach also results in the collection of almost all scattered light and the collection is no longer limited by the numerical aperture (NA) of the collection optics. The potential of this approach has been demonstrated by Bixler et al. who showed that ICERS can increase the Raman signal of bulk pyrene by 5 orders of magnitude.²¹

Our work focused on the preparation and characterization of integrating cavities and the subsequent comparison of Raman measurement of dyed fabric samples made without and with the use of the integrating cavities. Besides regular Raman measurements, we also evaluated terahertz (THz) Raman measurements and deep ultraviolet (DU) Raman measurements.

We encountered a wide range of challenges during this project, including:

- The preparation of integrating cavities from highly reflecting fumed silica required the development of new procedures and techniques that would allow for cavities that are simultaneously mechanically stable and highly reflecting.
- Machining of the cavities to integrate optical components required the development of new processes.
- Matching of the optical properties of the cavities with those of optical fibers to collect Raman-scattered light, required tradeoffs.
- The cavities appeared to enhance residual fluorescence from some optical components, overwhelming the desired Raman signals.

While we were able to successfully address the cavity processing and preparation challenges, we were not able to make satisfactory Raman measurements inside the cavity that would have demonstrated the desired signal enhancement. However, our THz measurements showed that the structural properties of the fabric (nylon) are affected by the dyeing process. Depending on the dye concentration, the Raman peak of nylon shows a distinct shift in energy. Our preliminary observations show that the interaction of two acid dyes, both of which electrostatically interact with the protonated terminal amino group $R-NH_3^+$ of nylon via their $R-SO_3^-$ functional groups, results in opposite changes to the dihedral angle of the C-C nylon backbone. The THz Raman spectra show this impact as red and blue shifts of the rotational C-C torsion band of nylon. This information, collected in the terahertz region, could provide structural properties indicative of the dye-fabric interaction, which could help identify textile trace evidence.

ACCOMPLISHMENTS

What are the major goals of the project?

The purpose of this project is to enhance the analytical capabilities for forensic examinations of dyed fibers. The specific goal is to evaluate integrating-cavity-enhanced Raman spectroscopy (ICERS) for its potential to significantly enhance the signal strength while simultaneously removing the fluorescence, thus enhancing the signal-to-noise ratio (S/N), allowing for the identification of minor dye components on fibers. The main objectives are:

Objective #1: To determine and compare the respective S/N of standard Stokes Raman spectra and ICERS anti-Stokes Raman spectra of red, blue, and black dyes and mixtures thereof.

Objective #2: To determine and compare the respective S/N of standard Stokes Raman spectra and ICERS anti-Stokes Raman spectra of cotton and polyester fibers dyed with red, blue, and black dyes.

Objective #3: To determine and compare the respective S/N of standard Stokes Raman spectra and ICERS anti-Stokes Raman spectra of cotton and polyester fibers dyed with mixtures of red, blue, and black dyes, and to determine the minimum detectable dye concentrations that can be identified.

Cavity-enhanced spectroscopy techniques have been developed for the ultrasensitive identification and characterization of materials. The basic concept behind this approach is the multifold interaction between the excitation light and the sample, which enhances the effective pathlength. At the same time, this approach also results in the collection of almost all scattered light and the collection is no longer limited by the numerical aperture (NA) of the collection optics. The potential of this approach has been demonstrated by Bixler et al. who showed that ICERS can increase the Raman signal of bulk pyrene by 5 orders of magnitude.²¹

ID	Tasks	Duration	Milestones	Status
1	Prepare and characterize integrating cavities.	Q1-Q2	Five integrating cavities with reflectivities of 0.99 or higher.	Completed.
2	HPLC- Mass spectrometry characterization of commercial dyes.	Q1-Q4	Identified dye structures and confirmed molecular formula of single chromophores and mixtures of colors (e.g., disperse black)	Completed.
3	Preparation of dye mixtures for standard Raman and ICERS.	Q1-Q10	Dye mixtures available when needed.	Completed.
4	Standard Raman measurements of dyes and dye mixtures.	Q1-Q3	Raman spectra of 12 individual dyes and multiple dye mixtures. Conclusion about ability to detect any minor dye components using standard Raman spectroscopy.	Completed.

5	ICERS measurements of pure dyes.	Q3-Q4	ICERS spectra of pure dyes. Calculated enhancement factor for ICERS vs. standard Raman.	Due to the challenges mentioned above, we were not able to conduct measurements that showed Raman enhancement from the cavities.
6	ICERS measurements of binary dye mixtures.	Q4-Q5	ICERS spectra of binary dyes. Minimum dye concentrations that can be identified using ICERS.	Due to the challenges mentioned above, we were not able to conduct measurements that showed Raman enhancement from the cavities.
7	ICERS measurements of ternary dye mixtures.	Q6-Q7	ICERS spectra of ternary dyes. Minimum dye concentrations that can be identified using ICERS.	Due to the challenges mentioned above, we were not able to conduct measurements that showed Raman enhancement from the cavities.
8	ICERS measurements of dyed cotton and polyester fibers.	Q8-Q9	ICERS spectra of dyed fibers. Minimum dye concentrations that can be identified on fibers using ICERS.	Due to the challenges mentioned above, we were not able to conduct measurements that showed Raman enhancement from the cavities.
9	Preparation of blind dyed fiber samples.	Q2-Q8	Prepared 40 samples. Performed spectrophotometric measurements to ensure levelness of dyeing.	Due to the challenges mentioned above, we were not able to conduct measurements that showed Raman enhancement from the cavities.
10	Characterization of blind fiber samples.	Q10	Identification of samples that contain minor dye components.	Due to the challenges mentioned above, we were not able to conduct measurements that showed Raman enhancement from the cavities.
11	Prepare scientific manuscripts	Q3 – Q10	Submitted manuscripts	Completed.
12	Prepare progress reports	July and January of each year.	Progress reports.	Completed.
13	Prepare financial reports	Quarterly	Financial reports	Ongoing.
14	Prepare final technical report draft	Q9	Final technical report draft submitted to NIJ	Completed
15	Prepare final technical report	Q10	Final technical report submitted to NIJ	Completed.

What was accomplished under these goals?

PREPARATION AND CHARACTERIZATION OF DYED FABRIC SAMPLES

Quality control (QC) of commercial dye by high-resolution mass spectroscopy

Prior to the dyeing of fabrics, the exact mass and formula of each commercial dye used in this study were validated by an Agilent Technologies 1260 High-Performance Liquid Chromatography (HPLC) system coupled with an Agilent 6520B Q-TOF high-resolution mass spectrometer. In order to facilitate the analysis, acid dye powders were dissolved by HPLC grade methanol and water at a ratio of 50:50 while disperse dye powders were dissolved by HPLC grade acetone. The mobile phase was made up by a mixture of acetonitrile and water at a ratio of 9:1, the flow rate was set to 0.5 mL/min and the total run time for each sample was 3 minutes. Ionization was performed via a dual electrospray ionization (ESI) system and was carried out in both positive and negative mode with the following parameters: gas temperature 350 °C, drying gas 5 liters per minute, nebulizer 30 psi, V_{cap} voltage 4000 V and fragmentor voltage at 180 V. In order to improve the mass accuracy, a solution of mass reference mix obtained from Agilent was introduced via a secondary ESI needle.

After each sample run, the data file was processed by Agilent MassHunter Qualitative analysis software, where formula generation function would provide information regarding the dye's formula and exact mass. The results from QC were summarized in Table 1 and Table 2. A total of 20 acid and disperse dyes were tested by HPLC-MS and 11 dyes were found to match with their available structure. Some of the unmatched dyes showed a discrepancy between available structure and observed exact mass and some other dyes didn't have available structures because their structure is confidential. After QC performed at Vinueza labs, the confirmed acid and disperse dyes were approved and sent to the dyeing facility at the Wilson College of Textiles where single color fabrics and black formulation fabrics would be produced.

Table 1. Quality control results on selected commercial acid dyes.

CI #	Commercial Name	Chromophore	Exact Mass	Mol. Weight	Chemical Formula	Observed Mass	Anion	Error (ppm)
Orange 67	Erionyl Yellow AR	Azo	582.0885	582.6025	C ₂₆ H ₂₂ N ₄ O ₈ S ₂	581.0804	[M-H] ⁻¹	0.39
Blue 260	Erionyl Blue AR	AQ	569.1621	568.6245	C ₃₁ H ₂₇ N ₃ O ₆ S	568.1571	[M-H] ⁻¹	2.98
Blue 62	Telon Blue RR 01	AQ	400.1098	400.4495	C ₂₀ H ₂₀ N ₂ O ₅ S	399.1025	[M-H] ⁻¹	1.27
Yellow 49	Telon Yellow FG01	Azo	425.0122	426.2725	C ₁₆ H ₁₃ Cl ₂ N ₅ O ₃ S	424.0046	[M-H] ⁻¹	0.43
Red 337	Telon Red FRLS	Azo	411.0501	411.3552	C ₁₇ H ₁₂ F ₃ N ₃ O ₄ S	410.0435	[M-H] ⁻¹	1.47

Table 2. Quality control results on selected commercial disperse dyes.

CI #	Commercial Name	Chromophore	Exact Mass	Mol. Weight	Chemical Formula	Observed Mass	Cation	Error (ppm)
Blue 56	Dianix Blue ER	AQ	347.9746	349.1400	C ₁₄ H ₉ BrN ₂ O ₄	348.9813	[M+H] ⁺	2.36
Blue 60	Terasil Blue BGE	Azo	379.1168	379.3720	C ₂₀ H ₁₇ N ₃ O ₅	380.1243	[M+H] ⁺	0.31
Red 60	Dianix Red EFB	AQ	331.0845	331.3270	C ₂₀ H ₁₃ NO ₄	332.0920	[M+H] ⁺	0.72
Red 82	Terasil Red 3BL	Azo	439.1492	439.4280	C ₂₁ H ₂₁ N ₅ O ₆	440.1560	[M+H] ⁺	0.07
Red 153	Terasil Red 4GN	Azo	403.0425	404.3130	C ₁₈ H ₁₅ Cl ₂ N ₅ S	404.0497	[M+H] ⁺	0.19
Yellow 211	Terasil Yellow 4G	Azo	361.0578	361.7420	C ₁₅ H ₁₂ ClN ₅ O ₄	362.0652	[M+H] ⁺	0.41

Quality Control (QC) tests were performed on a total of 48 commercial dyes including 17 disperse dyes, 16 acid dyes, and 15 reactive dyes. A total of 34 commercial dyes were confirmed to have a formula confirmed with their claimed structure. Interestingly, only 71% can be confirmed based on known structures. This result clearly shows that the current information of commercial dyes has to be taken with caution.

In QC tests, the exact mass and chemical formula of each commercial dye used in this phase of the project were validated by an Agilent 6520B Q-TOF high-resolution mass spectrometer coupled with an Agilent Technologies 1260 High-Performance Liquid Chromatography (HPLC) system. In order to facilitate the analysis, acid dye powders were dissolved in HPLC grade methanol and water at a ratio of 50:50 while disperse dye powders were dissolved in ACS grade acetone. The mobile phase was a mixture of HPLC grade acetonitrile and water at a ratio of 9:1. The flow rate was set to 0.5 mL per minute and the total run time for each sample was 3 minutes. Ionization was performed via dual electrospray ionization (ESI) and was carried out in both positive and negative modes with the following parameters: gas temperature 325 °C, drying gas 8 liters per minute, nebulizer 50 psi, V_{cap} voltage 4000V and fragmentor voltage at 170V. In order to improve the mass measurement accuracy, a solution of mass reference mix obtained from Agilent Technologies was introduced via a secondary ESI needle. In addition to single-stage mass spectra, spectra from tandem mass (MS/MS) spectrometry were gathered simultaneously using the auto MS/MS mode. In auto MS/MS mode, the system automatically isolates a series of precursor ions and fragments them using Collision-Induced Dissociation (CID). In CID, nitrogen gas was used as collision gas, isolation width was set to a 1.3 mass-to-charge ratio and collision energy was set to 5, 10, 20, 30, 40 and 50 eV.

After each sample run, the corresponding data file was processed by Agilent MassHunter Qualitative analysis software, where the formula generation function provided information regarding the chemical formula and exact mass of each dye. The results from QC tests are summarized in Table 3, Table 4, and Table 5, and categorized by dye class (disperse, acid, and reactive). A total of 34 commercial dyes were confirmed to have a formula matching their claimed structure including 14 disperse dye, 11 acid dyes, and 9 reactive dyes. Some of the unmatched dyes showed a discrepancy between claimed structure and observed exact mass, and some dyes didn't have available structures because their structure is confidential. After QC tests, the confirmed acid, disperse and reactive dyes were sent to a dyeing facility where single color fabrics, black formulations, and dichromatic fabrics would be produced.

Table 3. Quality control results on selected commercial disperse dyes

Color Index Name	Commercial Name	Chemical Formula	Theoretical Exact Mass	Experimental Exact Mass	Ion species (charge)	ppm Error
Disperse Blue 56	Dianix ER	C ₁₄ H ₉ BrN ₂ O ₄	347.9746	348.9813	[M+H] (+1)	2.36
Disperse Blue 60	Terasil Blue BGE	C ₂₀ H ₁₇ N ₃ O ₅	379.1168	380.1243	[M+H] (+1)	0.31
Disperse Red 60	Dianix EFB	C ₂₀ H ₁₃ NO ₄	331.0845	332.0920	[M+H] (+1)	0.72
Disperse Red 82	Terasil Red 3BL	C ₂₁ H ₂₁ N ₅ O ₆	439.1492	440.1560	[M+H] (+1)	0.07
Disperse Red 153	Terasil Red 4GN	C ₁₈ H ₁₅ Cl ₂ N ₅ S	403.0425	404.0497	[M+H] (+1)	0.19
Disperse Yellow 211	Terasil Yellow 4G	C ₁₅ H ₁₂ ClN ₅ O ₄	361.0578	362.0652	[M+H] (+1)	0.41
Disperse Red 86	Foron Brill Red AS-5GL	C ₂₂ H ₁₈ N ₂ O ₅ S	422.0936	423.1005	[M+H] (+1)	3.14
Disperse Blue 77	Teratop Blue BLF	C ₂₀ H ₁₂ N ₂ O ₆	376.0695	377.0764	[M+H] (+1)	2.2
Disperse Orange 73	Dianix Orange S-G	C ₂₄ H ₂₁ N ₅ O ₄	443.1594	444.1665	[M+H] (+1)	0.23
Disperse Blue 287	Dianix Blue 3RLS	C ₂₃ H ₂₄ N ₆ O ₄	448.1859	449.1945	[M+H] (+1)	-2.4
Disperse Yellow 82	Terasil Flavine 8GFF	C ₂₀ H ₂₁ N ₃ O ₂	333.1477	334.1548	[M+H] (+1)	0.63
Disperse Red 367	Dianix Brill Scarlet SF	C ₂₈ H ₂₂ O ₈	486.1315	487.1392	[M+H] (+1)	-1.82
Disperse Violet 28	Dianix Brill Violet B	C ₁₄ H ₈ Cl ₂ N ₂ O ₂	305.9963	307.0030	[M+H] (+1)	1.82
Disperse Yellow 114	Dianix Yellow 6G SL-FS	C ₂₀ H ₁₆ N ₄ O ₅ S	424.0841	425.0902	[M+H] (+1)	2.84

Table 4. Quality control results on selected commercial acid dyes

Color Index Name	Commercial Name	Chemical Formula	Theoretical Exact Mass	Experimental Exact Mass	Ion species(charge)	ppm Error
Acid Orange 67	Erionyl Yellow AR	C ₂₆ H ₂₂ N ₄ O ₈ S ₂	582.0885	581.0811	[M-H] (-1)	-0.62
Acid Blue 62	Telon Blue RR 01	C ₂₀ H ₂₀ N ₂ O ₅ S	400.1093	399.1025	[M-H] (-1)	1.27
Acid Yellow 49	Telon Yellow FG01	C ₁₆ H ₁₃ Cl ₂ N ₃ O ₃ S	425.0116	424.0046	[M-H] (-1)	0.43
Acid Red 337	Telon Red FRLS	C ₁₇ H ₁₂ F ₃ N ₃ O ₄ S	411.0501	410.0435	[M-H] (-1)	1.47
Acid Blue 90	Permalon Polar Blue G	C ₄₇ H ₄₉ N ₅ O ₇ S ₂	831.3012	830.2927	[M-H] (-1)	0.8
Acid Orange 7	Permalon Orange II	C ₁₆ H ₁₂ N ₂ O ₄ S	328.0518	327.0446	[M-H] (-1)	0.42
Acid Red 182	Isolan Bordeaux R	C ₁₆ H ₁₃ N ₃ O ₄ S	343.0627	741.0287	[2M-4H+Co] (-1)	-0.28
Acid Yellow 79	Telon Yellow M-4GL	C ₄₇ H ₄₂ N ₁₀ O ₁₂ S ₄	1066.1866	1065.1784	[M-H] (-1)	0.4
Acid Black 172	Permalon Black RPL	C ₂₀ H ₁₂ N ₃ O ₇ S	439.0474	924.0102	[2M-4H+Cr] (-1)	-0.07
Acid Yellow 199	Telon Yellow 4R	C ₁₉ H ₁₆ N ₄ O ₆ S	428.0791	427.0723	[M-H] (-1)	-0.89
Acid Black 58	Acid Black 58	C ₁₉ H ₁₇ N ₃ O ₆ S	415.0838	876.0824	[2M-4H+Cr] (-1)	1.21

Table 5. Quality control results on selected commercial reactive dyes

Color Index Name	Commercial Name	Chemical Formula	Theoretical Exact Mass	Experimental Exact Mass	Ion species (charge)	ppm Error
Reactive Red 123	Levafix Scarlet E-2GA	C ₂₁ H ₁₄ ClF ₂ N ₅ O ₈ S ₂	600.9940	599.9864	[M-H] (-1)	0.5
Reactive Blue 4	Procion Blue MXR	C ₂₃ H ₁₄ Cl ₂ N ₆ O ₈ S ₂	635.9692	634.9619	[M-H] (-1)	1.76
Reactive Yellow 86	Procion Yellow MX-8G	C ₁₈ H ₁₆ Cl ₂ N ₈ O ₉ S ₂	621.9859	620.9713	[M-H] (-1)	2.17
Reactive Blue 19	Remazol Brill Blue R	C ₂₂ H ₁₆ N ₂ O ₇ S ₂	484.0399	483.0329	[M-H] (-1)	-0.37
Reactive Orange 16	Remazol Brill Orange 3R	C ₂₀ H ₁₇ N ₃ O ₇ S ₂	475.0508	474.0436	[M-H] (-1)	0.21
Reactive Orange 107	Everzol Orange BN	C ₁₆ H ₁₆ N ₄ O ₆ S ₂	424.0511	423.0388	[M-H] (-1)	-0.72

Reactive Red 21	Everzol Red BB	C ₂₇ H ₂₂ N ₄ O ₁₁ S ₃	674.0447	673.0366	[M-H] (-1)	-1.18
Reactive Blue 225	Levafix Navy Blue E-BNA	C ₂₈ H ₁₉ ClF ₂ N ₈ O ₁₂ S ₄	859.9662	858.9587	[M-H] (-1)	0.24
Reactive Yellow 176	Remazol Yellow 3RS	C ₂₈ H ₂₂ ClN ₉ O ₁₂ S ₄	838.9959	418.4912	[M-2H] (-2)	-0.8

Prior to the dyeing of fabrics, the exact mass and formula of each commercial dye used in this study were validated by an Agilent Technologies 1260 High-Performance Liquid Chromatography (HPLC) system coupled with an Agilent 6520B Q-TOF high-resolution mass spectrometer. To facilitate the analysis, acid dye powders were dissolved by HPLC grade methanol and water at a ratio of 50:50 while disperse dye powders were dissolved by HPLC grade acetone. The mobile phase was made up by a mixture of acetonitrile and water at a ratio of 9:1, the flow rate was set to 0.5 mL/min and the total run time for each sample was 3 minutes. Ionization was performed via a dual electrospray ionization (ESI) system and was carried out in both positive and negative mode with the following parameters: gas temperature 350 °C, drying gas 5 liters per minute, nebulizer 30 psi, V_{cap} voltage 4000 V and fragmentor voltage at 180 V. In order to improve the mass accuracy, a solution of mass reference mix obtained from Agilent was introduced via a secondary ESI needle.

After each sample run, the data file was processed by Agilent MassHunter Qualitative analysis software, where formula generation function would provide information regarding the dye's formula and exact mass. The results from recent QC tests were summarized in Table 6 and Table 7. In phase of the project, a total of 14 acid and disperse dyes were tested by HPLC-MS and 11 dyes were found to match with their available structure. Some of the unmatched dyes showed a discrepancy between available structure and observed exact mass and some other dyes didn't have available structures because their structure is confidential. So far, a total of 54 acid and disperse dyes have been tested, 38 of them have been confirmed by HRMS with a confirmation rate of about 70%. After QC performed at Vinueza labs, the confirmed acid and disperse dyes were approved and sent to the dyeing facility at the Wilson College of Textiles where single color fabrics and black formulation fabrics would be produced.

Table 6. Quality control results on selected commercial acid dyes.

CI #	Commercial Name	Chromophore	Exact Mass	Mol. Weight	Chemical Formula	Observed Mass	Anion	Error (ppm)
Acid Yellow 246	Tectilon Yellow 3R	Azo	517.0766	517.5740	C ₂₆ H ₁₉ N ₃ O ₅ S ₂	516.0688	[M-H](-1)	0.96
Acid Orange 10	Acid Orange 10	Azo	408.0086	408.3990	C ₁₆ H ₁₂ N ₂ O ₇ S ₂	407.0015	[M-H](-1)	0.59
Acid Black 194	Isolan Black 194	Azo	439.0474	439.3980	C ₂₀ H ₁₃ N ₃ O ₇ S	462.498	[2M-5H+Cr](-2)	0.86
Acid Black 52	Acid Black 52	Azo	439.0474	439.3980	C ₂₀ H ₁₃ N ₃ O ₇ S	301.9966	[2M-6H+Cr](-3)	1.51
Acid Green 40	Lanaset Green B	Anthraquinone	802.0249	803.6340	C ₃₈ H ₂₄ Cl ₂ N ₂ O ₁₀ S ₂	366.0432	[M-2H](-2)	2.51

Table 7. Quality control results on selected commercial disperse dyes.

CI #	Commercial Name	Chromophore	Exact Mass	Mol. Weight	Chemical Formula	Observed Mass	Cation	Error (ppm)
Disperse Red 15	Disperse Red 15	Anthraquinone	239.0582	239.2300	C ₁₄ H ₉ NO ₃	240.0653	[M+H](+1)	2.2
Disperse Blue 291	Permasil Blue SE-GBL	Azo	508.0706	509.0706	C ₁₉ H ₂₁ BrN ₆ O ₆	509.0784	[M+H](+1)	0.94
Disperse Red 73	Foron Rubine RD-GFL	Azo	348.1335	348.3660	C ₁₈ H ₁₆ N ₆ O ₂	349.1415	[M+H](+1)	3.76
Disperse Red 167:1	Foron Rubine S-2GFL	Azo	505.1364	505.9120	C ₂₂ H ₂₄ ClN ₅ O ₇	506.1438	[M+H](+1)	0.67
Disperse Blue 79:1	Terasil Navy S-2GRL	Azo	624.0816	625.3890	C ₂₃ H ₂₅ BrN ₆ O ₁₀	625.0889	[M+H](+1)	0.02
Disperse Red 4	Disperse Red 4	Anthraquinone	269.0688	269.2560	C ₁₅ H ₁₁ NO ₄	270.076	[M+H](+1)	0.17

Prior to the dyeing of fabrics, the exact mass and formula of each commercial dye used in this study were validated by an Agilent Technologies 1260 High-Performance Liquid Chromatography (HPLC) system coupled with an Agilent 6520B Q-TOF high-resolution mass spectrometer. To facilitate the analysis, reactive dye powders were dissolved by using HPLC grade methanol and water with a ratio of 50:50. For disperse dyes, all powders were dissolved using HPLC grade acetone.

For liquid chromatography of disperse dyes, the mobile phase was a mixture of acetonitrile and water at a ratio of 9:1, the flow rate was set to 0.5 mL/min and the total run time for each sample was 3 minutes. For reactive dyes, the mobile phase was comprised of ammonium formate buffer solution (A) (20 mM ammonium formate solution with the pH of the solution adjusted to 4 by adding formic acid) and acetonitrile (B) with a gradient elution (constant flowrate = 0.5 mL min⁻¹): from 0 to 4 minutes, 93% (B) to 91.5% (B). Next, from 4 to 9 minutes, 91.5% (B) to 78% (B). The column temperature and injection volume were set to 40 °C and 5 µL, respectively. An ACQUITY UPLC BEH Amide HILIC column (2.1x50 mm, 1.7 µm, Waters Corporation, NC, USA) was used as the stationary phase.

Ionization was performed via a dual electrospray ionization (ESI) system and was carried out in both positive and negative mode with the following parameters: gas temperature 350 °C, drying gas 5 liters per minute, nebulizer 30 psi, V_{cap} voltage 4000 V and fragmentor voltage at 180 V. To improve the mass accuracy, a solution of mass reference mix obtained from Agilent was introduced via a secondary ESI needle.

Data files were processed by Agilent MassHunter Qualitative analysis software, where the formula generation function provides information regarding the dye's formula and exact mass. The results from recent QC tests are summarized in Table 8. During this reporting period, a total of 12 reactive and disperse dyes were tested by HPLC-MS and tandem mass spectrometry. All structures matched with their available known structure. So far, a total of 70 acid, disperse and reactive dyes have been tested, 51 of them have been confirmed by HRMS with a confirmation rate of about 72%. In addition, tandem mass spectrometry (MS/MS) was performed to develop a commercial dye database to enhance the identification of dyes. After QC was performed at Vinueza labs, the confirmed reactive, acid, and disperse dyes were approved and sent to the dyeing facility at the Wilson College of Textiles where single color, dichromatic fabrics, and black formulation fabrics would be produced.

Table 8. Quality control results on selected commercial dyes.

Commercial Name	Chemical Formula	Theoretical Exact Mass	Experimental Exact Mass	ion species (charge)	ppm Error
Disperse Blue 3	C17H16N2O3	296.1161	297.1239	[M+H](+1)	-0.98
Disperse Orange 3	C12H10N4O2	242.0804	243.0882	[M+H](+1)	-0.87
Disperse Orange 37	C17H15Cl2N5O2	391.0603	392.0681	[M+H](+1)	-0.66
Disperse Red 17	C17H20N4O4	344.1485	345.1563	[M+H](+1)	0.41
Cibacet yellow 2gc	C15H15N3O2	269.1164	270.1242	[M+H](+1)	-0.88
Reactive Yellow GR	C21H17ClN8O7S2	295.0102	295.0106	[M-2H](-2)	-1.36
Reactive Yellow RA	C26H20ClN7O10S3	377.4976	377.4974	[M-2H](-2)	0.53
Reactive Blue 5	C29H20ClN7O11S3	256.6618	256.6625	[M-3H](-3)	-2.73
Remazol Br. Red 3BS	C26H26FN9O13S4	408.5185	408.5184	[M-2H](-2)	0.24
Reactive Yellow 145	C28H22ClN9O12S4	418.4907	418.491	[M-2H](-2)	-0.71
Everzol Turquoise Blue G	C40H22CuN9O14S5Na3	537.9638	537.9644	[M-2Na+H](-2)	-1.39
Procion Red H-E3B	C44H30Cl2N14O20S6	678.9703	678.9562	[M-2H](-2)	1.71
Everzol Yellow 3GL	C20H20N4O7S2	294.0146	294.0143	[M-2H](-2)	3.05

Production of single-color and black fabrics with disperse and acid dyes

A total of 13 different fabrics were dyed with acid and disperse dyes. Among them, six nylon fabrics were produced with acid dye, including five single-color fabrics and one black fabric with composite formulation, and the rest of seven polyethylene terephthalate (PET) fabrics were dyed with disperse dye, which includes six single-color fabrics and one black fabric. An example of a detailed production procedure is described below.

All the substrate samples were scoured together in an atmospheric kettle heated to a simmer near 100 °C using 1 g/L of Invadine DA spin finish scour, 2 g/L soda ash (calcium carbonate) and 1 g/L Clarite ONE-AM surfactant. The bath and samples were agitated occasionally and circulated for 20 minutes before rinsing thoroughly following neutralization with acetic acid. The samples were then centrifuged to extract the water and dried in a circulating air oven at 40 °C.

Acid dye baths only include the dye solution and acetic acid to regulate the pH to a desirable level. The appropriate amounts of single dye samples or black formulation dye solution were added to 300 mL Ahiba Nuance beakers and the water level raised to 200 mL for around a 50:1 liquor ratio. The samples were wet with only water and padded at 4 bars to regulate dye strike and leveling before being loosely rolled and sealed inside the Nuance beakers. The temperature of the beaker dyeing machine was raised to 100 °C at 2.5 °C per minute and held for 45 minutes before cooling, rinsing, and drying.

Disperse dye baths only include the dye solution, acetic acid to regulate the pH to a desirable level, and a small amount of leveling agent (NT-9). The appropriate amounts of single dye samples or black formulation dye solution were added to 300 mL Ahiba Nuance beakers and the water level raised to 200 mL for around a 50:1 liquor ratio. The samples were wet with only water and padded at 4 bars to regulate dye strike and leveling before being loosely rolled and sealed inside the Nuance beakers. The temperature of the beaker dyeing machine was raised to 130 °C at 2.5 °C per minute and held for 60 minutes before cooling, rinsing, and drying.

In order to generate a formula for black fabrics, primary color data for each dye were read using an X-rite spectrophotometer and analyzed in Color iMatch (i7) software to predict black formulations for each dye

class. If the color of the combination sample was not close enough to black, adjustments were made to move the shade closer to the desired black and additional samples run to confirm the formula.

A total of 52 different samples of cotton, polyethylene terephthalate (PET), nylon and polyester-cotton-blend fabrics were dyed using confirmed commercial dyes (disperse, acid and reactive dyes) from Section A including 30 single color fabrics (single color with single type of dye), 10 monochromatic ratio fabrics (single color with two types of dyes at a ratio of 50:50, 80:20 and 99:1), 6 dichromatic ratio fabrics (a mix of two colors from two dyes at a ratio of 50:50, 80:20 and 99:1), and 6 black formula fabrics (a mixture of three dyes to generate black color). Among them disperse dyes were used on PET fabrics, acid dyes were used on nylon fabrics, and reactive dyes were used on cotton and polyester-cotton-blend fabrics. An example of the dyeing procedure was shown in the Appendix A. In order to generate a formula for black fabrics, primary color data for each dye were read using an X-rite spectrophotometer and analyzed in Color iMatch (i7) software to predict black formulations for each dye class. If the color of the combination sample was not close enough to black, adjustments were made to move the shade closer to the desired black and additional samples run to confirm the formula.

All of the fabric substrates were scoured together in an atmospheric kettle heated to a simmer near 100 °C using 1 gram per liter of Invadine spin finish scour, 2 gram per liter soda ash (sodium carbonate) and 1 gram per liter Clarite ONE-AM surfactant. The bath and samples were agitated occasionally and circulated for 20 minutes before rinsing thoroughly following neutralization with acetic acid. The samples were then centrifuged to extract the water and dried in a circulating air oven at 40 °C.

Disperse dye baths only include the dye solution, acetic acid to regulate the pH to a desirable level, and a small amount of leveling agent (NT-9). The appropriate amounts of dye solution were added to 300 mL Ahiba Nuance beakers and the water level raised to 200 mL for around a 50:1 liquor ratio. The samples were wet with only water and padded at 4 bars to regulate dye strike and leveling before being loosely rolled and sealed inside the Nuance beakers. The beaker dyeing machine was raised to 130 °C at 2.5 °C per minute and held for 60 minutes before cooling, rinsing, and drying.

Acid dye baths include the dye solution and acetic acid to regulate the pH to a desirable level. The appropriate amounts of acid dye solution and fabrics were added to 300 mL Ahiba Nuance beakers and the water level was filled to 200 mL for a liquor ratio around 50:1. The samples were wet with only water and padded at 4 bars to regulate dye strike and leveling before being loosely rolled and sealed inside the Nuance beakers. The beaker dyeing machine was raised to 100°C at 2.5°C per minute and held for 45 minutes before cooling, rinsing, and drying.

Reactive dye baths include the dye solution, sodium sulfate, and sodium carbonate. The appropriate amounts of reactive dye solution were added to 300 mL Ahiba Nuance beakers and the water level raised to 200 mL for around a 50:1 liquor ratio. The sodium sulfate was dissolved in the bath, and the samples were wet with only water and padded at 4 bars to regulate dye strike and leveling before being loosely rolled and placed in the beaker. The soda ash was then dissolved and the beakers and sealed and raised to 160 °C at 2.0 °C per minute and held for 60 minutes before cooling, rinsing, neutralizing, and drying. This all-in method was used because the samples were run in a closed machine; Usually reactive dyeing add alkali later in the process to control leveling, however, leveling was not of particular concern here.

A total of 17 additional fabrics were prepared, which includes 8 monochromatic (one color, two dyes of the same class), 6 dichromatic (two colors, two dyes of the same class) and 3 single dye acid and disperse samples were dyed. An example of a detailed production procedure is described below.

All the substrate samples were scoured together in an atmospheric kettle heated to a simmer near 100 °C using 1 g/L of Invadine DA spin finish scour, 2 g/L soda ash (sodium carbonate) and 1 g/L Clarite ONE-

AM surfactant. The bath and samples were agitated occasionally and circulated for 20 minutes before rinsing thoroughly following neutralization with acetic acid. The samples were then centrifuged to extract the water and dried in a circulating air oven at 40 °C.

Acid dye baths only include the dye solution and acetic acid to regulate the pH to a desirable level. The appropriate amounts of single dye samples or black formulation dye solution were added to 300 mL Ahiba Nuance beakers and the water level raised to 200 mL for around a 50:1 liquor ratio. The samples were wet with only water and padded at 4 bars to regulate dye strike and leveling before being loosely rolled and sealed inside the Nuance beakers. The temperature of the beaker dyeing machine was raised to 100 °C at 2.5 °C per minute and held for 45 minutes before cooling, rinsing, and drying.

Disperse dye baths only include the dye solution, acetic acid to regulate the pH to a desirable level, and a small amount of leveling agent (NT-9). The appropriate amounts of single dye samples or black formulation dye solution were added to 300 mL Ahiba Nuance beakers and the water level raised to 200 mL for around a 50:1 liquor ratio. The samples were wet with only water and padded at 4 bars to regulate dye strike and leveling before being loosely rolled and sealed inside the Nuance beakers. The temperature of the beaker dyeing machine was raised to 130 °C at 2.5 °C per minute and held for 60 minutes before cooling, rinsing, and drying.

Fiber reactive mixtures were dyed separately, the first run applying the disperse dyes as they require a higher temperature, and the second applying the reactive dyes. An all-in method was used to reactive dyeing as the process was carried out in a closed beaker, so all components were added simultaneously at the beginning of the cycle. The appropriate amount of reactive dye solution was added to each beaker along with 70g/L of sodium sulfate salt and enough water to bring the total volume to 200mL (approximately a 50:1 liquor ratio) and each sample loosely rolled and placed in the beaker. 15g/L of sodium carbonate was dissolved into the solution to fix the dye and each beaker sealed and run in an Ahiba Nuance for 45 minutes, heating at 2.5°C per minute to 60°C before cooling, rinsing, and drying.

In order to generate a formula for black fabrics, primary color data for each dye were read using an X-rite spectrophotometer and analyzed in Color iMatch (i7) software to predict black formulations for each dye class. If the color of the combination sample was not close enough to black, adjustments were made to move the shade closer to the desired black and additional samples run to confirm the formula.

In this phase of the project, a total of 14 additional fabrics were prepared, which includes 5 monochromatic (one color, two dyes of the same class), 6 dichromatic (two colors, two dyes of the same class) and 3 single dyes, reactive and disperse samples were dyed.

All the substrate samples were scoured together in an atmospheric kettle heated to a simmer near 100 °C using 1 g/L of Invadine DA spin finish scour, 2 g/L soda ash (sodium carbonate) and 1 g/L Clarite ONE-AM surfactant. The bath and samples were agitated occasionally and circulated for 20 minutes before rinsing thoroughly following neutralization with acetic acid. The samples were then centrifuged to extract the water and dried in a circulating air oven at 40 °C.

Disperse dye baths only include the dye solution, acetic acid to regulate the pH to a desirable level, and a small amount of leveling agent (NT-9). The appropriate amounts of single dye samples or dichromatic formulation dye solution were added to 300 mL Ahiba Nuance beakers and the water level raised to 200 mL for around a 50:1 liquor ratio. The samples were wet with only water and padded at 4 bars to regulate dye strike and leveling before being loosely rolled and sealed inside the Nuance beakers. The temperature of the beaker dyeing machine was raised to 130 °C at 2.5 °C per minute and held for 60 minutes before cooling, rinsing, and drying.

To reactive dyeing as the process was carried out in a closed beaker, all components were added simultaneously at the beginning of the cycle. The appropriate amount of reactive dye solution was added to each beaker along with 70 g/L of sodium sulfate salt and enough water to bring the total volume to 200 mL (approximately a 50:1 liquor ratio) and each sample loosely rolled and placed in the beaker. 15 g/L of sodium carbonate was dissolved into the solution to fix the dye and each beaker sealed and run in an Ahiba Nuance for 45 minutes, heating at 2.5 °C per minute to 60 °C before cooling, rinsing, and drying.

In this phase of the project, 12 additional fabrics were prepared, which includes 5 monochromatic (one color, two dyes of the same class), 3 dichromatic (two colors, two dyes of the same class), and 4 single dye, reactive, acid and disperse samples were dyed (Table 9). Single and dichromatic fabrics were dyed at three different concentrations (Table 9) to give a total of 28 dyed fabrics.

Table 9. Single and dichromatic dyed fabrics.

Fabric	Dye	Dye concentration on fabrics (%)
1	Reactive Red 123	100
2	Reactive Red 2	100
3	Reactive Blue 4	100
4	Reactive Yellow 86	100
5	Reactive Blue 4:Reactive Red 123	50:50, 80:20, 99:1
6	Reactive Blue 4: Reactive Yellow 86	50:50, 80:20, 99:1
7	Reactive Blue 123:Reactive Red 2	50:50, 80:20, 99:1
8	Disperse Blue 60 : Disperse Red 153	50:50, 80:20, 99:1
9	Disperse Blue 60: Disperse Blue 77	50:50, 80:20, 99:1
10	Disperse Yellow 211: Disperse Yellow 64	50:50, 80:20, 99:1
11	Acid Blue 62: Acid Blue 90	50:50, 80:20, 99:1
12	Acid Red 182: Acid Red 337	50:50, 80:20, 99:1

All the substrate samples were scoured together in an atmospheric kettle heated to a simmer near 100 °C using 1 g/L of Invadine DA spin finish scour, 2 g/L soda ash (sodium carbonate) and 1 g/L Clarite ONE-AM surfactant. The bath and samples were agitated occasionally and circulated for 20 minutes before rinsing thoroughly following neutralization with acetic acid. The samples were then centrifuged to extract the water and dried in a circulating air oven at 40 °C.

Disperse dye baths only include the dye solution, acetic acid to regulate the pH to a desirable level, and a small amount of leveling agent (NT-9). The appropriate amounts of single dye samples or dichromatic formulation dye solution were added to 300 mL Ahiba Nuance beakers and the water level raised to 200 mL for around a 50:1 liquor ratio. The samples were wet with only water and padded at 4 bars to regulate dye strike and leveling before being loosely rolled and sealed inside the Nuance beakers. The temperature of the beaker dyeing machine was raised to 130 °C at 2.5 °C per minute and held for 60 minutes before cooling, rinsing, and drying.

To reactive dyeing as the process was carried out in a closed beaker, all components were added simultaneously at the beginning of the cycle. The appropriate amount of reactive dye solution was added to each beaker along with 70g/L of sodium sulfate salt and enough water to bring the total volume to 200mL (approximately a 50:1 liquor ratio) and each sample loosely rolled and placed in the beaker. 15g/L of sodium carbonate was dissolved into the solution to fix the dye and each beaker sealed and run in an Ahiba Nuance for 45 minutes, heating at 2.5°C per minute to 60°C before cooling, rinsing, and drying.

Acid dye baths only include the dye solution and acetic acid to regulate the pH to a desirable level. The appropriate amounts of single dye samples or black formulation dye solution were added to 300 mL Ahiba

Nuance beakers and the water level raised to 200 mL for around a 50:1 liquor ratio. The samples were wet with only water and padded at 4 bars to regulate dye strike and leveling before being loosely rolled and sealed inside the Nuance beakers. The temperature of the beaker dyeing machine was raised to 100 °C at 2.5 °C per minute and held for 45 minutes before cooling, rinsing, and drying.

Detection of disperse dye from polyester fabrics via Direct Analysis of Real-Time (DART) and Quadrupole Time-Of-Flight (QTOF) mass spectrometry

Sample-prep-free analyses via Direct Analysis in Real-Time (DART) and Quadrupole Time-Of-Flight (QTOF) mass spectrometry were performed on single color fabrics and black formula fabrics. A DART-SVP100 probe using helium discharge gas was obtained from IonSense®. The results suggested that the combination of DART with QTOF mass spectrometry could detect and identify disperse dyes directly from a single colored fabric’s thread with minimal sample preparation. This system was also able to detect and identify three different disperse dyes simultaneously and rapidly from black thread samples.

A diagram explaining the ionization mechanism of DART is shown in Figure 1. Inert helium gas atoms are excited into a metastable state by the glow discharge generated by a high voltage needle. The excited gas then flows through a ceramic heater where the gas is heated to a certain temperature (in this experiment, the temperature was set to 350 °C) controlled by Graphical-User-Interface (GUI) before exiting through the exit grid. The exit grid is charged to filter out any charged particles, leaving only the metastable helium atom. Finally, the gas flow reaches the sample and heated metastable helium atoms will react with water vapor in the atmosphere and sample molecules, generating protonated molecules or molecular ions through a series of sequential reactions shown in Figure 1. The DART source was custom-mounted to the ionization source interface of Agilent 6520B Q-TOF high-resolution mass spectrometer. Three sets of adjustable screws with three rulers were used to adjust the position and tilting of the discharge gas outlet. 2 cm thread samples were removed from different fabrics and mounted on an IonSense® Quick Strip™ sample card. A picture of this sample card is shown in Figure 2.

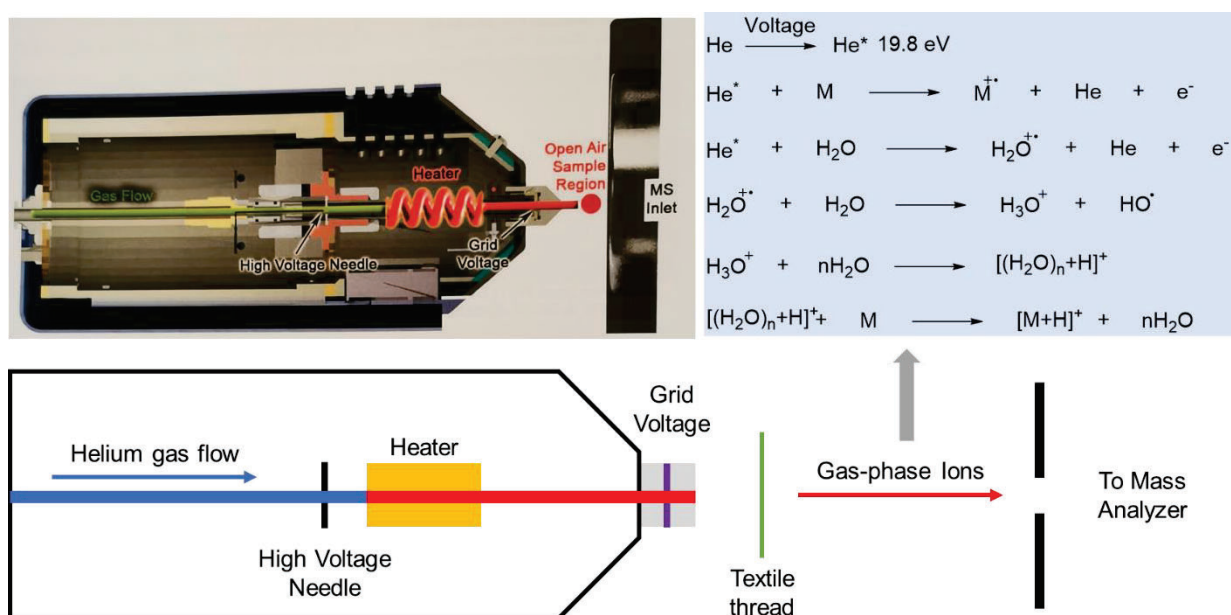


Figure 1. Diagram explaining the design and ionization mechanism of DART ionization source.

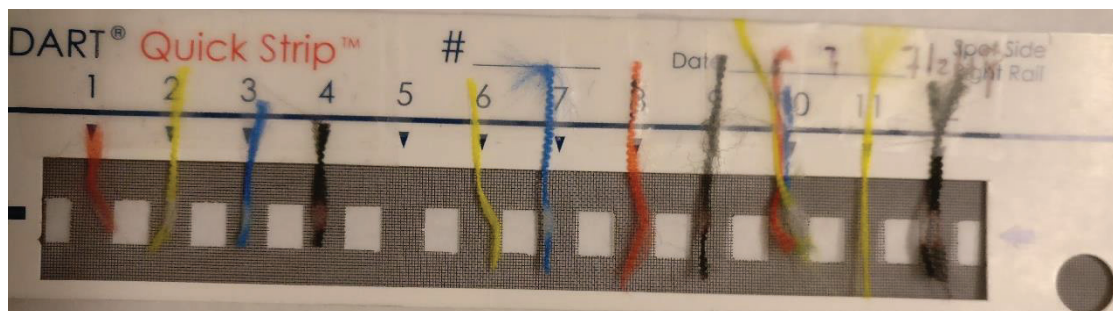


Figure 2. Photo showing threads mounted on IonSense® Quick Strip™ sample card after DART-QTOF analyses.

Results from DART-QTOF analyses on single color fabrics are summarized in Figure 3. Three thread samples obtained from PET fabrics dyed with three different disperse dyes were tested including C.I. Disperse Red 153, C.I. Disperse Yellow 211 and C.I. Disperse Blue 56. From the sample of C.I. Disperse Red 153 (shown as sample A in Figure 3), a signal with a mass-to-charge ratio of 404.0499 was detected by QTOF and the m/z difference between isotopic distribution peaks suggested that it was a singly charged ion. Thus, this m/z signal was generated by an ion with an exact mass of 404.0499. Then, by using the formula generation function in Agilent MassHunter Qualitative analysis software, a formula of $C_{18}H_{15}Cl_2N_5S$ was obtained with a relative mass measurement error of 0.38 ppm (parts-per-million), which matches with the chemical formula of C.I. Disperse Red 153. Besides identification by exact mass and chemical formula, tandem mass spectrometry tests were also performed. By colliding this ion with nitrogen gas and studying its fragmentation patterns, the identification of C.I. Disperse Red 153 from sample A was reinforced by fragmentation patterns obtained from Collision-Induced-Dissociation (CID). Using similar methodology, C.I. Disperse Yellow 211 and C.I. Disperse Blue 56 were also identified from samples B and C, respectively. The results suggest that the combination of DART with QTOF mass spectrometry could detect and identify the disperse dyes directly from the corresponding fabric threads with minimal sample preparation. Another observation from Figure 3 is bleaching of fabrics at the bottom of each thread, suggesting that during ionization, high-temperature helium gas flow coming from the DART probe is able to remove some amount of disperse dye from fabrics.

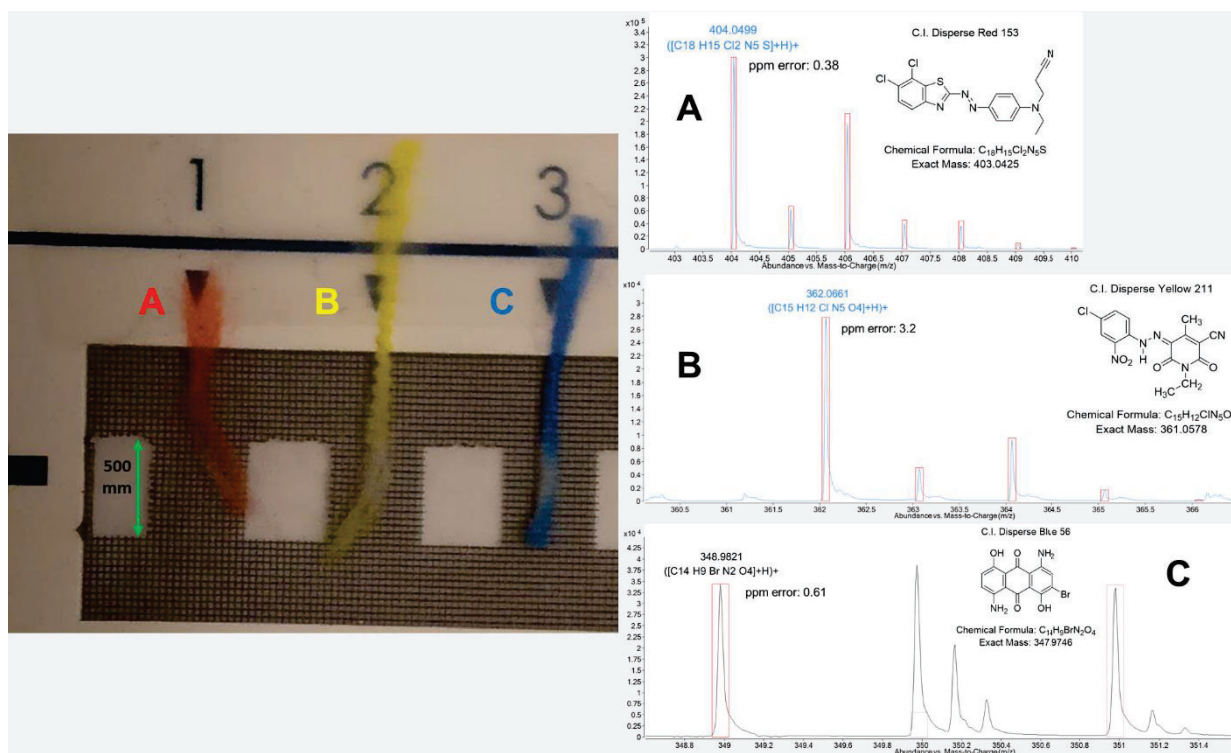


Figure 3. Mass spectra obtained from DART-QTOF analyses on single color PET threads.

Results from DART-QTOF analyses on black fabrics are summarized in Figure 4. Following the same analysis procedure described in the last section, the identification of C.I. Disperse Red 153, C.I. Disperse Yellow 211 and C.I. Disperse Blue 56 from a black thread sample were accomplished based on exact mass, chemical formula, isotropic distribution, and fragmentation patterns obtained from CID. This suggests that the combination of DART with QTOF mass spectrometry could rapidly (average sample analysis time for is less than 30 seconds) and simultaneously identify the different dye components in a black thread sample. Another observation from Figure 4 is the bleaching of the thread; Similar to the bleaching observed on single color thread analyses, black thread samples after DART-QTOF analyses also showed a loss of color as helium gas flow coming from DART is able to remove the dyes from thread and ionize them.

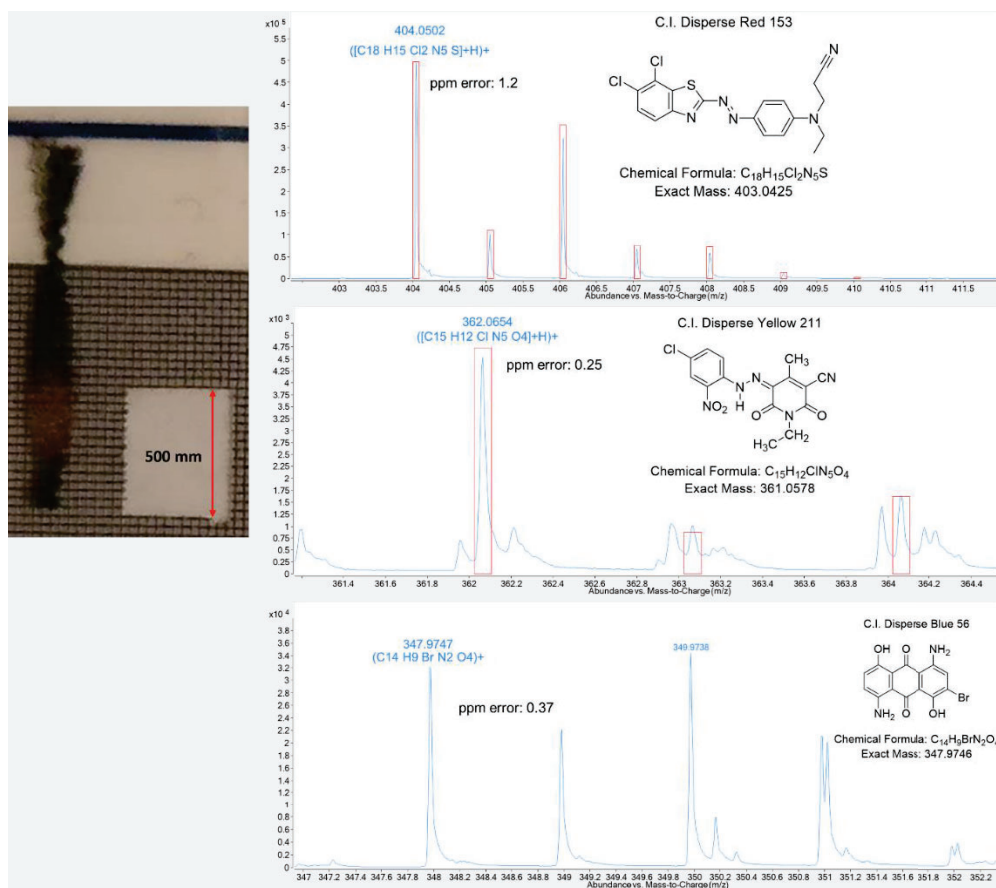


Figure 4. Mass spectra obtained from DART-QTOF analyses on single color PET threads.

Production of single-color, dichromatic trichromatic fabrics with disperse and reactive dyes

Approximately 10 cm by 10 cm cotton, polyester, and nylon fabric samples were exhaust dyed in a laboratory beaker dyeing machine (Ahiba Nuance, Datacolor, NJ, USA) using methodology outlined in previous reports, see Table 10. A post scour was performed to remove excess, unreacted dye from the fiber's surface before shipment and analysis. 134 fabric samples in total were generated for this project; refer to Tables below for fabric samples generated using commercial dyes (all samples dyed at NC State)

Table 10. Dyes to be investigated in mixtures.

No.	Name	Type	Color	Vendor
1	Red 123	Reactive	Red	DyStar
2	Blue 4	Reactive	Blue	DyStar
3	Yellow 86	Reactive	Yellow	DyStar
4	Red 2	Reactive	Red	DyStar
5	Red 82	Disperse	Red	Huntsman Corporation
6	Blue 56	Disperse	Blue	DyStar
7	Yellow 211	Disperse	Yellow	Huntsman Corporation
8	Yellow 64	Disperse	Yellow	DyStar
9	Red 153	Disperse	Red	Huntsman Corporation
10	Blue 60	Disperse	Blue	Huntsman Corporation
11	Blue 77	Disperse	Blue	Huntsman Corporation
12	Red 60	Disperse	Red	DyStar
13	Blue 62	Acid	Blue	DyStar

14	Orange 67	Acid	Orange	Hunstman Corporation
15	Red 337	Acid	Red	DyStar
16	Yellow 49	Acid	Yellow	DyStar
17	Blue 90	Acid	Blue	Standard Dyes, Inc
18	Red 182	Acid	Red	DyStar

We will also prepare mixtures of these dyes to determine the concentrations that can be detected by ICERS. After preparing and measuring the initial binary dye mixtures shown in Table 11, we will use Design-of-Experiment (DOE) to decide on subsequent mixtures to determine the lowest concentration of minor dye components that can be detected in binary mixtures.

Table 11. Initial binary reactive dye mixtures (ratio in 3% total).

Sample	Dye 1	Dye 2	Sample	Dye 2	Dye 3	Sample	Dye 1	Dye 4
A1	99	1	D1	1	99	G1	1	99
B1	80	20	E1	20	80	H1	20	80
C1	50	50	F1	50	50	I1	50	50

Once the minimum identifiable concentrations of binary mixtures have been determined, we will prepare ternary mixtures using dyes 1, 2, and 3. The initial mixtures are shown in Table 12.

Table 12. Initial ternary reactive dye mixtures (weight percent).

Sample	Dye 1	Dye 2	Dye 3	Sample	Dye 1	Dye 2	Dye 3
J1	1.293%	12.63%	5.678%				
K1	12.82%	3.323%	6.648%				

Once these have been analyzed, we will refine further mixtures using DOE. Next, the same process will be repeated with the dispersive dyes, see Table 13 and Table 14 .

Table 13. Initial binary disperse dye mixtures (ratio in 3% total).

Sample	Dye 9	Dye 10	Sample	Dye 10	Dye 11	Sample	Dye 7	Dye 8
A2	99	1	D2	1	99	G2	1	99
B2	80	20	E2	20	80	H2	20	80
C2	50	50	F2	50	50	I2	50	50
Sample	Dye 9	Dye 12	Sample	Dye 7	Dye 10			
J2	1	99	M2	99	1			
K2	20	80	N2	80	20			
L2	50	50	O2	50	50			

Table 14. Initial ternary disperse dye mixtures (weight percent).

Sample	Dye 6	Dye 7	Dye 9	Sample	Dye 6	Dye 7	Dye 12
P2	2.186 %	0.525 %	0.991%	R2	1.941%	0.714%	1.598%
Q2	3%	1%	1%				
Sample	Dye 5	Dye 6	Dye 7				
S2	0.542%	1.928%	0.063				
					T3	80	20
					U3	93	7
					V3	100	0

Table 15. Initial binary acid dye mixtures (ratio in 3% total).

Sample	Dye 13	Dye 17	Sample	Dye 13	Dye 15	Sample	Dye 13	Dye 16
A3	1	99	D3	1	99	G3	1	99
B3	20	80	E3	20	80	H3	80	20
C3	50	50	F3	50	50	I3	50	50

Sample	Dye 15	Dye 18	Sample	Dye 14	Dye 16	Sample	Dye 15	Dye 16
J3	99	1	M3	99	1	P3	0	100
K3	80	20	N3	80	20	Q3	7	93
L3	50	50	O3	50	50	R3	20	80
						S3	50	50
						T3	80	20
						U3	93	7
						V3	100	0

Table 16. Initial ternary acid dye mixtures (weight percent).

Sample ID	Dye 13	Dye 15	Dye 16	Sample	Dye 13	Dye 14	Dye 15
W3	1.5%	1%	1.526%	Y3	1.19%	1.435%	0.269%
X3	2%	1.5%	1.526%				

Table 17. Combined reactive and disperse dye mixtures on poly-cotton blend fabric (A4) and grid fabric (A5) (ratio in 3% total).

Sample ID	Dye 2	Dye 3	Dye 4	Dye 8	Dye 9	Dye 10
A4 / A5	50					50
B4 / B5	80					20
C4 / C5	99					1
D4 / D5		50		50		
E4 / E5		80		20		
F4 / F5		99		1		
G4 / G5			50		50	
H4 / H5			80		20	
I4 / I5			99		1	

Table 18. Fabrics dyed with a single dye for initial readings.

Dye (Sample)	Dye Class	Dye (Sample)	Dye Class	Dye (Sample)	Dye Class
Blue 4	Reactive	Red 4	Disperse	Black 58	Acid
Blue 19	Reactive	Red 15	Disperse	Black 172	Acid
Orange 16	Reactive	Red 60	Disperse	Blue 62	Acid
Orange 107	Reactive	Red 73	Disperse	Blue 90	Acid
Red 2	Reactive	Red 82	Disperse	Blue 260	Acid
Red 21	Reactive	Red 86	Disperse	Green 28	Acid
Red 123	Reactive	Red 153	Disperse	Orange 7	Acid
Yellow 86	Reactive	Red 367	Disperse	Orange 67	Acid
Blue 56	Disperse	Violet 28	Disperse	Red 131	Acid
Blue 60	Disperse	Yellow 64	Disperse	Red 182	Acid
Blue 77	Disperse	Yellow 82	Disperse	Red 337	Acid
Blue 287	Disperse	Yellow 114	Disperse	Yellow 49	Acid
Blue 291	Disperse	Yellow 211	Disperse	Yellow 79	Acid
Orange 73	Disperse			Yellow 199	Acid

Table 19. Cotton fibers dyed using mixtures of reactive dyes (ratio in 3% total) combined table.

Sample ID	Dye 1	Dye/ 2	Dye 3	Dye 4
A1	99	1		
B1	80	20		
C1	50	50		
D1		1	99	
E1		20	80	
F1		50	50	
G1	1			99
H1	20			80
I1	50			50
J1	6.6	64.4	29	
K1	56.7	14.7	28.6	
L1				

Table 20. Polyester fibers dyed using mixtures of disperse dyes (ratio in 3% total) combined table.

Sample ID	Dye 5	Dye 6	Dye 7	Dye 8	Dye 9	Dye 10	Dye 11	Dye 12
A2					99	1		
B2					80	20		
C2					50	50		
D2						1	99	
E2						20	80	
F2						50	50	
G2			1	99				
H2			20	80				
I2			50	50				
J2					1			99
K2					20			80
L2					50			50
M2			99			1		
N2			80			20		
O2			50			50		
P2		59	14.2		26.8			
Q2		60	20		20			
R2		45.6	16.8					37.6
S2	21.4	76.1	2.5					

Table 21. Nylon fibers dyed using mixtures of acid dyes (ratio in 3% total) combined table.

Sample ID	Dye 13	Dye 14	Dye 15	Dye 16	Dye 17	Dye 18
A3	1				99	
B3	20				80	
C3	50				50	
D3	1		99			
E3	20		80			
F3	50		50			
G3	1			99		
H3	80			20		
I3	50			50		

J3			99			1
K3			80			20
L3			50			50
M3		99		1		
N3		80		20		
O3		50		50		
P3			0	100		
Q3			7	93		
R3			20	80		
S3			50	50		
T3			80	20		
U3			93	7		
V3			100	0		
W3	37.3		24.8	37.9		
X3	39.8		29.8	30.4		
Y3	41.1	49.6	9.3			

Direct Analysis on Real-Time (DART) mass spectrometry of polyester dyed fabrics

The direct collection of disperse dye spectra from dyed fibers was completed using an IonSense DART-SVP100 (Direct Analysis in Real-Time) using helium discharge gas set to 300-350 °C. Fibers were introduced to the ionization stream using tweezers and mounting fibers on an IonSense mesh sample card. The back of the source was aligned with the 10.5 cm mark on the scale for the x-axis used for positioning, which creates a 1cm spacing between the probe gas outlet and the mass spectrometer interface. The alignment of the gas stream and the MS inlet was adjusted to be approximately 50% off-set (gas stream running above the inlet) to prevent excess He gas flow and sample into the instrument.

Temperature trials (200 °C, 250 °C, 300 °C, 350 °C, 400 °C, 500 °C) were undertaken to determine temperature limitations on the polyester fibers used while retaining dye transfer to the mass spectrometer. The state of single polyester fibers and the abundance of a test dye at each temperature were collected to determine the optimum temperature for analysis. Significant fiber degradation occurs at and above 350 °C, with these higher temperatures almost instantaneously melting and shrinking up the fiber. 300 °C and below caused little to no damage following exposure even as long as 20 to 30 seconds. Within 30 seconds, however, there is some bleaching of the fibers (to increasing degrees with increasing temperature) over time as dye molecules are dislodged. A comparable abundance of dye ions was found between 250 and 350, so a temperature of 300 °C would be best, with the use of 350 °C as needed (some fibers may require a higher temperature to dislodge dye molecules).

The DART-MS methodology correctly identified both single dyes and dye mixtures applied to polyester fibers. Clear spectra were generated for mixtures of varying concentrations of two components, as well as all three components of a black mixture (red, yellow, and blue at appropriate concentrations to generate the correct color). Refer to the sample identification tables (Table 15, Table 16, Table 17, Table 18, Table 19, Table 20, Table 21) document for information on what mixtures of disperse dyes were generated. A total of 37 commercial disperse dyes were sampled for confirmation, and 29 of these had a structure/exact mass confirmed.

The final data for the various dyes can be found in the updated tables below:

Table 22. High-Res LCMS ESI Mass Spectrometry Results: m/z ratio and characteristic information for fiber reactive dyes with confirmed identity and exact mass.

CI #	Exact Mass	MW	Chemical Formula	Observed Mass	Ion	ppm Error
RB 13	773.0072	774.16	C29H20ClN7O11S3	771.9995	[M-H](-1)	0.4
RB 19	484.0399	484.497	C22H16N2O7S2	483.0329	[M-H](-1)	0.62
RB 198	1447.8273	1450.89	C40H28Cl4N14O20S6 Na4	722.8973	[M-2H](-2)	-0.33
RB 2	877.0116	878.274	C31H24ClN9O12S4	291.3294	[M-3H](-3)	-1.66
RB 21	1076.9359	1078.529	C40H24CuN9O14S5	537.9644	[M-2H](-2)	1.3
RB 220	690.8948	672.113	C22H15CuN4O11S3Na	345.4486	[M-2H](-2)	3.47
RB 225	859.9662	861.1908	C28H19ClF2N8O12S4	858.9587	[M-H](-1)	-0.24
RB 4	635.969	637.4201	C23H14Cl2N6O8S2	634.963	[M-H](-1)	1.76
RB 49	815.0541	816.228	C32H26ClN7O11S3	406.5202	[M-2H](-2)	0.98
RB 5	773.0071	774.147	C29H20ClN7O11S3	256.6625	[M-3H](-3)	3.9
RB 71	1077.9421	1079.535	C40H25CuN9O14S5	538.9719	[M-2H](-2)	0.56
RBlk 5	796.9741	798.184	C27H20ClN7O12S4	352.4994	[M-2H](-2)	1.99
RO 107	424.0511	424.446	C16H16N4O6S2	423.0388	[M-H](-1)	-0.72
RO 16	475.0508	475.49	C20H17N3O7S2	474.0436	[M-H](-1)	0.21
RO 35	582.0073	582.569	C22H18N2O11S3	248.0064	[M-2H](-2)	2.82
RR 120	1333.9317	1336.047	C44H30Cl2N14O20S6 Na	678.9562	[M-2H](-2)	1.71
RR 123	600.994	601.938	C21H14ClF2N5O8S2	599.9864	[M-H](-1)	-0.67
RR 198	796.9741	798.184	C27H20ClN7O12S4	264.6512	[M-3H](-3)	-1.51
RR 2	567.944	571.3611	C19H12Cl2N6O7S2	565.9746	[M-H](-1)	-
RR 21	674.0447	674.67	C27H22N4O11S3	673.0366	[M-H](-1)	-1.19
RR 24	721.0122	722.115	C26H20ClN7O10S3	377.4974	[M-2H](-2)	0.53
RR 141	1704.7947	1707.199	C52H28Cl2N14Na5O26S8Na5	567.5917	[M-3H](-3)	0.38
RY 125	612.01	612.9638	C22H15ClF2N6Na2O7S2	304.9975	[M-2H](-2)	-1.22
RY 145	838.9959	840.24	C28H22ClN9O12S4	418.491	[M-2H](-2)	0.72
RY 15	492.0773	492.52	C20H20N4O7S2	491.0716	[M-H](-1)	3.05
RY 174	817.0371	817.7675	C26H24FN9O13S4	408.5184	[M-2H](-2)	-0.24
RY 176	838.9959	840.225	C28H22ClN9O12S4	418.4912	[M-2H](-2)	1.19
RY 3	592.035	592.986	C21H17ClN8O7S2	295.0106	[M-2H](-2)	1.36
RY 84	1743.8647	1746.285	C52H30Cl2N18Na4O26S8	435.4581	[M-4H](-4)	0.71
RY 86	621.986	623.393	C18H16Cl2N8O9S2	620.9713	[M-H](-1)	-0.64

Table 23. High-Res LCMS ESI Mass Spectrometry Results: m/z ratio and characteristic information for disperse dyes with confirmed identity and exact mass.

CI	Exact Mass	MW	Chemical Formula	Observed Mass	Ion	ppm Error	DART Mass*
DB 27	420.0958	420.377	C22H16N2O7	421.0885	[M+H](+1)	-0.33	
DB 287	448.1859	448.483	C23H24N6O4	449.1945	[M+H](+1)	-2.4	449.1901
DB 291	508.0706	509.317	C19H21BrN6O6	509.0784	[M+H](+1)	0.94	509.0725
DB 56	347.9746	349.14	C14H9BrN2O4	348.9813	[M+H](+1)	2.36	348.9776
DB 60	379.1168	379.372	C20H17N3O5	380.1243	[M+H](+1)	0.31	380.1087
DB 77	376.0695	376.0695	C20H12N2O6	377.0764	[M+H](+1)	2.2	377.0628
DB 79 :1	624.0816	625.3818	C23H25BrN6O10	625.0889	[M+H](+1)	-0.77	
DO 73	443.1594	443.463	C24H21N5O4	444.1665	[M+H](+1)	0.23	444.1540
DR 15	239.0582	239.23	C14H9NO3	240.0653	[M+H](+1)	-0.83	240.0587
DR 153	403.0425	404.313	C18H15Cl2N5S	404.0497	[M+H](+1)	0.19	404.0345
DR 167:1	505.1364	505.9073	C22H24ClN5O7	506.1438	[M+H](+1)	-0.99	
DR 367	486.1315	486.476	C28H22O8	487.1392	[M+H](+1)	-1.82	487.1313
DR 4	269.0688	269.256	C15H11NO4	270.076	[M+H](+1)	0.17	270.0823
DR 60	331.0845	331.327	C20H13NO4	332.092	[M+H](+1)	0.72	332.0916
DR 73	348.1335	348.366	C18H16N6O2	349.1415	[M+H](+1)	3.76	349.1377
DR 82	439.1492	439.428	C21H21N5O6	440.156	[M+H](+1)	0.07	440.1432
DR 86	422.455	422.455	C22H18N2O5S	423.1005	[M+H](+1)	3.14	423.0990
DV 28	305.9963	307.13	C14H8Cl2N2O2	306.9956	[M+H](+1)	1.82	306.9995
DY 114	424.0841	424.431	C20H16N4O5S	425.0902	[M+H](+1)	2.84	425.0865
DY 211	361.0578	361.742	C15H12ClN5O4	362.0652	[M+H](+1)	0.41	362.0638
DY 64	366.9844	366.9844	C18H10BrNO3	290.0813	[M+H](+1)	0.56	290.0814
DY 82	333.1477	333.391	C20H19N3O2	334.1548	[M+H](+1)	0.63	334.1515
DB 3	296.1161	296.3199	C17H16N2O3	297.1230	[M+H](+1)	-3.03	297.1125
DO 30	449.0658	450.2747	C19H17Cl2N5O4	450.0725	[M+H](+1)	-1.11	450.0663
DY 54	289.0739	289.2844	C18H11NO3	290.0813	[M+H](+1)	-1.38	290.0758
DO 29	377.1124	377.3529	C19H15N5O4	378.1191	[M+H](+1)	17.72	378.1124
DR 311	516.1605	516.4598	C22H24N6O9	517.161	[M+H](+1)	-14.12	517.1586
DB 183	474.1015	475.347	C20H23BrN6O3	475.0911	[M+H](+1)	-38.31	475.0830
DB 73	376.1059	376.368	C21H16N2O5	377.1155	[M+H](+1)	3.18	377.1068

Table 24. High-Res LCMS ESI Mass Spectrometry Results: m/z ratio and characteristic information for acid dyes with confirmed identity and exact mass.

CI #	Exact Mass	MW	Chemical Formula	Observed Mass	Ion	ppm Error
AB 62	400.1093	400.4490	C20H20N2O5S	399.1025	[M-H](-1)	1.27
AB 90	831.3012	832.0430	C47H49N3O7S2	830.2927	[M-H](-1)	0.80
ABk 172	439.0474	438.3980	C20H13N3O7S	924.0102	[2M-4H+Cr](-1)	-0.07
ABk 194	438.0401	439.3905	C20H13N3O7S	462.4980	[M-2H](-2)	0.86
ABk 52	438.0401	439.0401	C20H13N3O7S	307.3312	[2M-4H+Cr](-1)	-0.94
ABk 58	415.0838	415.4200	C19H17N3O6S	876.0824	[2M-4H+Cr](-1)	1.21
AG 40	802.0249	803.6340	C38H24Cl2N2O10S2	366.0432	[M-2H](-2)	2.51
AO 10	408.0086	408.3990	C16H12N2O7S2	407.0015	[M-H](-1)	0.59
AO 67	582.0879	582.6020	C26H22N4O8S2	581.0804	[M-H](-1)	0.39
AO 7	328.0518	327.3345	C16H13N2O4S	327.0446	[M-H](-1)	0.42
AR 182	343.0627	343.3570	C16H13N3O4S	741.0287	[2M-4H+Co](-1)	-0.28
AR 337	411.0501	411.3552	C17H12F3N3O4S	410.0435	[M-H](-1)	1.47
AY 199	428.0791	428.4190	C19H16N4O6S	427.0723	[M-H](-1)	-0.89
AY 246	517.0766	517.5740	C26H19N3O5S2	516.0688	[M-H](-1)	0.96
AY 49	425.0116	426.2720	C16H13Cl2N5O3S	424.0046	[M-H](-1)	0.43
AY 79	1066.1866	1067.1510	C47H42N10O12S4	1065.1784	[M-H](-1)	0.40
AR 111	786.1124	786.1124	C37H30N4O10S3	392.0492	[M-2H](-2)	0.77
AB 120	651.1246	651.7120	C33H25N5O6S2	324.5574	[M-2H](-2)	7.39
AR 447	717.0658	717.0658	C32H23N5O9S3	357.5252	[M-2H](-2)	-1.12
AR 361	518.1294	518.1294	C23H26N4O6S2	517.1232	[M-H](-1)	2.13
AB 113	637.1090	637.6850	C32H21N5Na2O6S2	317.5479	[M-2H](-2)	2.20
AY 159	444.0659	444.8900	C20H17CLN4O4S	443.0595	[M-H](-1)	2.03
AR 97	654.0879	654.6680	C32H222N4O8S2	653.0833	[M-H](-1)	4.13

PREPARATION AND CHARACTERIZATION OF INTEGRATING CAVITIES

Aerosil Powder

We purchased Evonik Aerosil OX 50 (fumed silica) for the preparation of integrating cavities. To determine if the material contained any adsorbed moisture, we conducted an FTIR analysis before and after a bake-out, see Figure 5. We do not observe any differences and as such decided to omit this step for the integrating cavity processing.

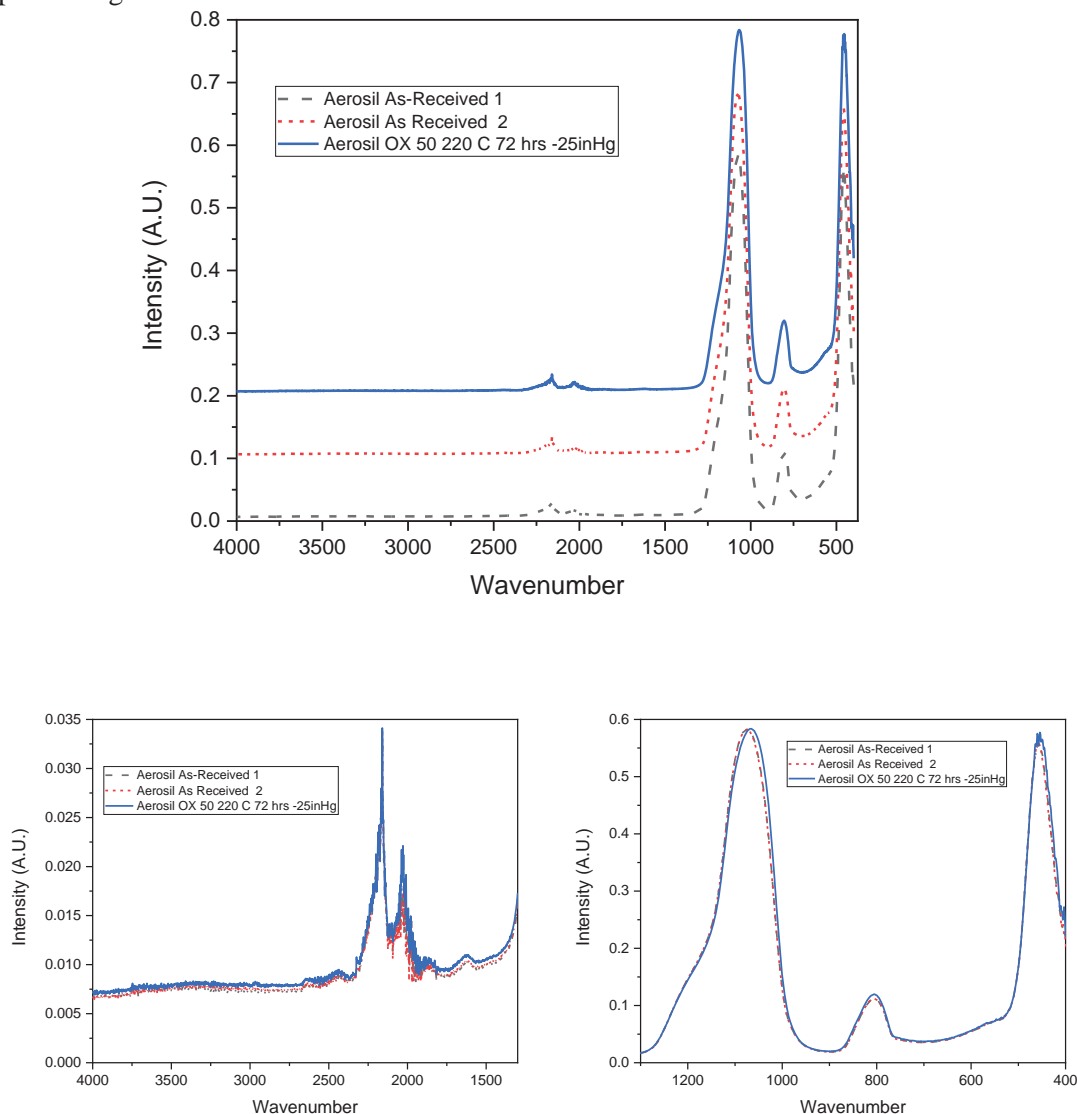


Figure 5. FTIR of Aerosil OX 50 before and after bake-out.

According to the dissertation by Cone, robust cylindrical parts with a cavity can be produced by applying a very modest pressure (30-1000) psi.²² For a 0.5" die, the lowest force that we can apply using the hydraulic pump is 500 lb or 2546.5 psi. Note that when a higher pressure is applied, the released part tends to chip and crumble. Figure 6 shows the quality of the pellets pressed at different pressures for 5 min: 2546.5 psi (500 lb), 5093.0 psi (1000 lb), and 10185.9 psi (2000 lb). At 10185.9 lb, the ejected pellet is brittle and readily crumbles.

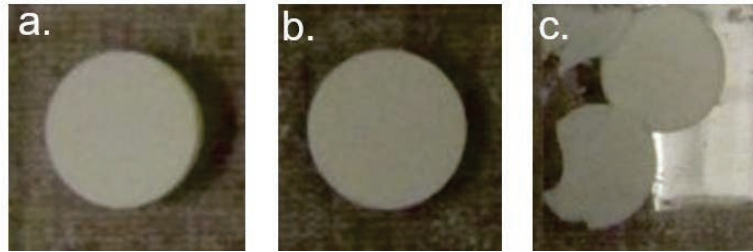


Figure 6. Aerosil powder pressed into 0.5” diameter pellets for 5 min at different pressures: (a) 500 lb, (b) 1000 lb, and (c) 2000 lb.

A lower pressure can be applied using a larger diameter die (1” diameter). Figure 7 shows the pellets obtained at different pressures: 636.6 psi (500 lb), 1273.2 psi (1000 lb), and 2546.5 psi (2000 lb). Robust pellets are obtained for all pressures. Slight chipping, however, occurs at the edge of the pellets.

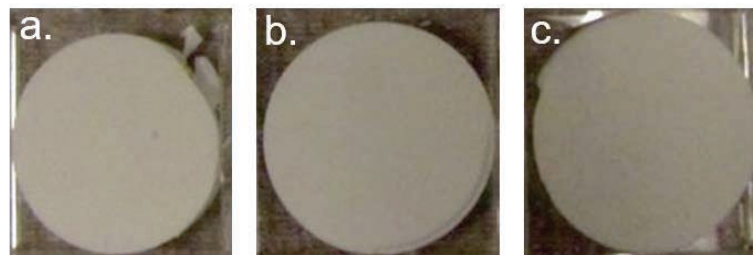


Figure 7. Aerosil powder pressed into 1” diameter pellets for 5 min at different pressures: (a) 500 lb, (b) 1000 lb, and (c) 2000 lb.

Next, we try to produce a part with a cavity. An inner cavity can be formed during packing using a removable part²². Here, we use a similar approach. We use a pushing rod with a cubical end to form a cubical cavity. The die diameter is 0.5”. The powder is pressed at pressures: 2546.5 psi (500 lb), 5093.0 psi (1000 lb), and 10185.9 psi (2000 lb). However, in all attempts the pressed part crumbled when ejected from the die (not shown). Alternatively, we retain the pressed part in the die after the powder is pressed; only the plunger is released. For the most part, the pressed part stayed robust, but the top part is partially chipped when the rod is released, see Figure 8.



Figure 8. Aerosil powder pressed at various pressures for 5 min to yield a part with a cavity: (a) 500 lb, (b) 1000 lb, and (c) 2000 lb.

Aerosil Powder with Binder

To yield a robust pressed powder, we introduce a 5% binder. As in the above process, we pressed the powder in a 0.5” die at different pressures: 2546.5 psi (500 lb), 5093.0 psi (1000 lb), and 10185.9 psi (2000 lb). In all case, robust pellets are obtained, see Figure 9.

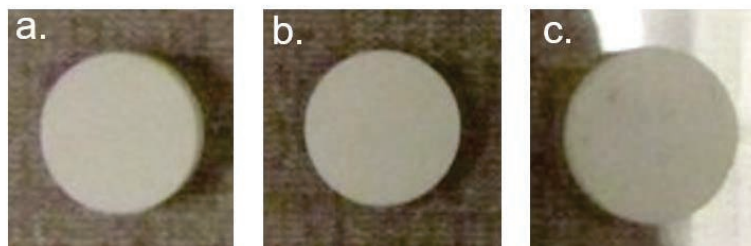


Figure 9. Aerosil powder with 5% binder pressed into 1” diameter pellets for 5 min at different pressures: (a) 500 lb, (b) 1000 lb, and (c) 2000 lb.

Next, we press the powder containing 5% binder with a pushing rod with a cubical end (Figure 10a) using a 10185.9 psi (2000 lb) pressure. We found that the released part chipped slightly. So, we increase the pressure to 12732.4 psi (2500 lb) to yield a robust cylindrical part with a cubical cavity (Figure 10b). The part remains robust following a 600 °C for 6 h heating that removes the polymeric binder (Figure 10c). Figure 11 shows that the presence of the binder, however, is not discernible from the FTIR spectra.

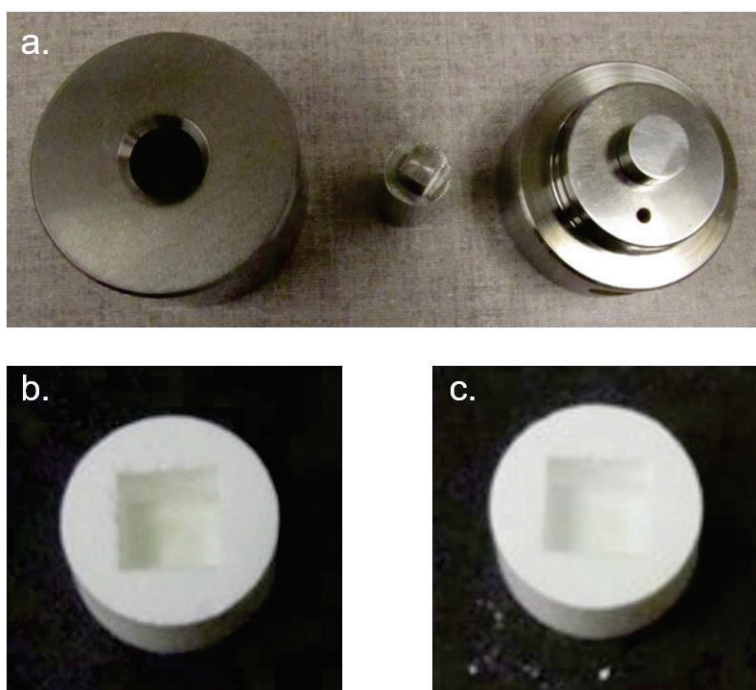


Figure 10. Pictures showing: (a) four-part die used to produce the cylindrical part with a cuboid cavity, (b) as-prepared and (c) baked (600 °C for 6 h) Aerosil/binder.

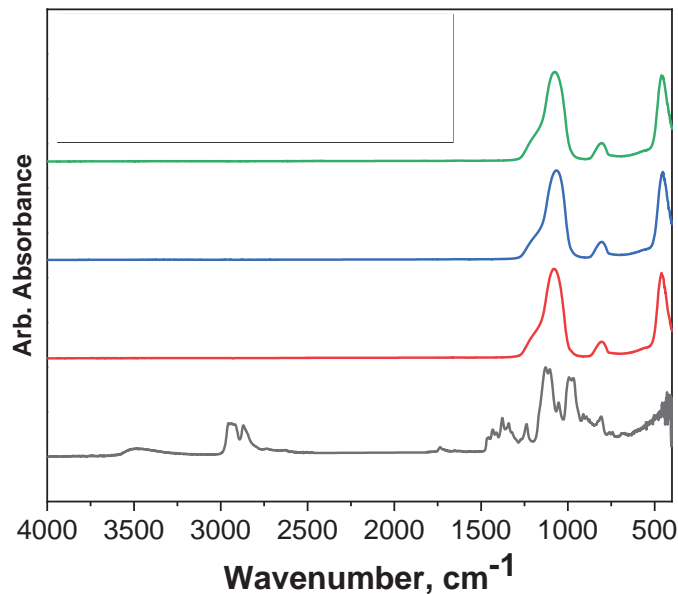


Figure 11. FTIR spectra of pure Aerosil, pure binder, and unbaked and baked Aerosil/binder powder.

To better understand the processing conditions for this material, we pressed larger parts (4" diameter) and then subjected them to a high-temperature bake-out. Figure 12 shows an image of the part being pressed and the temperature profile for the bake-out. The bake-out resulted in a slight volume expansion and we re-pressed the material to its original volume.

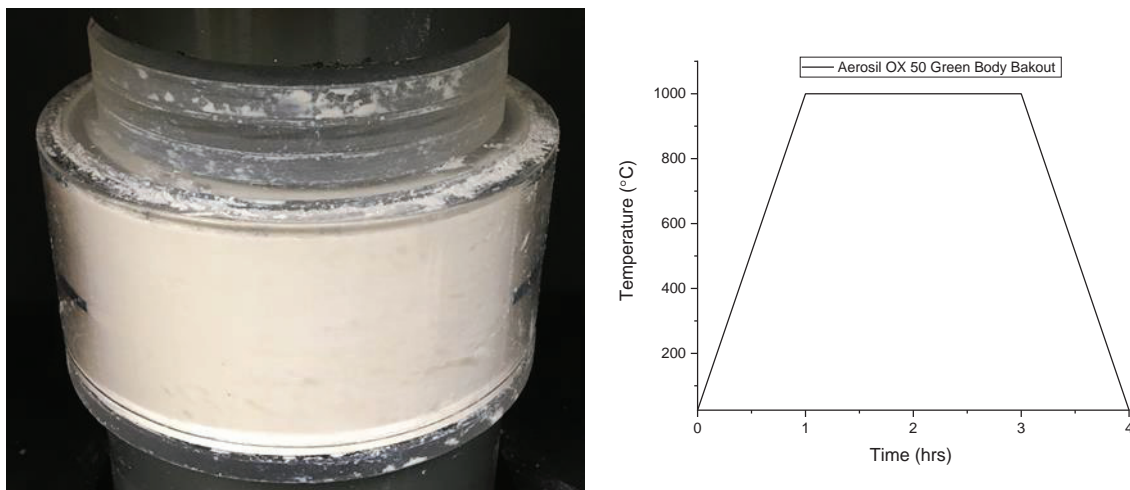


Figure 12. 4" diameter part during pressing (left) and temperature profile for subsequent bake-out (right).

We compared cavities made from multiple materials, including Aerosil OX 50 (Evonik), PTFE (Spectralon, Thorlabs), Accuflect B6 (Accuratus), and HOD-500 (Heraeus), see Figure 13 and Figure 14. The Accuratus and Heraeus materials were purchased as disks and then machined by us to fabricate cavities, while the Spectralon material was purchased as a cavity. The Aerosil material was purchased as a powder and then processed (with and without binders), pressed in different shapes, and sometimes sintered at various temperatures. Some additional powder processing information was presented in a previous report.

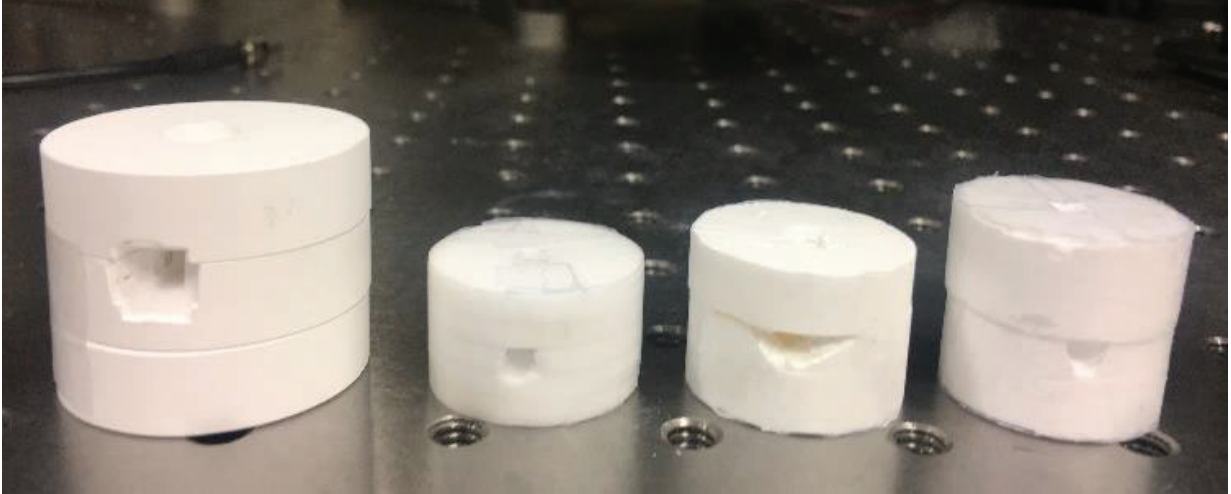


Figure 13. Image of different cavities. From left to right: Accuratus, Heraeus, Aerosil + 5% binder w/o sintering, Aerosil + 5% binder + 1050 °C, 1 hr sintering.

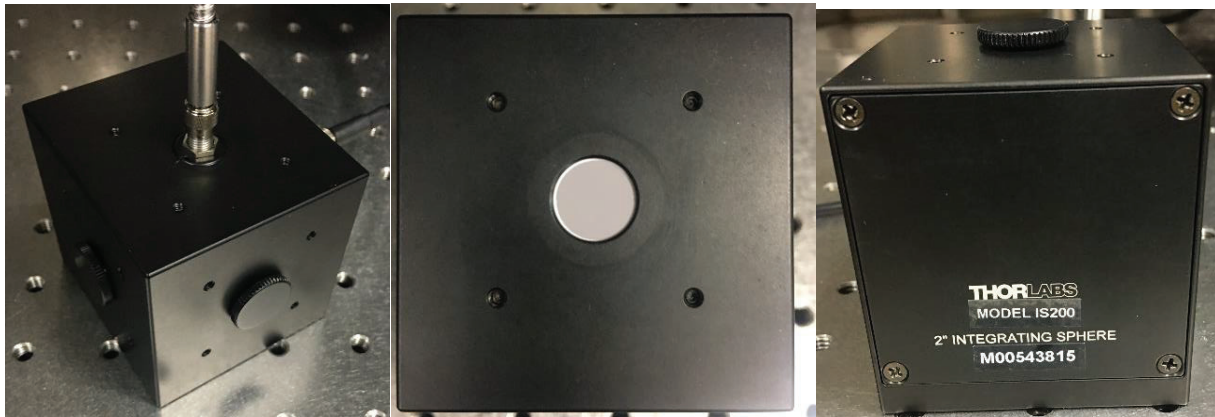


Figure 14. Thorlabs 2" IS 200 integrating sphere used for reference measurements.

Additional images of the cavities and their integration with optical fibers are shown in Figure 15, Figure 16, Figure 17, and Figure 18.

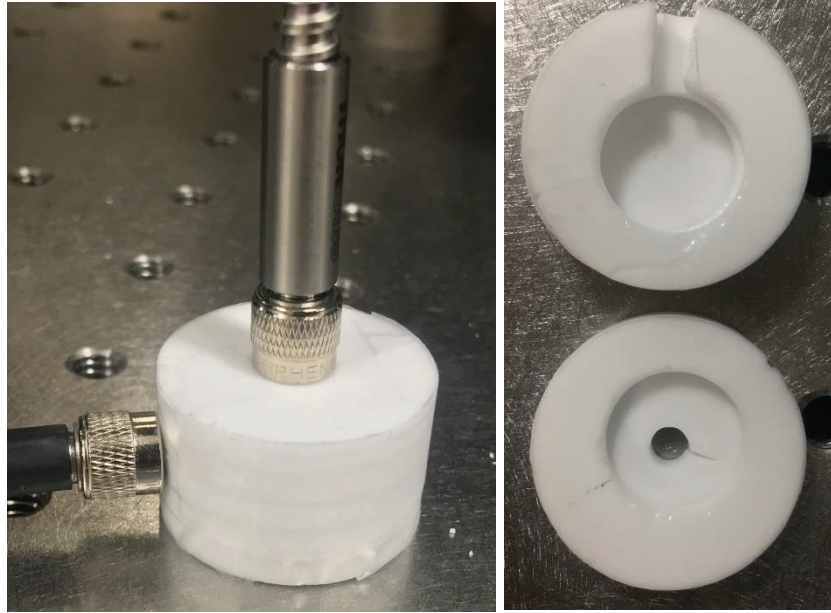


Figure 15. Heraeus HOD-500 cavity with attached optical fibers. This material is very hard, and machining takes extra time.

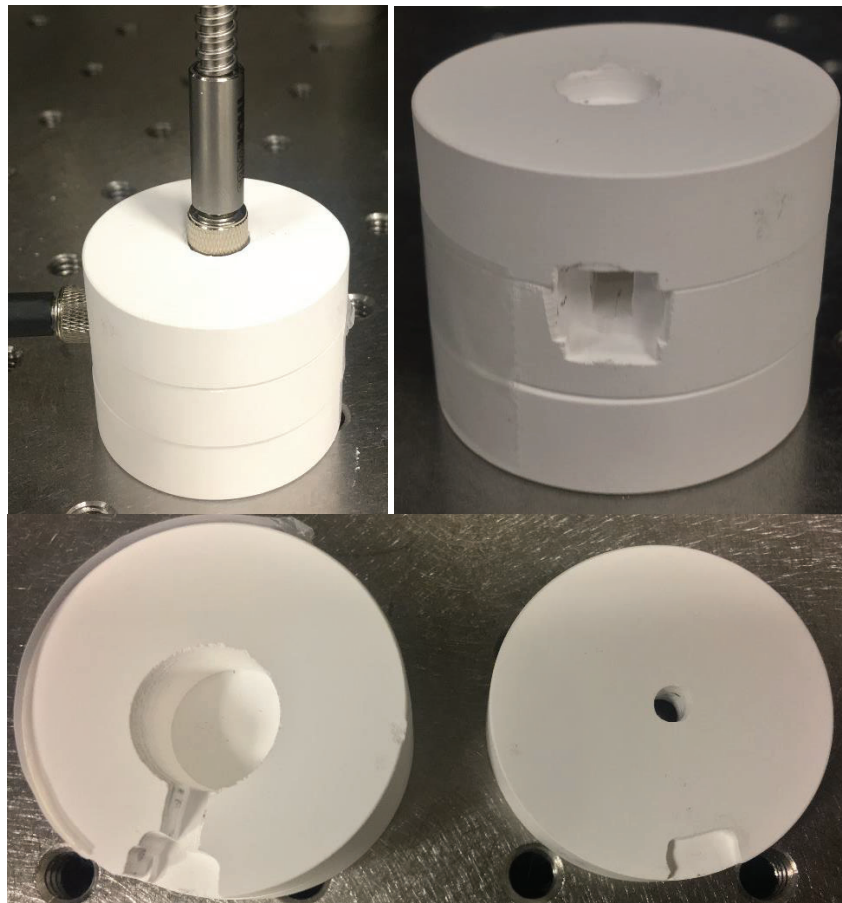


Figure 16. Accuratus Accuflect cavity with attached optical fiber. This material is significantly softer than the Heraeus material and easier to machine.



Figure 17. Aerosil OX 50 cavity w/5wt% binder with attached optical fiber. Without sintering, this material is very brittle and tends to crumble.

The Heraeus material is a very hard ceramic and requires care during machining to prevent breakage. The Accuratus material, on the other hand, is significantly softer and easier to machine. The Aerosil material requires us to form and press the powder into desired shapes. Without using a binder, this material shows very strong “spring-back” and it is very difficult to fabricate any pressed form, see Figure 17. We found, however, that a subsequent burnout, followed by a sintering step leads to pressed forms that are stable enough for subsequent machining, see Figure 18.



Figure 18. Aerosil OX 50 cavity w/5wt% binder, sintered at 1050 °C for 1 hr, with attached optical fiber. The sintered material is more stable and easier to machine.

While absolute diffuse reflectivities and cavity ringdown measurements are still in progress, Figure 19 shows a comparison of the relative diffuse reflectivity of various cavity materials with respect to standard Spectralon. The Heraeus material is less reflective than Spectralon over the whole wavelength range, while the Accuratus material has higher reflectivities for wavelengths above about 365 nm. The inhouse prepared Aerosil samples have higher reflectivities for shorter wavelength, with the sintered material performing better than the non-sintered material.

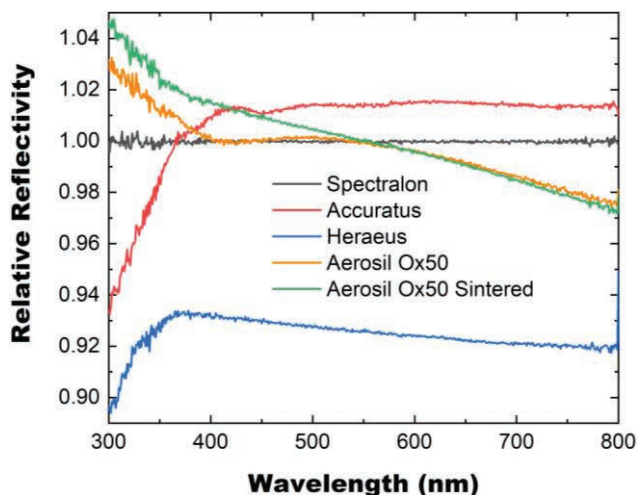


Figure 19. Comparison of diffuse reflectance of various cavity materials with respect to Spectralon (right).

Figure 20 shows the FTIR spectra of the as-received Aerosil material, the as-received Aerosil material blended with binder, and the as-received Aerosil material blended with binder and subsequently sintered at 1050 °C for 1 hour. There is no apparent difference in the spectra, indicating that processing the material with a binder and subsequently sintering it, does not impact the chemical properties of the material.

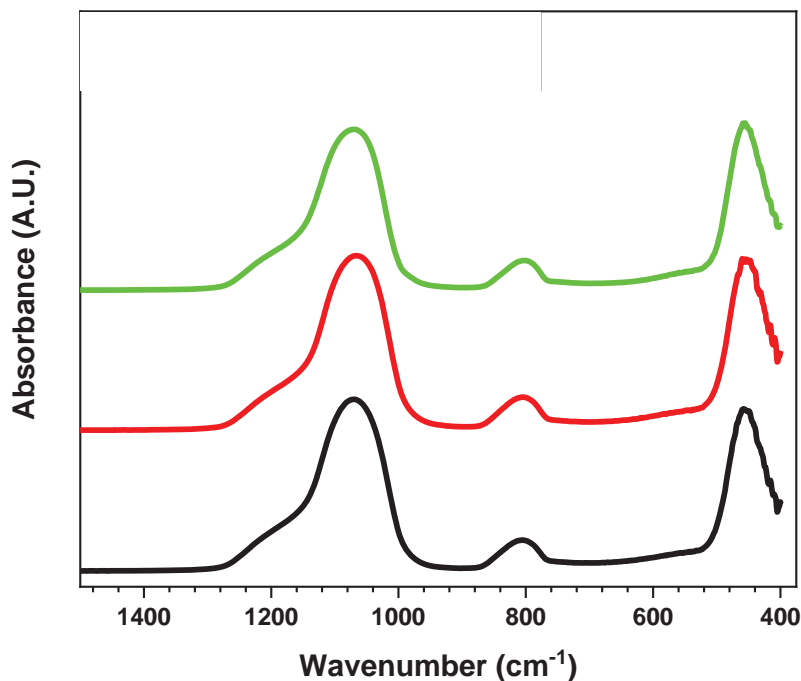


Figure 20. FTIR of Aerosil OX 50 processed under different conditions. No changes in the material can be observed after the addition of 5 wt% PVBA (Poly(vinyl butyral-co-vinyl-alcohol-covinyl acetate)) binder and after sintering at 1050 °C for 1 hour.

Figure 21 compares the FTIR spectra of the different cavity materials. The spectra are normalized to compare spectral features. Some of the materials show strong absorption peaks, however, this does not affect the Raman signals.

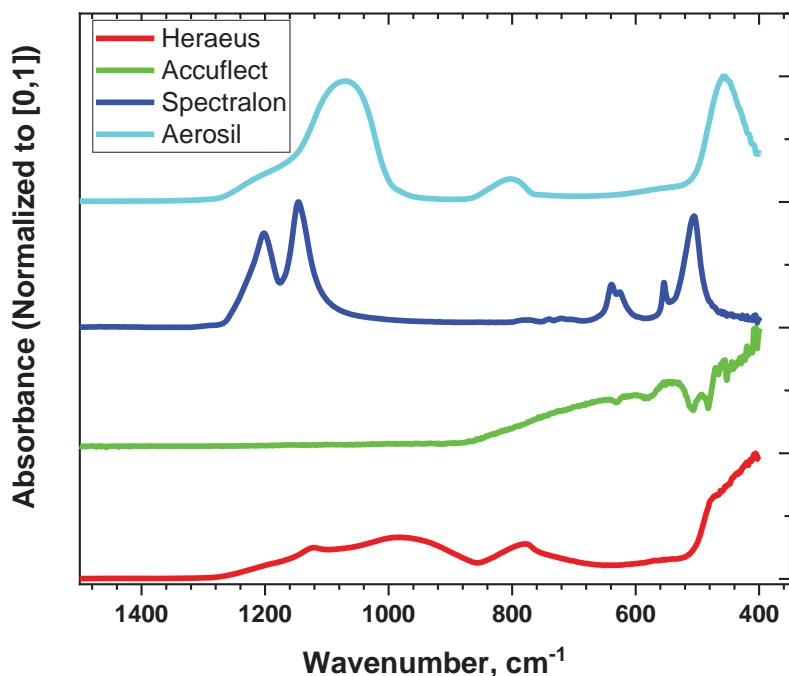


Figure 21. FTIR comparison of the various cavity materials.

Because Raman intensity scales with concentration, it is important to note that the material with the highest concentration inside an integrating cavity is the cavity material itself. As such, the material used to construct the cavity will likely cause the strongest Raman signal and will need to be subtracted from any sample signal. For characterization purposes, Figure 22 shows the Raman spectra of four different materials. The Spectralon and Accuratus materials show strong and distinct Raman peaks. Such strong signals may be problematic if they overlap with dye Raman bands and will need to be addressed when subtracting backgrounds. The other two materials, Heraeus and Aerosil, show no appreciable and distinct Raman bands. The high reflectivity and lack of vibrational structure should make these materials ideal for use in integrating cavities.

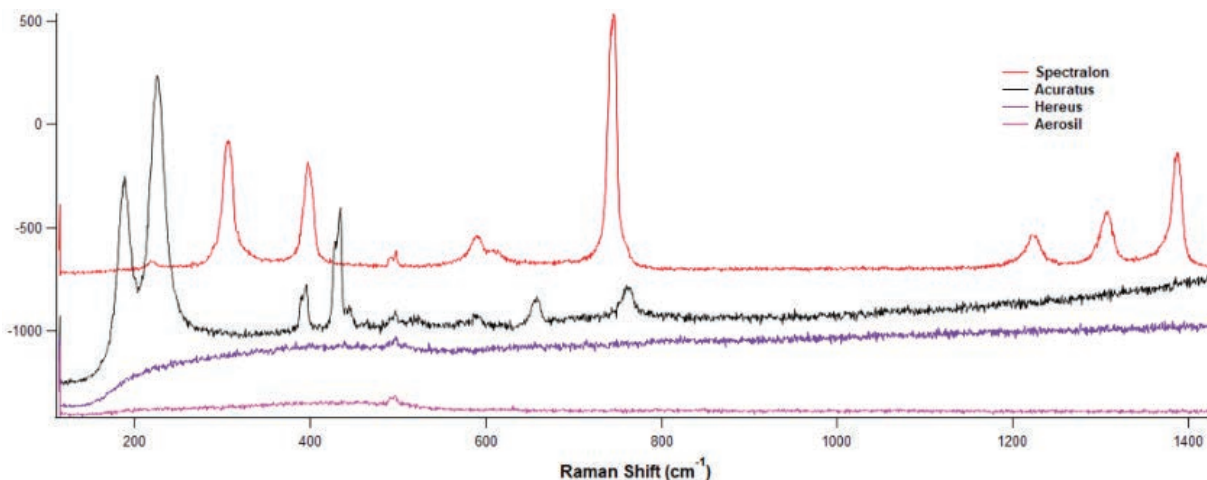
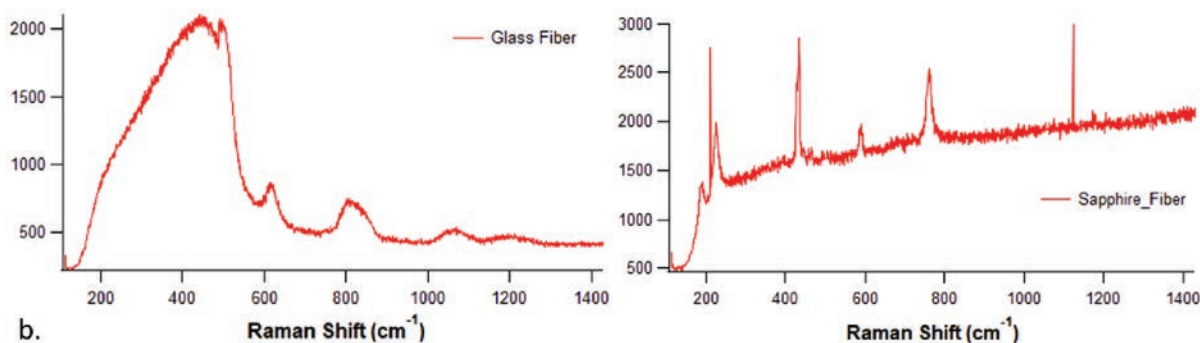


Figure 22. Raman spectra of various integrating cavity materials collected under 532 nm irradiation. The spectra are scaled and offset to show differences.

Comparison of Figure 19 and Figure 22 indicates that using the sintered Aerosil material in combination with a UV wavelength, would be the best combination. Using UV wavelength has the additional advantage

that Raman scattering is proportional to λ^{-4} (i.e., changing from 532 nm to 266 nm increases the scattering efficiency by a factor of 16). Furthermore, since fluorescence is typically emitted at wavelengths above 300 nm, choosing a lower wavelength such as 266 nm (4th harmonic of Nd:YAG laser) offers sufficient spectral room for Stokes Raman spectroscopy without interference from fluorescence.

Besides the cavity material itself, we also need to consider the optical fibers used to guide laser light into the cavity and collect the scattered light. Figure 23 shows Raman spectra obtained when using an optical fiber made of fused quartz (top) and sapphire (bottom) under 532 nm irradiation. Concerns for using a glass fiber include that the background will increase with laser power and fiber length and that correction will be difficult due to overlapping scattering and fluorescence being convoluted. Concerns for the sapphire fiber include higher losses because the fibers have no cladding and higher cost and fragility. As an alternative, we may not need a fiber if we can collimate and collect light directly from a port on the side of the integrating cavity.



b. Figure 23. Raman spectra obtained when using an optical fiber made of fused quartz (left) and sapphire (right) under 532 nm irradiation.

We continued the characterization and evaluation of cavity materials. Our previous results indicated that our custom-processed Aerosil material performs better than any other commercially available material. As such, our current work focuses on the Aerosil material prepared under various conditions.

The integrating cavity is prepared from Aerosil OX 50 (Evonik). To aid with pressing and sintering, a binder (Poly(vinyl butyral-co-vinyl alcohol-co-vinyl acetate), is incorporated at 5 wt% with respect to the Aerosil. The binder is first dissolved into acetone prior to the addition of the Aerosil in a 20% solution.

The solution is mixed for several hours and then poured in shallow pans to allow the acetone to evaporate, see Figure 1. The Aerosil combined with binder is dried, crushed, and ground and course sieved prior to loading into a 4" ID x 2" H quartz mold, see Figure 24



Figure 24. Crushing and grinding Aerosil OX 50 following incorporation of 5% binder.

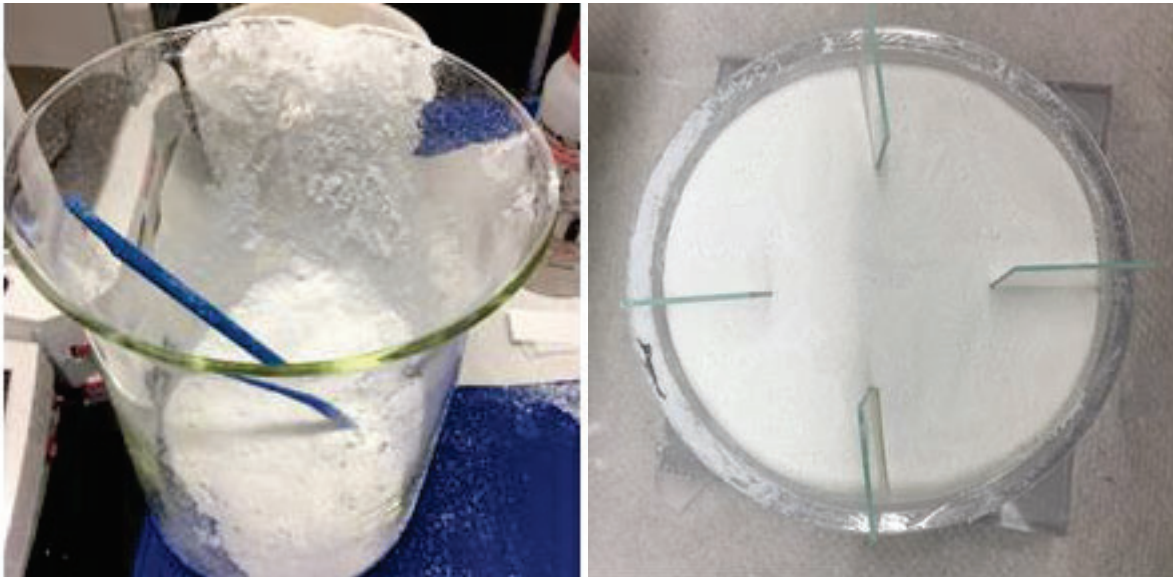


Figure 25. Sieved Aerosil OX 50+5wt% added to quartz mold with Plexiglas bottom.

Prior to adding the powder to the mold, a 1" H x 2" DIA quartz puck is centered with four quartz slides. The Aerosil + 5 wt% binder is pressed around the quartz puck to form one half of the cavity, see Figure 25. Approximately 135 g of the powder mixture is poured over the centered puck and pressed with approximately 5,000 lbs. force and held for 15 min, see Figure 26.

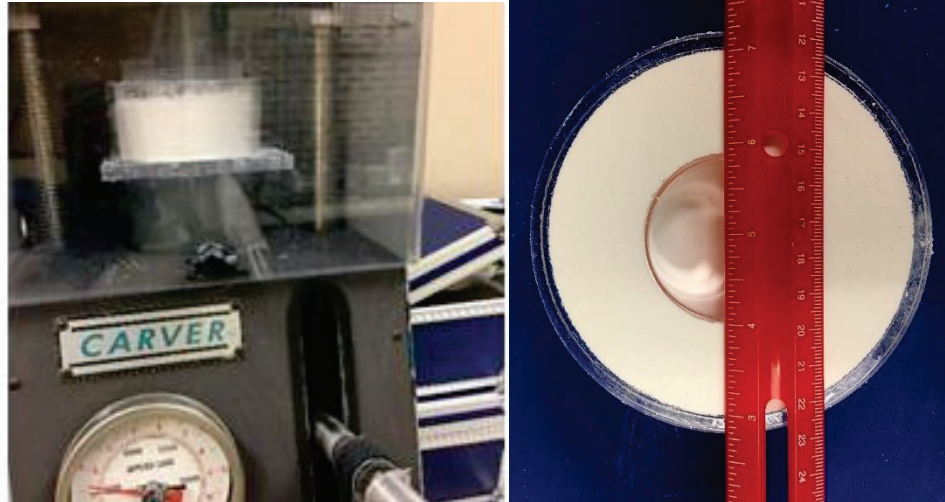


Figure 26. Cavity pressed at 5,000 lbs. for 15 minutes.

Spread out over 12.56 in², this is equivalent to approximately 238 PSI. A 4-in² Plexiglas plate is positioned at the bottom and several 4-in diameter quartz discs are positioned at the top of the cylindrical mold along with an additional plastic plate to protect the quartz from direct metal contact prior to pressing. The Plexiglas is then removed, and the cylinder inverted, see Figure 27.

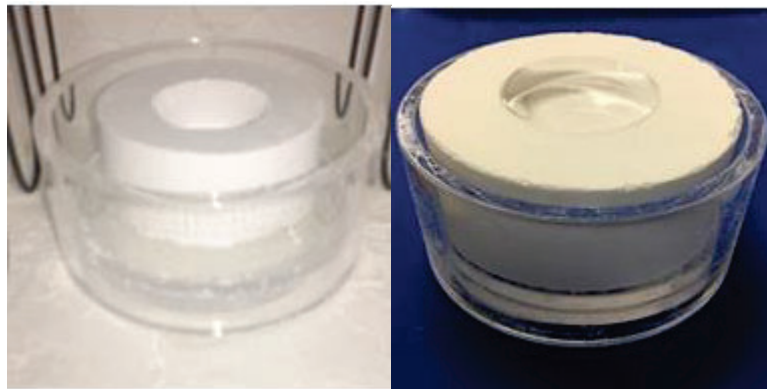


Figure 27. Cavity sintered at 1,050 °C for 6 hours (left) vs. 1 hour (right).

The cylinder with the quartz puck is sintered at 1,050 °C as a function of 1, 3, and 6 hours of soaking time. The quartz puck is left in the center during sintering to maintain consistent cavity size for each half produced, see Figure 28.

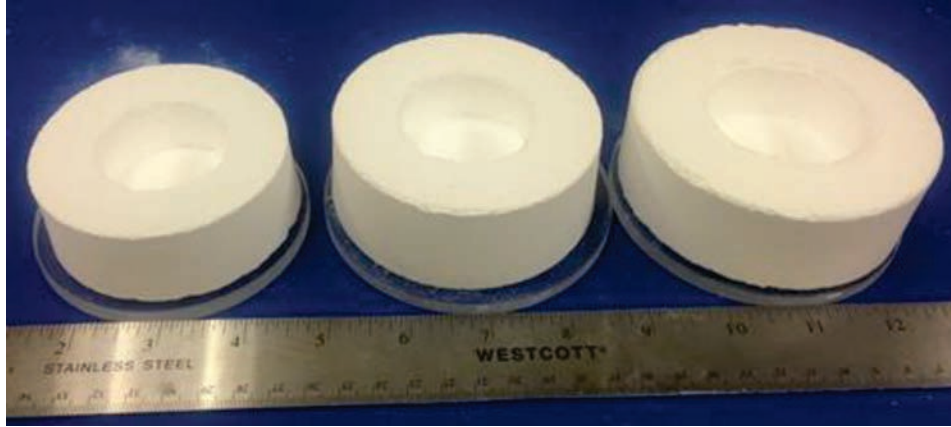


Figure 28. Comparison of cavities sintered at 1,050 °C as a function of soaking times of 6 hours (left), 3 hours (center), 1 hour (right).

The cavity sintered for six hours lost the most volume. Considering the extent of sintering observed, it is anticipated to have the lowest reflectivity. Conversely, the cavity with the least volume loss is expected to have the best reflectivity. An assembled cavity is shown in Figure 29.

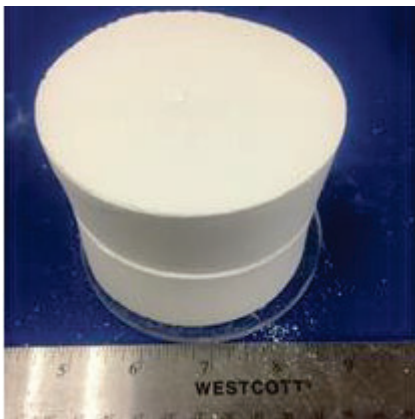


Figure 29. Assembled cavity.

For better comparison, we acquired a new calibrated reference standard for the Cary 5000 integrated sphere. Measurements revealed that the previously used Spectralon sample had somewhat degraded over time, in particular in the UV wavelength range.

Figure 30 shows the UV-Vis reflectance spectra of Aerosil-based samples for various processing conditions. The data is compared to that of a new Spectralon reference which has been normalized to 100%. Several important findings were made:

1. The main advantage of Aerosil materials occurs in the UV wavelength range, below 400 nm.
2. The thickness of the Aerosil samples is an important criterium for the reflectivity. The 5 g (10 mm thick) performs significantly better than the 2 g (4 mm thick) sample.
3. Reflectivity is dependent on which side of the sample is measured.
4. Aerosil and Aerosil/binder samples that were not heat-treated performed well under some conditions. However, these samples tend to crumble when handled.

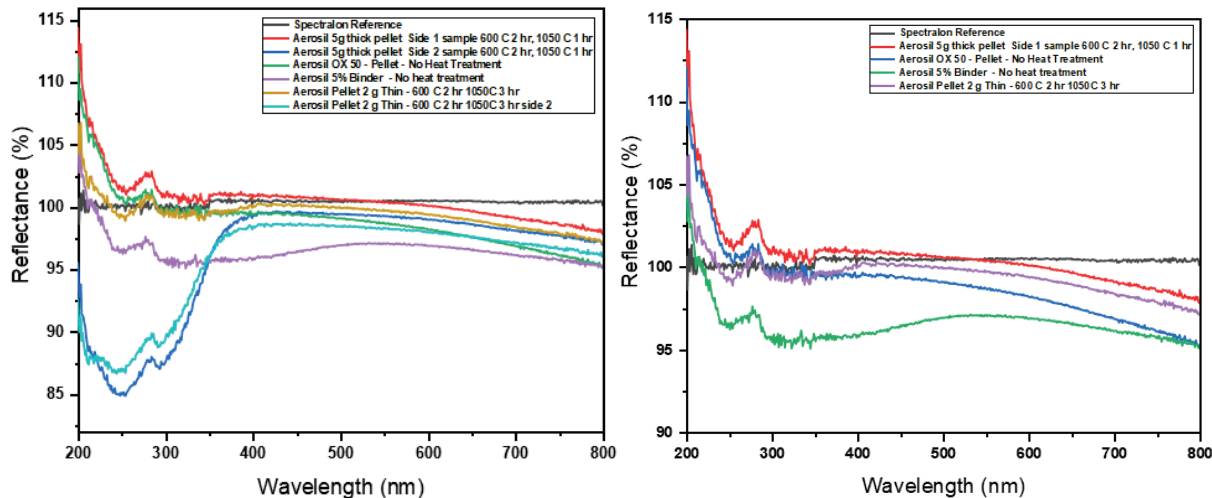


Figure 30. Reflectivity of various Aerosil samples relative to a new calibrated Spectralon standard whose reflectivity was normalized to 100%,

The fact that Aerosil-based samples have a significantly better reflectivity in the UV wavelength range indicates that our Raman measurements will have to be performed in the UV so as to take advantage of any cavity enhancement process. Compared to other wavelengths, the use of UV has several advantages. Raman scattering is proportional to the fourth power of the inverse of the wavelength (i.e., the Raman scattering cross section at 300 nm is 16 times higher than the one at 600 nm). However, when wavelengths of about 300 nm or longer are used for Raman spectroscopy, autofluorescence tends to cause significant noise which can overwhelm any Raman signals. Laser wavelengths around 250 nm, however, avoid the generation of autofluorescence. As such, we are currently evaluating the potential of using 248.6 nm (NeCu hollow-cathode metal-ion laser in combination with a plasma-line filter) and 266 nm (fourth harmonic of a Nd:YAG laser).

The strong dependence of reflectivity on the thickness of the Aerosil samples highlights the strong scattering effect of this material. Photons are multiply scattered throughout the material, and some are backscattered and lost. As such, the dependence on sample thickness needs to be carefully evaluated.

The strong dependence of the reflectivity on the side of the sample was a surprised finding and requires further evaluation. Possible explanations include a temperature gradient during the heat treatment (the bottom side of the sample rests on a support which may limit the temperature. Alternatively, the contact with the support may affect the surface morphology during the heat treatment.

Finally, while the non-heat-treated samples showed good reflectivity, they are not mechanically stable, and our results show that the treatment conditions can be selected so as to have good mechanical stability combined with good reflectivity.

We continued to encounter challenges (e.g., mechanical stability vs. UV reflectivity) during the cavity preparation process and had to continue to refine the process. Figure 31 shows several images related to the preparation and processing of the Aerosil cavity material.

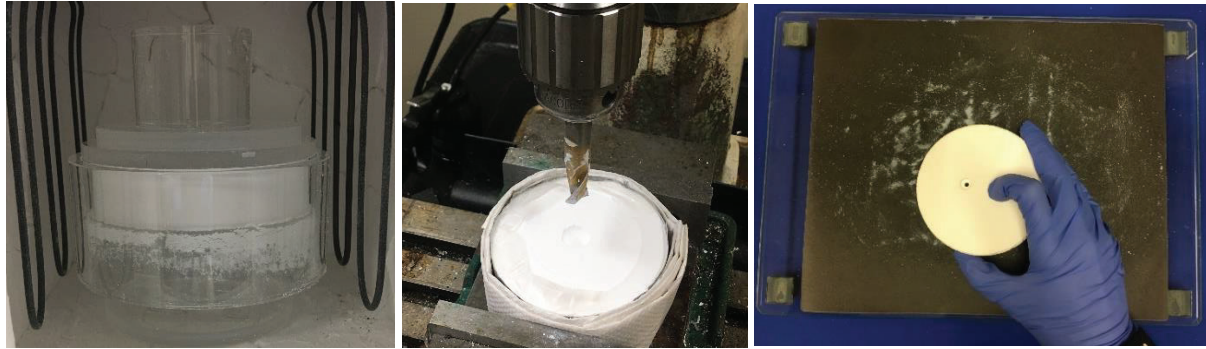


Figure 31. Preparation and processing of the Aerosil cavity material. Aerosil sintered in quartz mold with weighted top plates (left). Cavity and through ports prepared with various end mills (center), and flat mating faces prepared by grinding and polishing with SiC paper.

One of the unexpected findings during our investigation was that the reflectivity in the UV wavelength region depends on whether the material was in contact with a quartz substrate, see Figure 32.

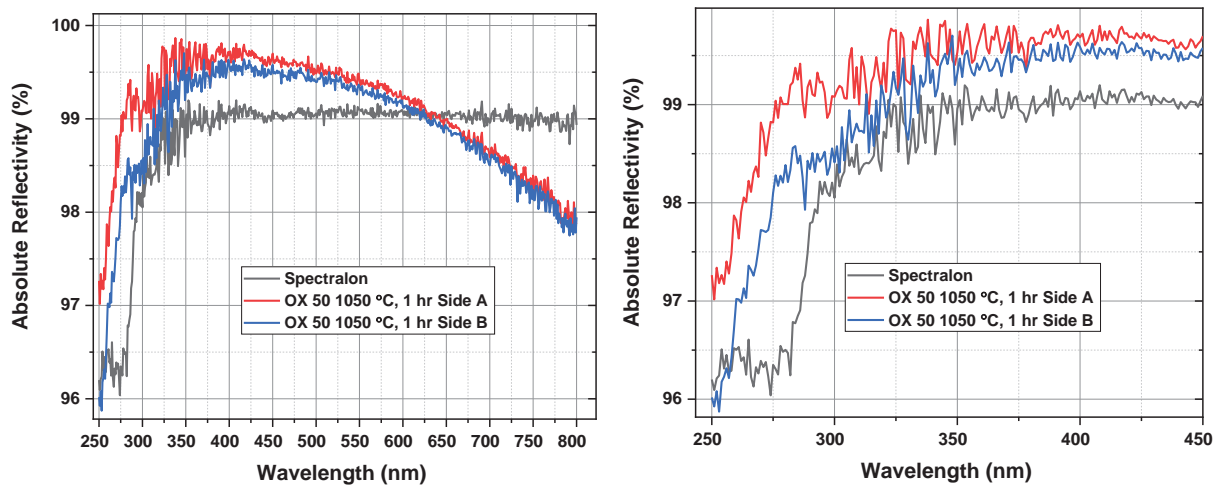


Figure 32. Reflectivity of Spectralon and sintered Aerosil samples (left) and zoomed-in view (right). The side of the Aerosil sample that was in contact with a quartz substrate shows higher reflectivities in the UV region.

Our initial hypothesis was that this difference in reflectivity was due to differences in the microstructure of the Aerosil material. During this reporting period, we tested this hypothesis by performing optical and electron microscopy imaging experiments. Optical microscopy did not show any apparent differences between the two sides, indicating that any differences would have to occur at much smaller length scales. Figure 33 shows SEM images of as-received Aerosil and Aerosil mixed with a binder. It is apparent that the binder mixes well with the Aerosil, allowing us to handle the material and form cavity structures.

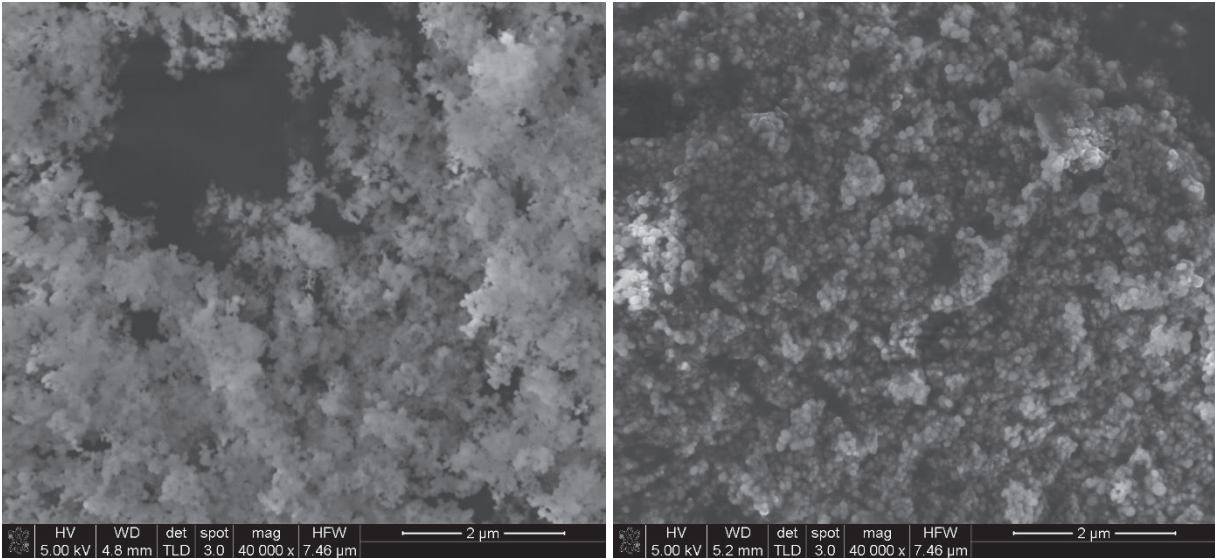


Figure 33. SEM images of as-received Aerosil powder (left) and Aerosil powder mixed with binder (right).

After a series of Design-of-Experiment (DOE) runs to determine the best sintering parameters, we settled on the heating profile shown in Figure 34. The hold at 600 °C is used to burn out the binder from the Aerosil material. The hold at 1,050 °C ensures sintering of the Aerosil particles.

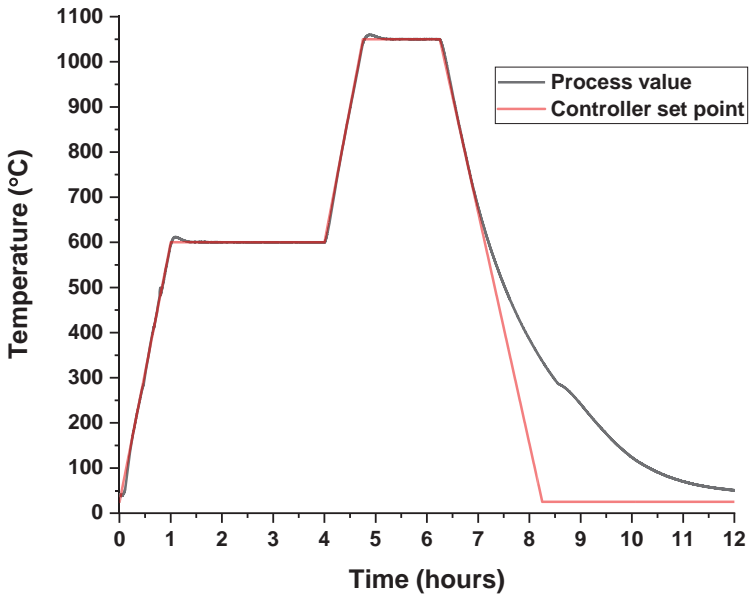


Figure 34. Heating profile used for the preparation of Aerosil cavities.

Figure 35 shows SEM images of sintered Aerosil material. The image on the left is for Aerosil material that was in contact with a quartz substrate during the sintering process, while the image on the right is for Aerosil material from the inside of a cavity that was exposed to air in the furnace. Except for some discolorations, there are no apparent differences in the microstructure, indicating that our initial hypothesis was not correct.

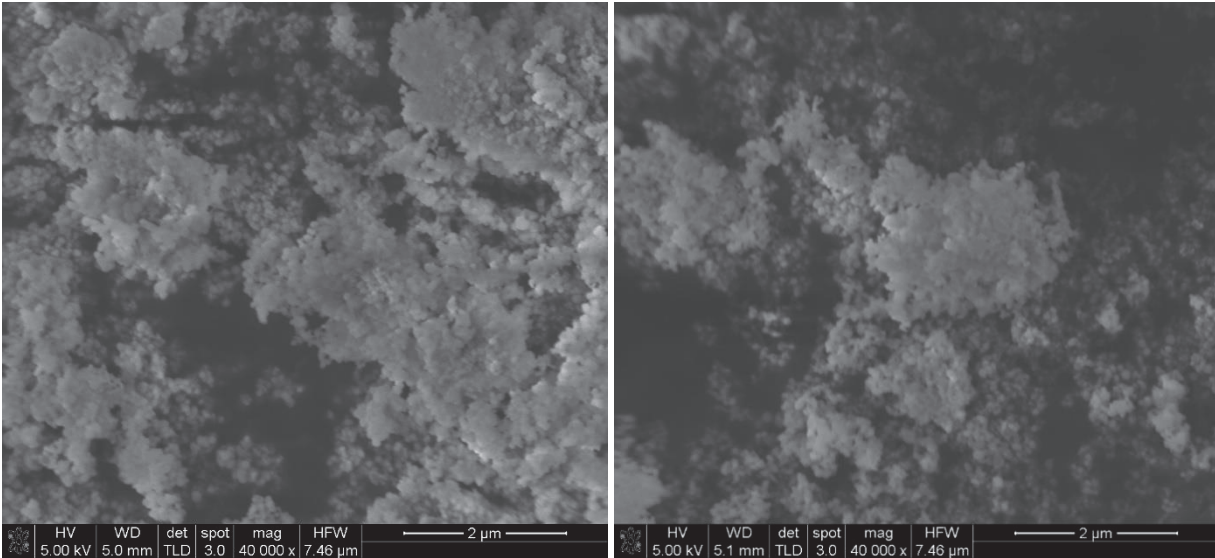


Figure 35. SEM images of the two sintered Aerosil sides, in contact with quartz (left) and exposed to air in furnace (right).

The furnace we use for sintering is relatively small, with our cavities filling up almost all the insides. When we tried using a larger furnace, we noticed that at the binder burnout temperature, the binder combusted. This combustion is not observed in the smaller furnace. This difference indicates that there is relatively little oxygen present in the smaller furnace, which leads us to hypothesize that the observed discoloration and differences in reflectivities, may be due to a reducing effect (i.e., there may be small differences in the oxidation state of the Si for the two sides. Proving such a hypothesis is challenging and requires special equipment such as XPS which we currently do not have. As such, we are focusing on using processing conditions that will optimize the reflectivity properties of the cavity and leave a more detailed material characterization for later.

Figure 36 and Figure 37 show images of cavities prepared in September and December of 2020. The cavity in Figure 36 was prepared in two cylindrical halves and molded with a quartz cylinder. Subsequent removal of the quartz cylinder was difficult due to Aerosil contracting during the sintering process and caused some cracking and minor damage to the cavity as well as disruption to the internal surfaces of the cavity. The cavity prepared in Figure 37 is composed of three parts: top and bottom disks and a center hollowed cylinder. This approach produced a cavity free of cracks with a flatter fit between mating surfaces to minimize light from escaping. Each mating surface was polished for a low tolerance. Multiple hollow cylinders may be stacked to increase the total surface area of the cavity.

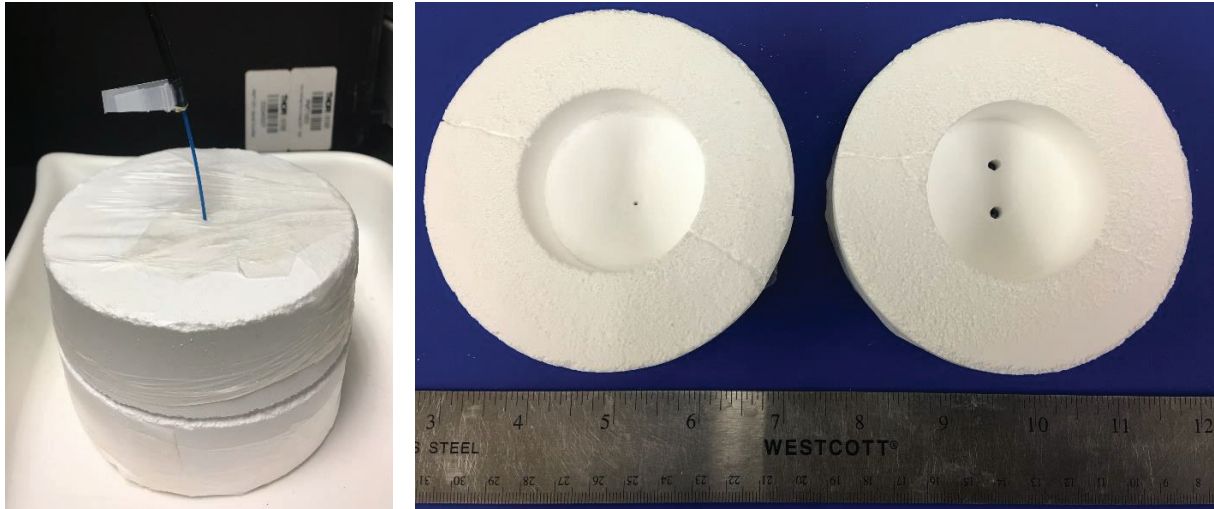


Figure 36. Cavity prepared in September of 2020.

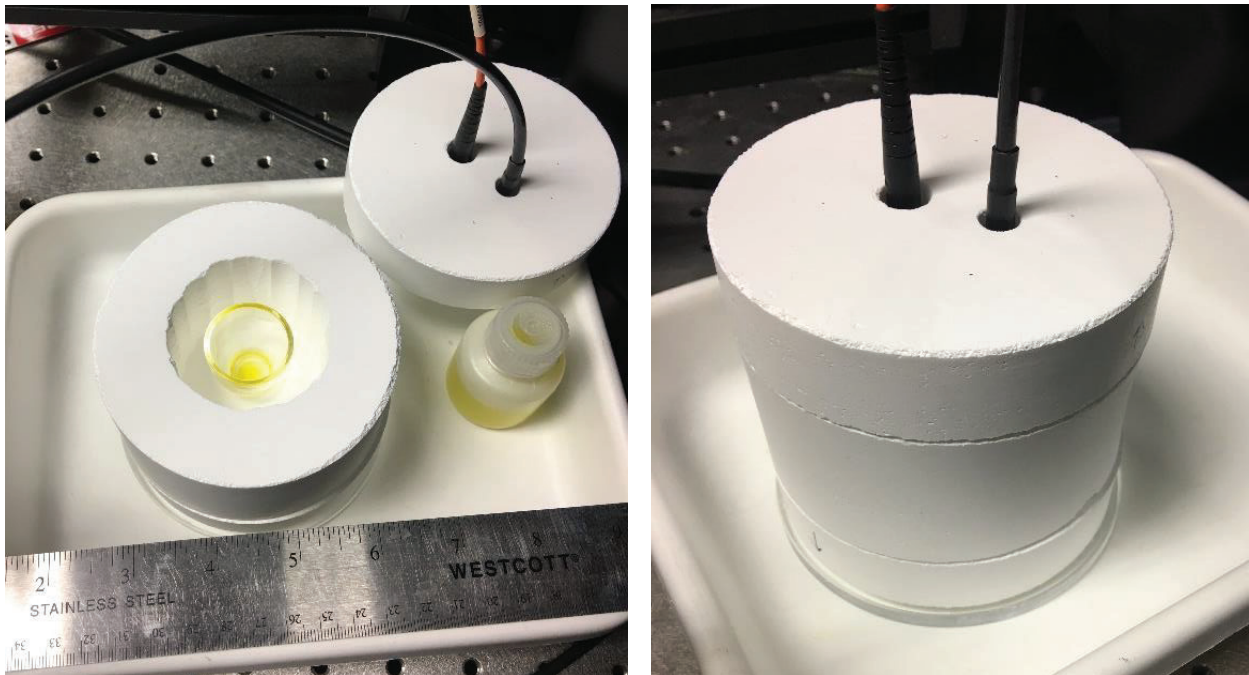


Figure 37. Cavity prepared in December of 2020.

Reflectivity of Aerosil

Using a calibrated Spectralon reflecting puck we performed absolute reflectivity measurements of our aerosol material using a UV/VIS/NIR Cary 5000 Spectrophotometer with the resulting spectrum shown in Figure 38 (note the Spectralon's calibrated spectrum is included for reference). We find from Figure 38 that Aerosil has better reflectance than Spectralon from 250 nm to approximately 610 nm, with aerosol having reflectivities >99% from 280 nm to 610 nm.

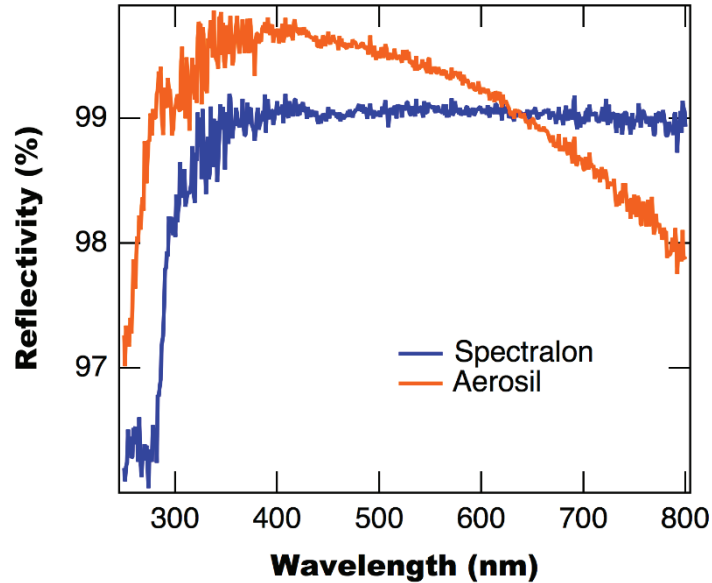


Figure 38. Absolute reflectivity of Spectralon and Aerosil measured using a UV/VIS Spectrophotometer.

Variability and processing

Figure 39 shows multiple raw reflectivity measurements of the same sample, indicating excellent reproducibility of our measurements. After polishing the sample, the reflectivity increased slightly for wavelengths below 230 nm. At this time, it is not clear what effect is responsible for this increase. For comparison, we also show the reflectivity of the commercial Spectralon sample. It is apparent that the Aerosil material has higher reflectivities in the UV wavelength range.

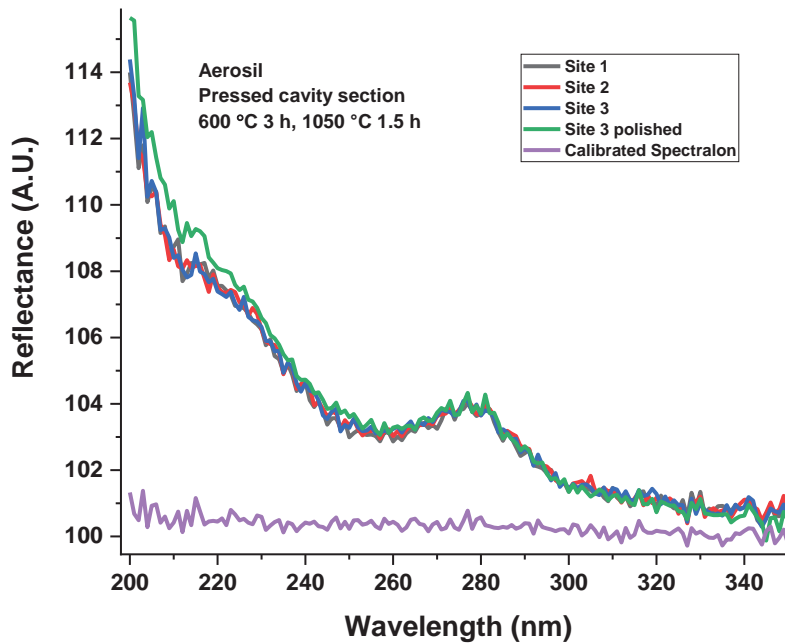


Figure 39. Multiple measurements of the reflectivity show the good level of reproducibility of our data. After polishing, the reflectivity below about 230 nm increased somewhat. The reflectivity of the Spectralon sample is shown for comparison.

The main challenge for us is to select the best laser wavelength to use with our cavities. For that decision, we need to consider the following:

1. The availability of commercially available laser wavelengths.
2. The spectral dependence of the absolute reflectivities of the Aerosil material.
3. The fact that Raman scattering is proportional to the fourth power of the inverse of the wavelength (i.e., the Raman scattering cross section at 300 nm is 16 times higher than the one at 600 nm).
4. The fact that UV wavelengths can result in significant background fluorescence which can overwhelm any Raman signals.

Given these requirements, we are currently focusing on using a frequency-tripled Nd:YAG for the characterization of our cavities.

Calculated Enhancement

To model the intensity enhancement of an integrating cavity with reflectivity r , we can use a simple model that assumes a two-mirror cavity with each mirror having internal reflectivity r , but perfect transmission into the cavity. Into this cavity we place a sample that either emits fluorescence or Raman scatters. For simplicity we assume that the pump light is not depleted by the sample and therefore the cavity walls are the only source of energy loss. When pump light is injected into the cavity it will “bounce” back and forth with each iteration producing emitted light from the sample. This emitted light then also cycles within the cavity with only a fraction of the light escaping each time it strikes a mirror. Summing up the emitted light escaping from one mirror and dividing that intensity by the cavity-less situation, we find that the intensity enhancement is given by

$$\begin{aligned} \eta &= (1 - r) \left(r + \sum_{n=0}^{\infty} \sum_{k=n}^{\infty} r^{2k} + 2 \sum_{n=1}^{\infty} \sum_{k=n}^{\infty} r^{2k+1} \right) \\ &= (1 - r) \left(\frac{1}{(r^2 - 1)^2} + \frac{2r^3}{(r^2 - 1)^2} + r \right) \end{aligned} \quad (1)$$

where we have simplified the summation to give a closed form solution.

We plot Equation 1 as a function of reflectivity in Figure 40 with the enhancement found to be small for reflectivities under 0.99 but rapidly increasing as the reflectivity passes 0.995. Based on this observation it is clear that we want a cavity with reflectivities $> 99.5\%$ if we want to maximize the usefulness or cavity enhancement.

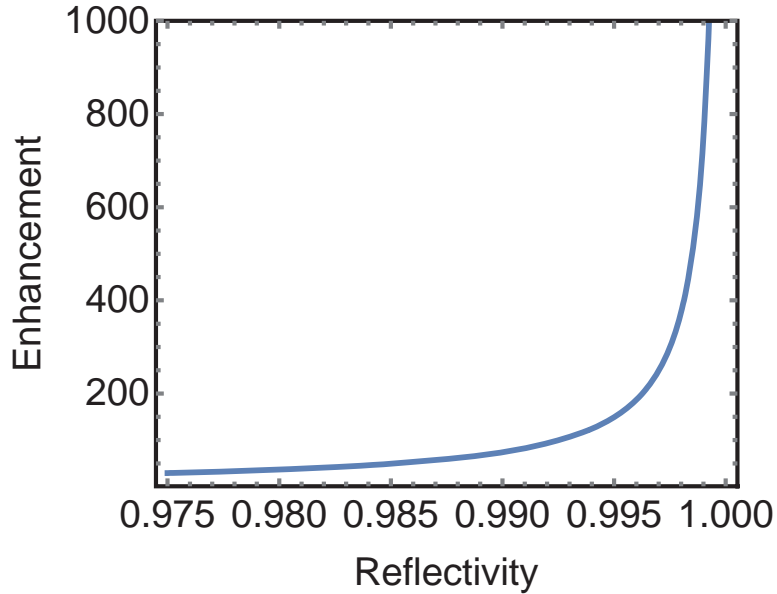


Figure 40. Calculated enhancement as a function of reflectivity.

Aerosil Cavities

September 2020 Cavity

Figure 41 shows the ringdown curves for the cavity prepared in September of 2020. By fitting the curve to an exponential decay, we determine the reflectivity of this cavity to be about 98.7%.

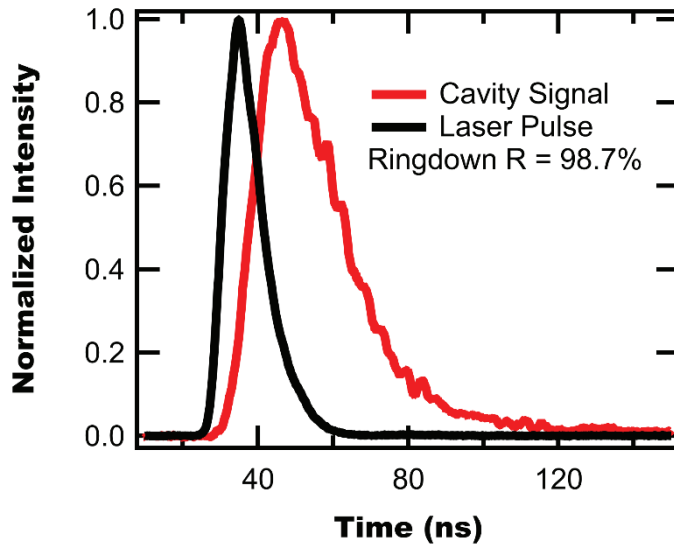


Figure 41. Example pulse ringdown curves for the Sep 2020 cavity. The calculated reflectivity is 98.7%.

December 2020 Cavity

After the new Aerosil cavity (with $\bar{d} = 2.147$ cm) was prepared we performed ringdown measurements to determine the cavity’s reflectivity. During these measurements we discovered significant variations in reflectivity, whose source is currently unknown. Example ringdown traces taken on four separate days are

shown in Figure 42, demonstrating variations in the resulting pulses. Note that after the Dec 17/18 traces were measured, we placed the cavity in a vacuum oven after which we measured the traces again on Dec 22/23. The measured ringdown times and calculated reflectivities from the different days are tabulated in Table 25. From these values we find that the two ringdowns on Dec 22 and 23 are within uncertainty of each other, while the Dec 17 and 18 ringdowns are significantly different.

Based on these observations we speculated that the variations may either be due to environmental factors or due to variations in how the different pieces of the cavity are put together. Addressing the environmental factors is challenging as our experimental space currently does not have strict controls. However, it is simple for us to test the arrangement of cavity pieces by disassembling and reassembling the cavity. Therefore, we perform five different assembly runs and measure their ringdown times and calculated reflectivities, which are tabulated in Table 26.

From Table 26 we find that the ringdown times and reflectivities vary outside of the fit uncertainty and fit in a range with a width of approximately 0.015%. This is smaller than the width observed for the reflectivity measured on different days which spans a range of $\approx 0.06\%$. This suggests that the day-to-day variation involves more than just assembly variations. Further work is required to understand these variations and better quantify them.

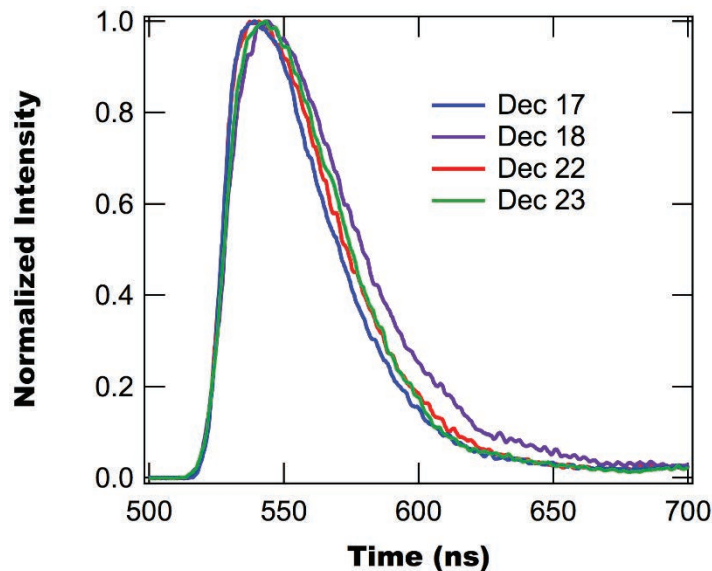


Figure 42. Pulse measurements on different days in December 2020. Between the Dec 17/18 measurements and the 22nd and 23rd measurements the cavity was stored in a heated vacuum oven.

Table 25. Measured ringdown time and calculated reflectivities measured on different days.

	Ringdown Time (ns)	Reflectivity (%)
Dec 17	26.71 ± 0.10	99.7322 ± 0.0030
Dec 18	34.17 ± 0.13	99.7906 ± 0.0022
Dec 22	28.58 ± 0.11	99.7496 ± 0.0027
Dec 23	28.06 ± 0.16	99.7451 ± 0.0029

Table 26. Ringdown repeatability measurements.

	Ringdown Time (ns)	Reflectivity (%)
1	28.58 ± 0.11	99.7496 ± 0.0027
2	28.65 ± 0.14	99.7503 ± 0.0028
3	28.29 ± 0.12	99.7472 ± 0.0027
4	27.70 ± 0.12	99.7418 ± 0.0028
5	29.16 ± 0.13	99.7547 ± 0.0027
Average	28.48 ± 0.24	99.7489 ± 0.0033

Photoluminescence Measurements

As a first test of cavity enhancement we begin with photoluminescence measurements, as photoluminescence is several orders of magnitude brighter than Raman scattering. For these initial tests we used the cavity made in September, which has a reflectivity of 98.7%. We begin by first characterizing the emission response of the empty cavity using 355 nm excitation, which is shown in Figure 43. From Figure 43 we observe that for the empty cavity there is a broad PL emission peaking near 430 nm along with multiple sharp peaks. Initially these were hypothesized to be cosmic ray contamination, but multiple measurements revealed the peaks to be reproducible. While the source of these emission peaks is unknown, their intensity is relatively small and will most likely be negligible compared to the signal.

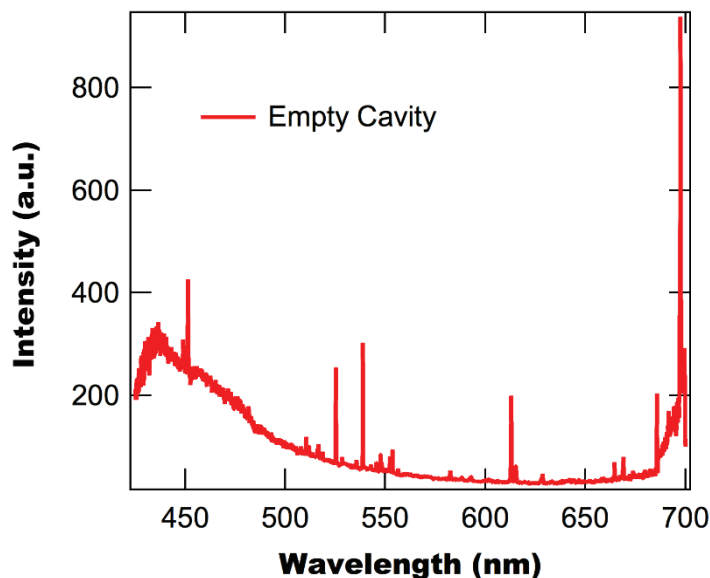


Figure 43. PL signal from empty cavity.

Having measured the empty cavity we next turn to testing a dye-doped polymer sample, which consists of Disperse Orange 11 doped into polyurethane. We measure its PL using a traditional PL microscope, the full cavity, and the cavity without a base (i.e., we effectively cancel multiple reflections) with the resulting spectra shown in Figure 44. From Figure 44 we find that the full cavity PL spectra is approximately 61.7x as large as the half-cavity, which demonstrates the cavity enhancement effect. This enhancement is roughly equal to our predicted enhancement of 57x for a reflectivity of 98.7%.

While Figure 44 shows cavity enhancement between having a full and half cavity, it also shows that the PL microscope produced a signal almost 10x greater. This can be attributed to significantly more efficient coupling of the emitted PL in the microscope as the current cavity design only uses a fiber to collect light.

In order to capitalize on the cavity enhancement a new coupling design is required to properly collect light out of the cavity.

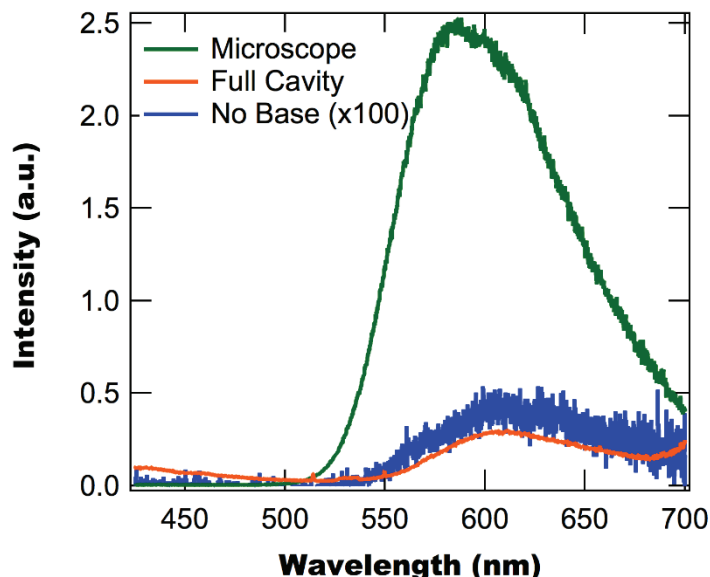


Figure 44. PL Intensity spectra measured in three different scenarios.

We prepared various cavity components using the previously established processing conditions. This general processing method was established to maximize the reflectivity of the inside surfaces of the cavity.

Since the reflectivity of the cavity material, Aerosil OX50, depends on its microstructure, and the microstructure depends on the thermal processing conditions, we further investigated the impact of the various sintering conditions, including time, temperature, and atmosphere. We used simultaneous thermal analysis (STA = thermogravimetry TG with simultaneous differential scanning calorimetry DSC) to study the cavity material under non-isothermal (dynamic) conditions. The Aerosil OX 50 consists of synthetic amorphous hydrophilic fumed silica, lacking a crystalline structure. To avoid the formation of crystalline cristobalite at 1300 °C we heat treated the material only to 1050 °C, as described previously. Thermal analysis was performed in dry “zero air” and in nitrogen.

This analysis is preliminary and constitutes an ongoing complementary study to the optical spectroscopy (Raman and fluorescence) measurements. These measurements are expected to provide additional information for understanding the cavity material and for improving the reflectivity and optical performance—the better the Aerosil is understood per the processing parameters, the better the rendering of a highly reflective cavity material.

Under nitrogen flow, the DSC curve of Aerosil OX 50 (Figure 45), shows a first exothermic peak at 362 °C, corresponding to binder burnout. The TG/DTG curves show the binder decomposition to occur between 376.5 °C and 477.1 °C with a mass loss of 2.77%. The DSC data show a second exothermic peak at 891 °C. This peak may be associated with the reduction in surface energy by sintering in an inert atmosphere, crystallization, or the consolidation of the material.

Under air flow, the DSC curve (Figure 46), shows a first exothermic peak at 341 °C, corresponding to binder burnout. The TG/DTG curves show the burnout to occur between 379.5 °C and 600.5 °C, with a mass loss of 3.32%. The somewhat higher mass loss in dry air is most likely due to the combustion/burning of the binder and the formation of products such as CO and CO₂. Unlike for the nitrogen flow, we do not

observe a second exothermic peak in the DSC data. The absence of this peak indicates that heating in zero air may interfere with the crystallization process.

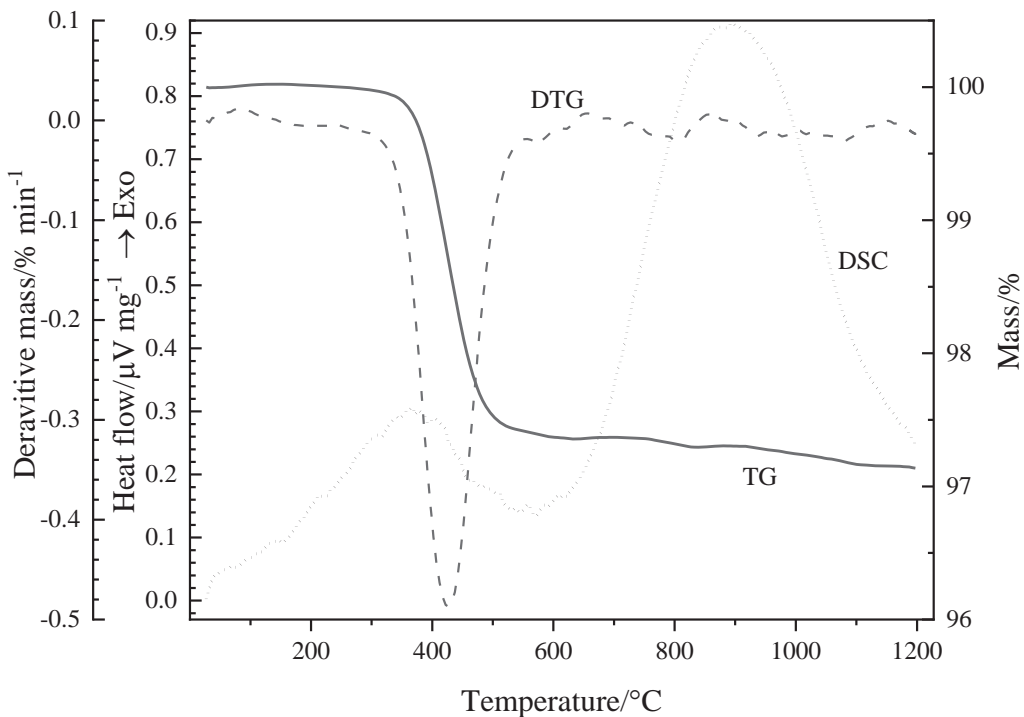


Figure 45. DSC and TG/DTG curves of Aerosil OX 50 + binder in nitrogen atmosphere (40 mL min⁻¹) and heating rate 20 °C min⁻¹.

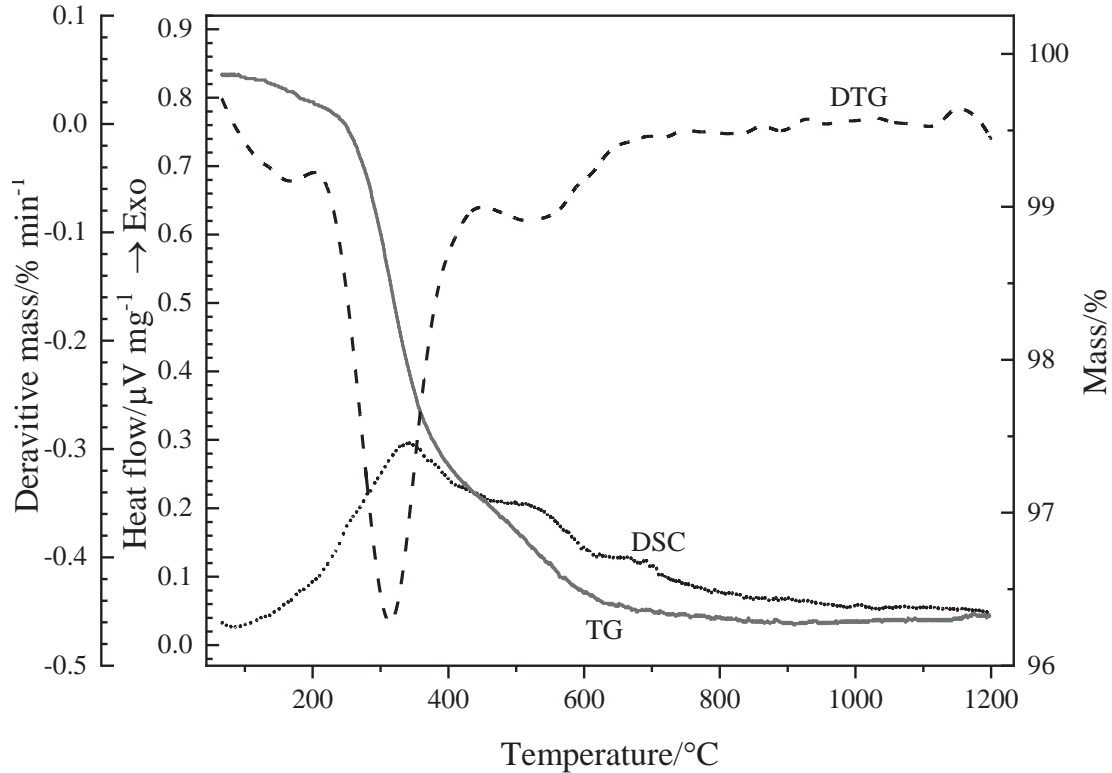


Figure 46. DSC and TG/DTG curves of Aerosil OX 50 + binder in zero air atmosphere (40 mL min⁻¹) and a heating rate 20 °C min⁻¹.

Cavity improvements

Several activities were completed to improve cavity performance. The existing cavity components were heat treated below the sintering temperature (600 °C, 1 hour) to remove moisture contamination that may have accumulated in the material over time. The internal volume of the cavity was enlarged by adding an additional hollow-centered cylinder. The existing cavity hollow center was also enlarged.

To prepare the new cavity segment, a 350 g batch of Aerosil + binder was prepared for an additional cavity section, see Figure 47. Material preparation is the same as reported previously and includes the following processing steps after the binder is introduced and the slurry is dried.

Crush → grind → sieve → mold → sinter → machine → polish

Following the sintering process, the Aerosil loses approximately 4.8 wt% due to the amount of binder that is burned out during the heating, see Figure 48.

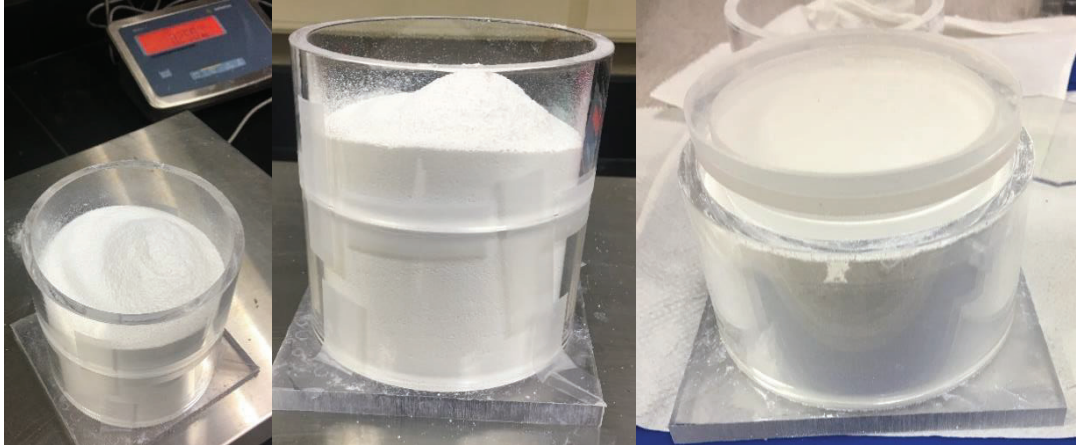


Figure 47. New Aerosil cylinder prepared to enlarge existing cavity volume.

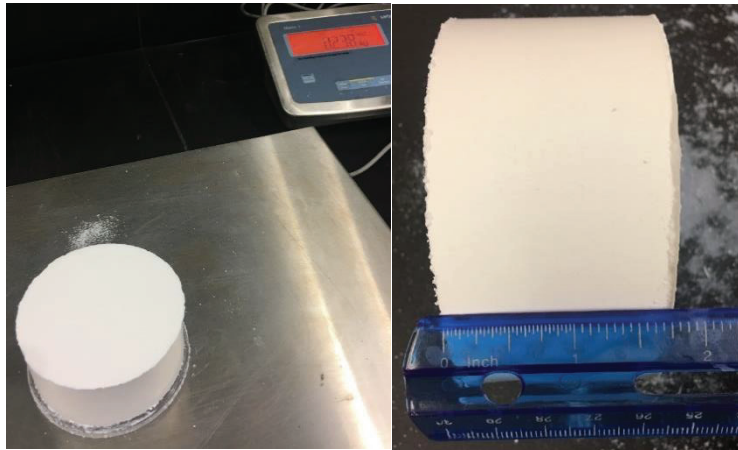


Figure 48. Post sintering weight of new cavity cylinder, 238 g for weight loss of 12 g or 4.8% weight loss.

Both the existing cavity sections were machined with an endmill to give each level a hollow center of 2" x 2" x 1.7", see Figure 49.

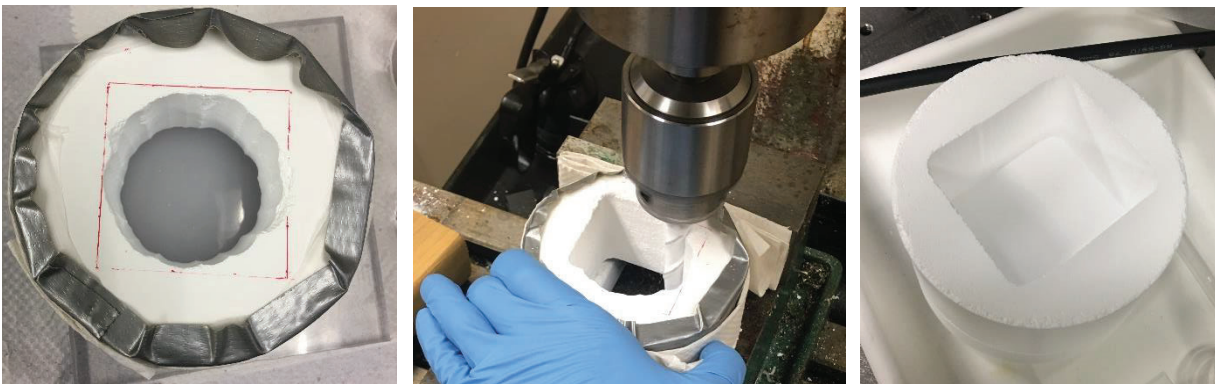


Figure 49. Cavity center modified to 2" x 2" square.

A new cavity top with FC/PC and bare fiber ports was prepared. The new Aerosil top was fabricated using the same method described above to make new ports for a kinematic lens assembly and to accommodate lens tube accessories to get the output coupler properly aligned in the cavity, improving coupling to the fiber. A New SM1 thread adapter with the kinematic mount was secured to the top of the cavity as shown in Figure 50. After the new cavity top was made, the other preexisting parts of the cavity including the bottom, and the two hollow segments were cleaned, and the bottom was resurfaced by polishing off the top layer exposed to the inside of the cavity. After surface cleaning by polishing and removing dust with canned air, all three parts were baked out to 600 °C for 1 hour in a furnace under ambient atmosphere according to the temperature profile shown in Figure 51. The purpose of the bakeout was to remove moisture and organics that can potentially accumulate, although this was done as a precaution and was not done reactively

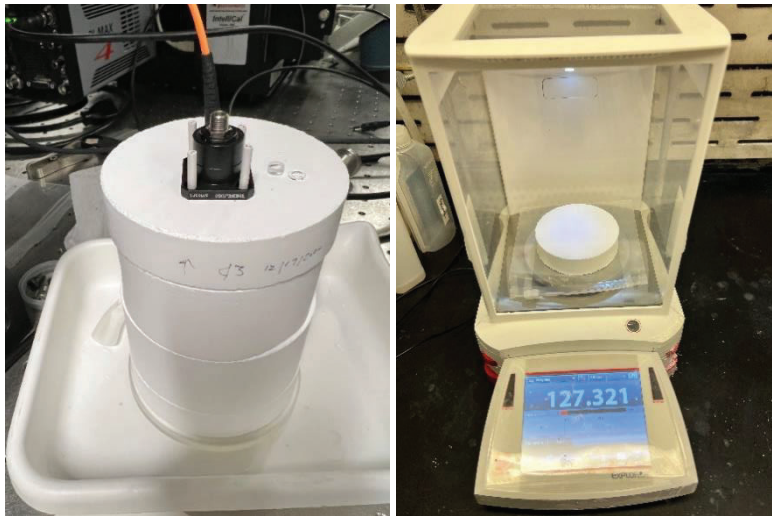


Figure 50. Cavity volume increased by the addition of a second hollow segment. A new top was fabricated to accommodate a kinematic mound to correct for beam offset.

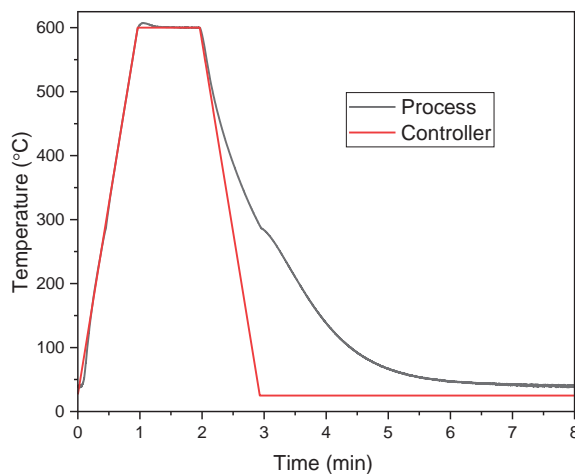


Figure 51. Cavity component bakeout.

Control samples

To eliminate the possibility of contamination being introduced during processing, a set of Aerosil pellets was prepared, see Figure 52. Contamination can lead to spurious fluorescence that could become problematic during ICERS analysis. One sample was prepared to determine if any oils from endmilling could have been introduced. A second sample was prepared by sanding with SiC sandpaper to determine if contact with the Aerosil components during processing would introduce any additional contaminants. Neither the endmilling or sanding created measurable contamination. The pellets were prepared similarly to the cavity material. Aerosil was combined with 5wt% binder (PVBVA) as reported previously, using acetone to dissolve the binder. Some of the sieved Aerosil powder with binder that was used to prepare the cavity section was pressed into 1/2" diameter, ~0.5 g (pre-sinter) pellets. Heat treatment and sintering were the same as reported previously for cavity preparation.

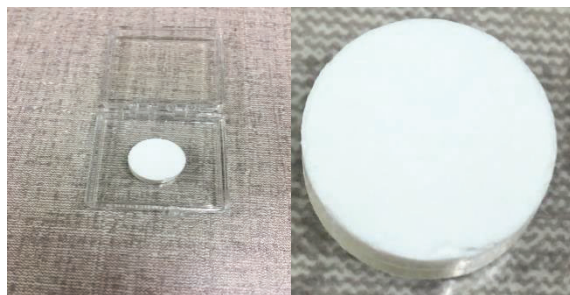


Figure 52. Pellets prepared for determination of spurious fluorescence.

OPTICAL MEASUREMENTS

Raman spectroscopy of dyes and dye fabrics without the use of an integrating cavity.

To benchmark Raman capabilities without the use of an integrating cavity, we collected spectra using the Raman setup depicted in Figure 53. In short, a 532 nm laser (Verdi 5, Coherent) is reflected off a beam-splitting cube and focused through a microscope objective (Mitutoyo, 20X 0.40NA) onto each sample. The Raman signal is then collected in a 180° backscattering geometry, passing through a spatial filter and notch filter (Kaiser, 532 nm) before being focused into a spectrograph (Princeton Instruments SP2500i).

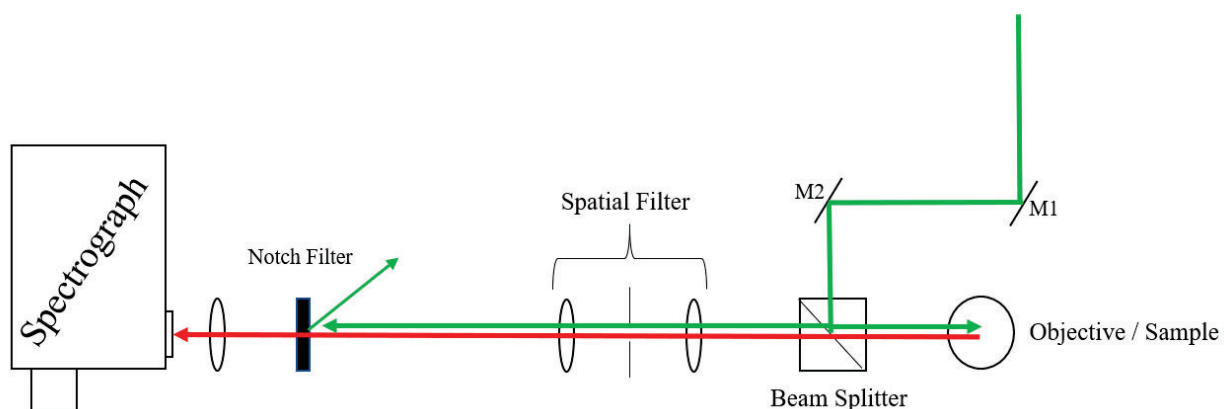


Figure 53. Schematic diagram of the Raman setup. Green lines represent the incident 532 nm laser light and Raleigh scattering while the red lines represent all other signals from the sample.

We collect all spectra at 1 mW total power at the sample point while choosing integration times based on optimal signal-to-noise (S/N) for each spectrum. We measured spectra from dye samples in both powder form and bound to fabrics under similar conditions. Currently, we have measured spectra of all 11 fabric samples and each associated dye using 532 nm irradiation.

Before the Raman spectra of each dye could be analyzed, we fitted a baseline to each sample to remove the large backgrounds caused by random scattered light and fluorescence. Figure 54a shows both the uncorrected and baseline corrected Stokes and antiStokes Raman spectra for undyed nylon fabric. As seen, a broad rising baseline appears beginning in the antiStokes region which reaches a maximum near 1500 cm^{-1} in the Stokes region of uncorrected spectrum. This feature is likely caused by fluorescence of the material and can be easily fit by hand as it has a predictable shape resembling that of an emission curve. As a note, fitting baselines to such spectra by hand is a common practice in situations such as this, however, future work will include a more objective procedure for fitting such as polynomial fits or spline interpolations. The baseline corrected spectrum of nylon is also shown in Figure 54a, clearly indicating the Raman peaks.

Figure 54b shows the uncorrected Stokes and antiStokes Raman spectra of both Telon Yellow FG01 (TY FG01) and Acid Yellow 049 (AY 049). For clarity, both the TY FG01 and AY 049 spectra consist of the same dye, however, the former is bound to a piece of Nylon fabric and the latter was sampled directly from pure dye powder. As observed, both spectra show a rising baseline extending the entire probed spectral region, with the amplitude of TY FG01 far exceed that of AY 049. The increased baseline of the dye when bound to Nylon can be attributed to both the additive signal of the dye and nylon fabric and to the decreased degrees of freedom (DOF) of the bound dye. Here, the more rigid structure of the bound dye compared to that of the powdered dye exhibits fewer DOF decreasing nonradiative channels and subsequently increasing emission.

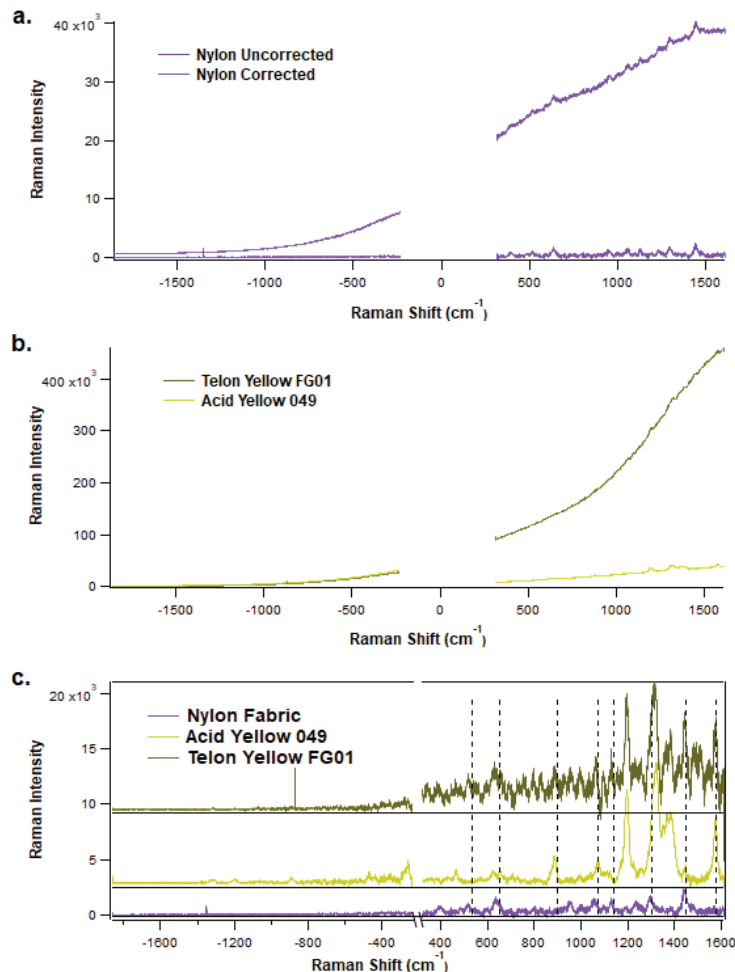


Figure 54. a) The Stokes and antiStokes Raman spectrum of nylon fabric both uncorrected and corrected. b) The uncorrected Stokes and antiStokes Raman spectra of Telon Yellow FG01 (olive) and Acid Yellow 049 (yellow). c) A comparison of the corrected Stokes and antiStokes Raman spectra of dye Acid Yellow 049, Telon Yellow FG01 and Nylon fabric under 532 nm irradiation. Dashed lines are added for comparison of common spectral features.

Figure 54c displays the corrected Stokes and antiStokes spectra of Nylon fabric, AY 049 and TY FG01. From the spectra, we find that both ‘dye’ Raman spectra are near identical with negligible contribution from the pure Nylon. As a consequence of the larger amplitude baseline, TY FG01 shows much lower S/N than pure AY 049.

Figure 55 shows baseline corrected and scaled data for three different acid dye samples. Panels 11a and 11b display the antiStokes and Stokes Raman spectra of the dyes in powder form, respectively. Panels 11c and 11d, display the same three dyes in identical spectral windows, however, each of the dyes is deposited on Nylon fabric. From these plots we can make several observations: 1) All dyes exhibit different Raman peaks which will make them distinguishable from one another even in mixed samples. 2) Depositing the dyes on Nylon fabric does not change the Raman spectrum significantly, making separation of Nylon fabric peaks from dye peaks possible. 3) Samples which are deposited on Nylon fabrics generally show much worse S/N than when sampled from pure powder. The enhanced baseline when deposited on Nylon decreases S/N such that many bands, especially in the antiStokes region, are indistinguishable.

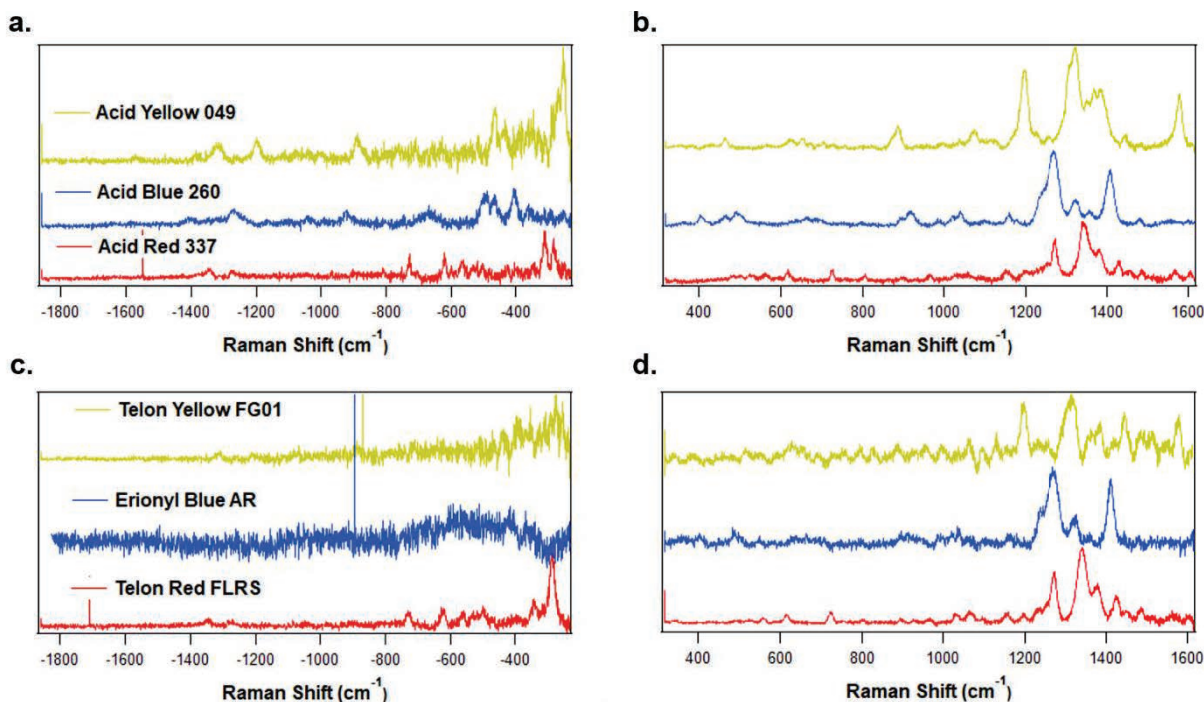


Figure 55. The baseline corrected Raman spectra of dyes Acid Yellow 049, Acid Blue 260 and Acid Red 337 sampled directly from powders in the antiStokes (a) and Stokes (b) spectral regions, respectively. The Raman spectra of the same dyes deposited on Nylon fabric are presented as Telon Yellow FG01, Eroiny Blue AR and Telon Red FLRS in the antiStokes (c) and Stokes (d) regions, respectively.

To assess the ability to distinguish minor components, samples of “Black” colored fabrics were created for testing with Raman spectroscopy. Figure 56 displays the corrected and overlaid spectra of Nylon fabric (purple), Nylon Black (black), Telon Red FLRS (red, lower spectrum) and Acid Red 337 (red, top spectrum). From this, we are only able to identify that the Acid Red 337 dye appears to be a major component showing near identical bands to Nylon Black and Telon Red FLRS with no apparent contribution from any other dye or the Nylon fabric itself.

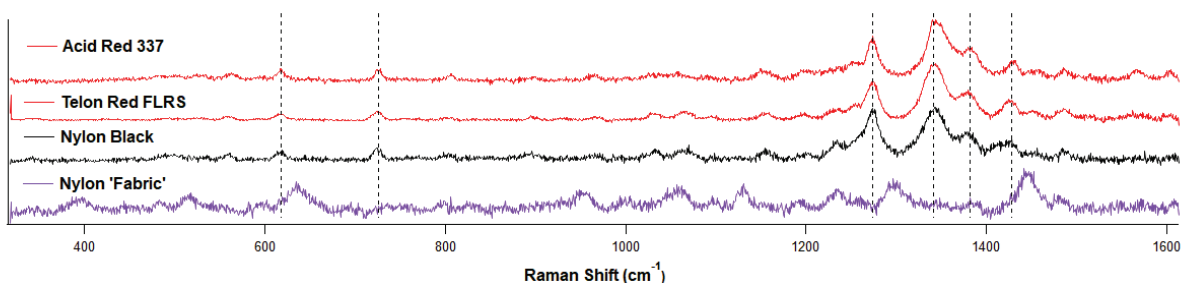


Figure 56. The corrected, overlaid and scaled spectrum of Acid Red 337 (red, top), Telon Red FLRS (red, lower), Nylon Black (black) and Nylon fabric (purple). Dashed lines are added to highlight similarities between spectra.

To further understand this, we look at the absorption spectrum of each acid dye solvated in water. As depicted in Figure 57, each dye has a broad absorption spanning much of the visible region. To illustrate the spectral window of interest, the Raman spectrum of cyclohexane (standard) is overlaid to show the Stokes and antiStokes regions. Here, we see that the 532 nm is resonant with dyes Acid Red 337, Acid Blue 260 and Acid Blue 62 and pre-resonant with Acid Orange 67. The strong overlap with the absorption of Acid Red 337 is likely the cause of the strong Raman signal compared to other dyes. To circumvent this issue, we will be trying different wavelength lasers, specifically ones with $\lambda > 700 \text{ nm}$

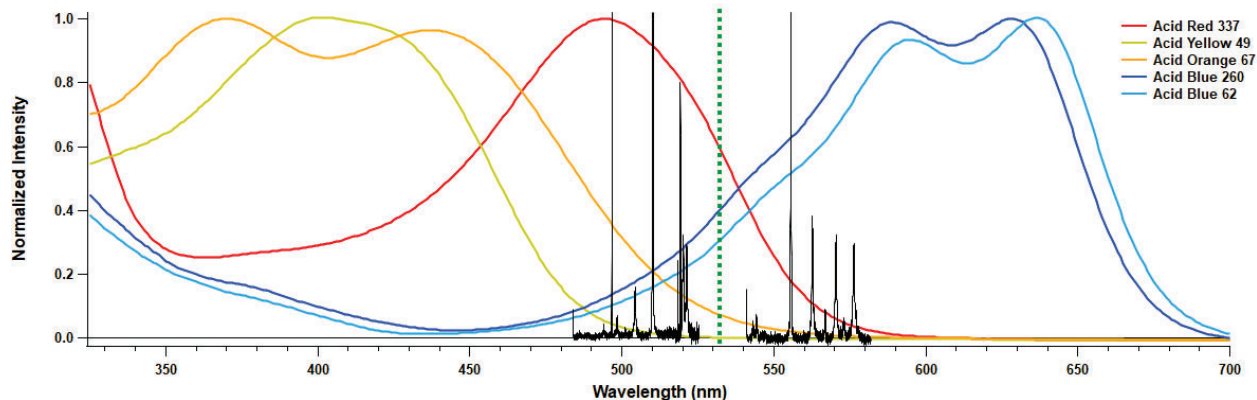


Figure 57. The normalized absorption spectrum of acid dyes dissolved in water. The Stokes and anti-Stokes Raman spectra of cyclohexane is overlaid when excited with 532 nm laser light (green dashed line).

Near-IR Raman spectroscopy with 785 nm laser.

Using 532 nm for Raman measurements of dyes often results in a large fluorescence background as many dyes absorb in the visible wavelength range. To reduce this background, we tried using a 785 nm near-IR laser (785 nm, Cobolt NLD™ 120 mW) for our Raman measurements. Hübner Photonics loaned us this laser for several weeks to evaluate its performance for Raman measurements on dyes. Its wavelength is outside the absorption range of most dyes while at the same time, it has adequate power for Raman measurements (scattering scales with $1/\lambda^4$).

To test the performance, we chose cyclohexane as a standard since it has a known spectrum, having 5 distinct peaks in the region of interest. Figure 58 shows the Raman spectrum of cyclohexane with 785 nm irradiation collected with a CCD camera (Princeton Instruments Spec-10) and with a PMT (Hamamatsu R9110). The CCD gives adequate signal to near 1700 cm^{-1} in the Stokes region but little to no signal in the anti-Stokes region. This observation demonstrates that the detector's capabilities should be sufficient since efficiencies increase at shorter wavelengths. However, the relatively low power of the laser may be of concern for anti-Stokes collection since these intensities are generally much weaker. Similarly, the PMT has increasing efficiency at shorter wavelengths, but testing resulted in much weaker signals in both the Stokes and anti-Stokes regions along with significantly greater integration times.

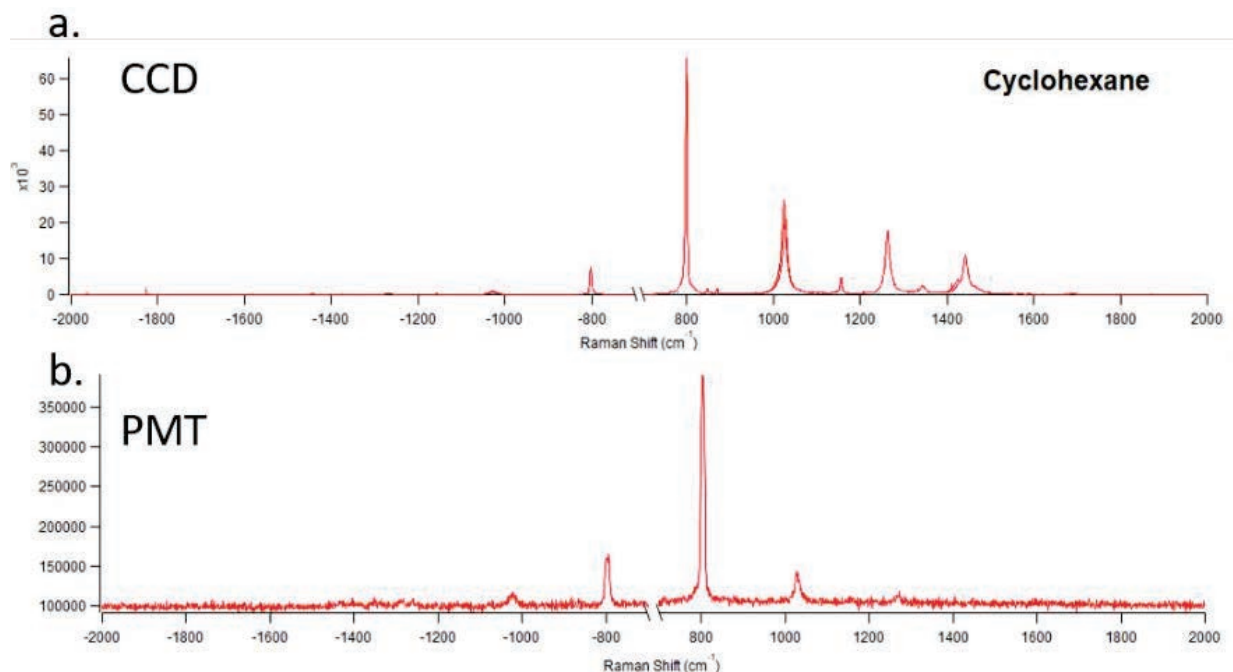


Figure 58. Comparison of CCD and PMT response.

Unfortunately, we found the collection of Raman signals of dyes using the near-IR laser to be problematic. Even though absorption of laser light from the dyes was avoided with the longer wavelength laser, small amounts of ambient scattering was collected in the spectrograph causing an etaloning background. This phenomenon is well established for CCD detectors as silicon becomes partially transparent at long wavelengths. Figure 59 displays the attempted Raman signals collected for a dyed “Black Fabric” showing the strong, periodic etaloning which becomes more persistent further to the red. This etaloning effect becomes strikingly more persistent with more reflective materials such as powder dyes Acid Orange 67 (AO67) and Acid Yellow 49 (AY49), see Figure 60. We are currently exploring alternative detectors to help circumvent these shortcomings.

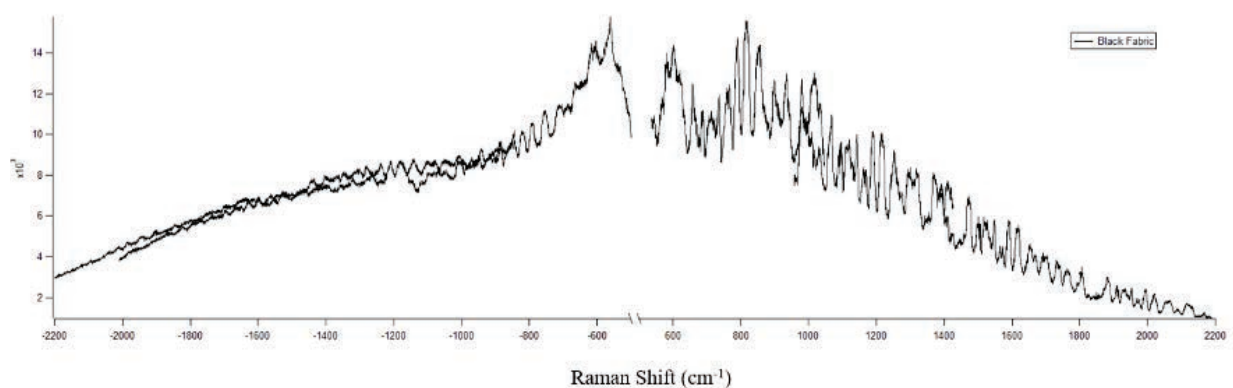


Figure 59. Raman signals collected for a dyed “Black Fabric” showing the strong, periodic etaloning which becomes more persistent further to the red.

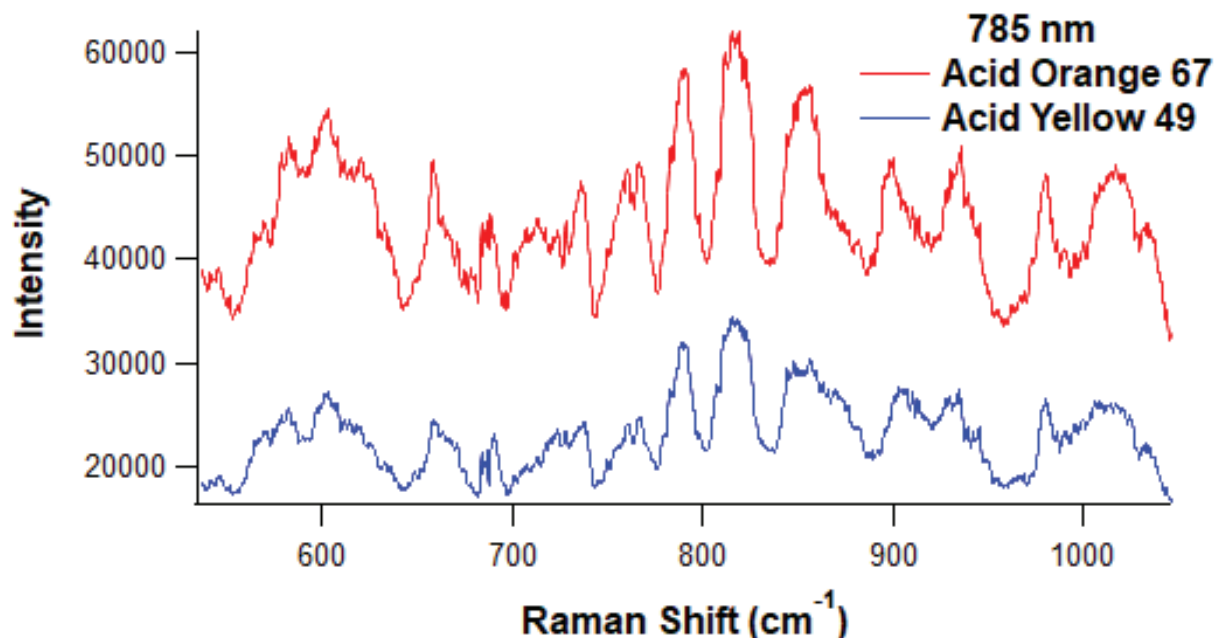


Figure 60. Etaloning effect becomes strikingly more persistent with more reflective materials such as powder dyes Acid Orange 67 (AO67) and Acid Yellow 49 (AY49).

Raman spectroscopy of mixed dye samples.

To evaluate the ability of Raman spectroscopy to quantify trace amounts of different dyes, we prepared colored nylon samples containing different relative amounts of dyes. Figure 61 shows three fabrics that were prepared with different amounts of AY49 and AO67. From left to right, we observe that the 50:50 dyed sample is very orange, becoming increasingly lighter as the orange concentration is decreased. When only 1% AO67 is used, the fabric becomes a vibrant yellow.



Figure 61. Fabrics prepared with different amounts of AY49 and AO67. The 50:50 dyed sample is very orange, becoming increasingly lighter as the orange concentration is decreased. When only 1% AO67 is used, the fabric becomes a vibrant yellow.

We performed Raman measurements on these samples via 532 nm irradiation, see Figure 62. Upon laser irradiation, we observe strong fluorescence and scattering backgrounds that change shape depending on the relative concentrations. Although 532 nm light should avoid the absorption of the solvated dyes (see report ending June 2019), due to intermolecular interactions, the absorption spectrum of dyes in “solid” form tends to extend to longer wavelengths. The spectra shown in Figure 62 highlight the challenge of differentiating between different dye components and their relative concentrations and the most appropriate laser wavelength to be used.

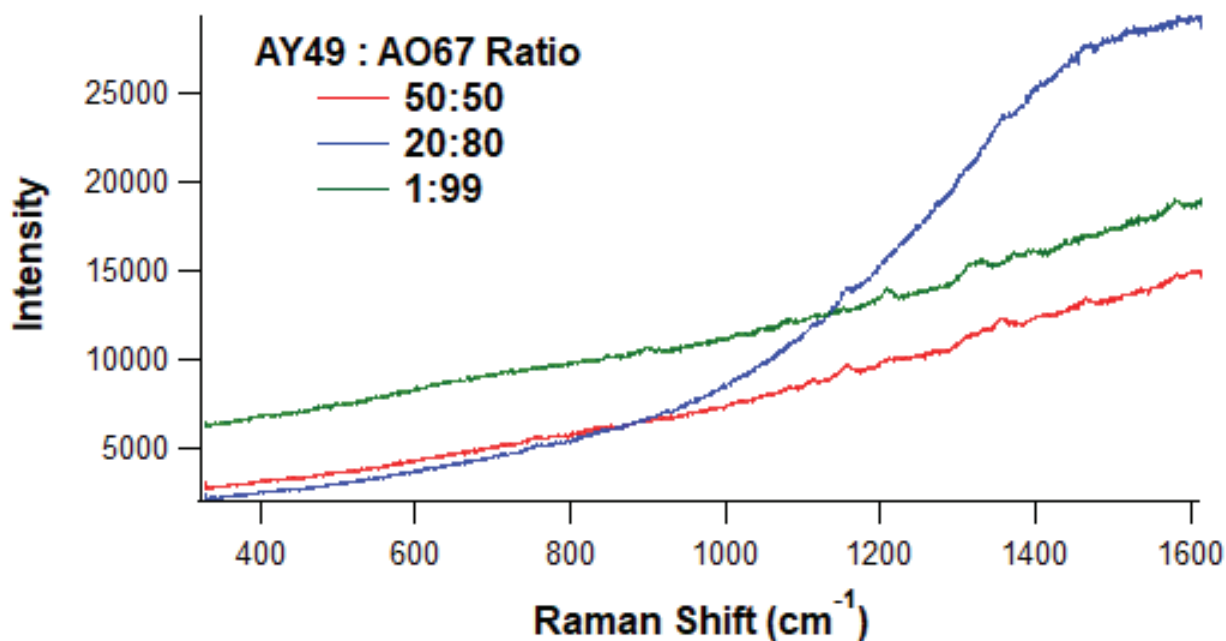


Figure 62. Raw spectra of dyed fabrics presented in Figure 55. As the relative dye concentrations change, the stray scattered light entering the spectrograph changes in shape and amplitude.

To further explore the effect of relative concentrations of mixed samples, we investigated the commercial dye powder Permasil Rubine. The relative concentrations of the individual components making up this dye are unknown. Figure 63 shows microscope images (2x magnification) of this dye powder, as-purchased (left) and after an attempted solvation (right). The solubility was tested in methanol, dichloromethane, ethanol, water, acetone, and acetonitrile—all of them showed only limited solubility and the particle size is relatively large. The particle size ($>100 \mu\text{m}$) of this dye is much larger than the laser spot size used for Raman spectroscopy ($\sim 5\text{-}10 \mu\text{m}$).

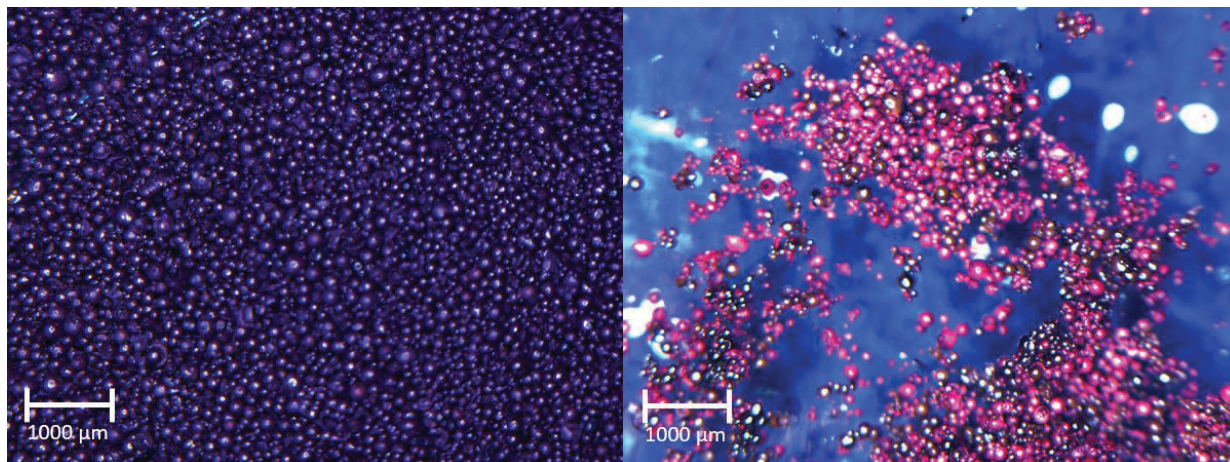


Figure 63. Microscope images (2x magnification) of commercial dye powder Permasil Rubine. The left image shows the dye as purchased. The right image shows the same dye after trying to solvate it.

To achieve a more uniform size distribution on the sub-micron scale, we dissolved specific dyes in water and prepared our own dye mixture in desired concentrations. Specifically, we chose Acid Red 337 (AR337)

and Acid Yellow 49 (AY49). The dyes were massed out in appropriate ratios and placed in vials. The mixtures were then solvated with water to uniformly disperse them. Acetone was added to evaporate the water more quickly and the solutions were then dried in glass dishes and scraped into sample dishes. The observed sample color lightens with less contribution of AR337 compared to AY49. Figure 64 shows the microscope images of three different mixtures. Each sample shows a uniform color indicating that the two components are thoroughly mixed and can be used for Raman spectroscopy.

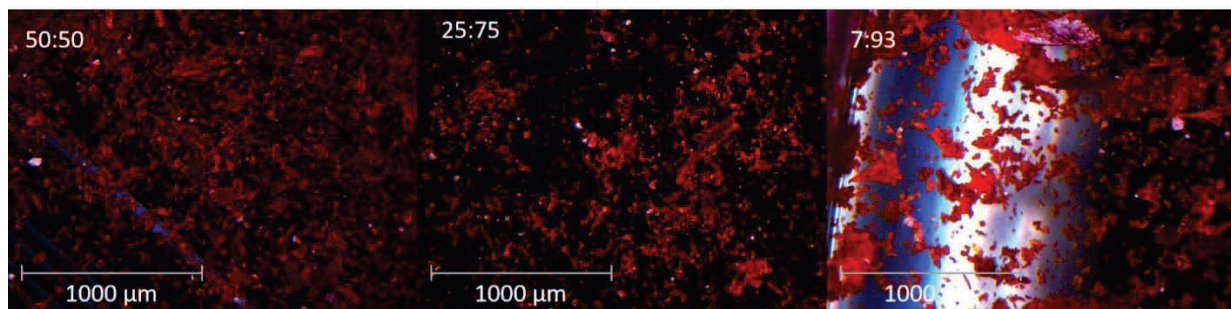


Figure 64. 8x magnification images of recrystallized dye samples of AR337 and AY49. The relative ratio of AR337 to AY49 are 50:50 (left), 25:75 (center), and 7:93 (left).

Figure 65 shows the corrected Raman spectra of pure dyes AR337 and AY49 as well as the three mixtures. The spectra of AR337 and AY49 have distinct bands at 1300 cm^{-1} and 1210 cm^{-1} , respectively. The relative Raman signal strength from the two dyes is about equal when they are mixed in a 7:93 ratio, indicating resonance enhancement of AR337. AR337 also attenuates more light, leaving less for Raman scattering from AY49. In this particular case, we can detect trace amounts of AR337.

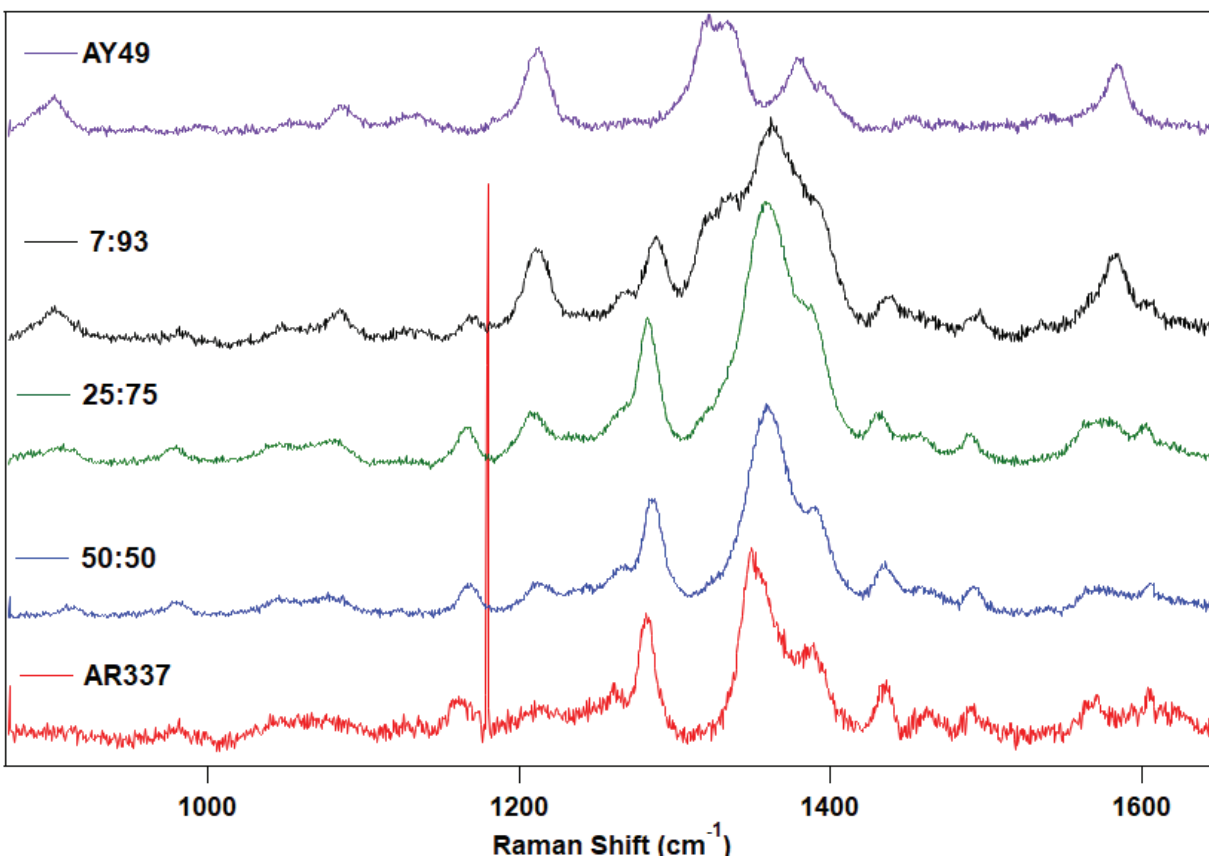


Figure 65. Corrected Raman spectra of pure dyes AR337 and AY49 as well as the three mixtures.

Reference Raman Measurements

The integrating cavity will be used to perform Raman measurements of dyes. For comparison, we performed reference measurements of the dyed fabrics, powder dyes, and dye solutions without a cavity. These comparison measurements will help to determine if the integrating cavity is providing an advantage over standard, non-cavity, measurements. We used the same Raman setup as described in our previous report, using a 532 nm laser, to characterize dyes containing AR337 and AY49, see Figure 66. With these dyes, the acidic SO_3H group forms a bond with the basic amide group of nylon.

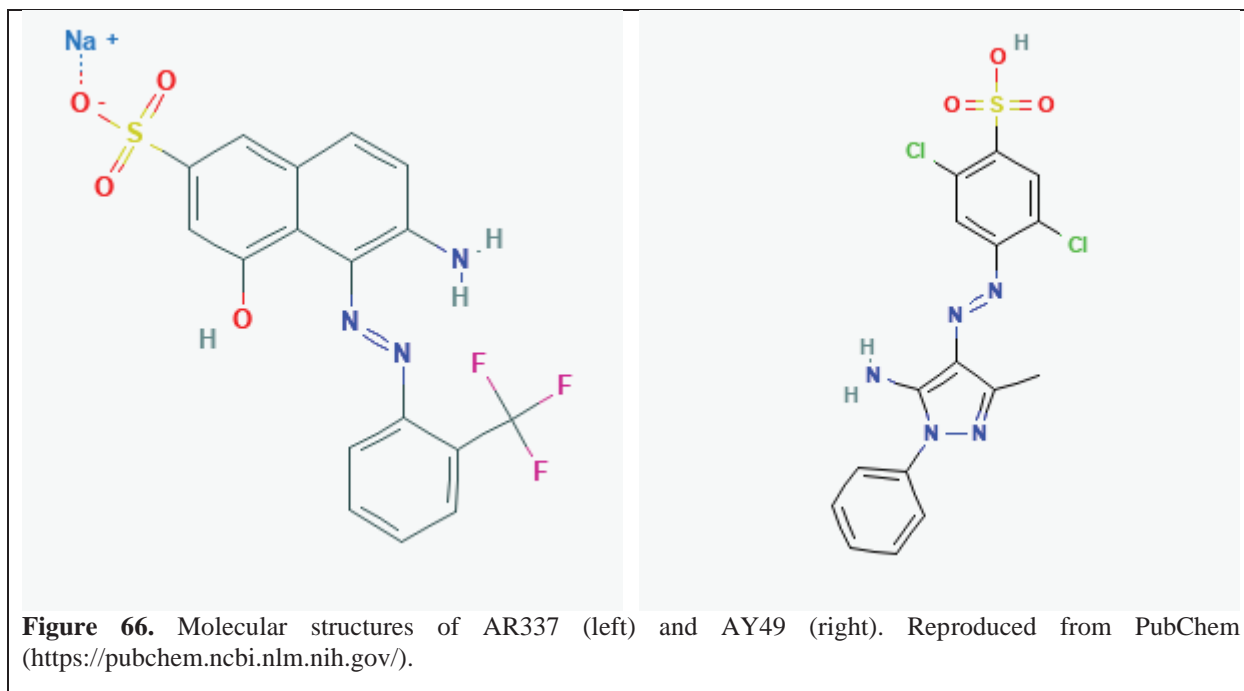


Figure 67 shows reference Raman spectra of various dyed nylon fabric swatches, including pure AR337 and AY49 dyes, different mixtures of these two dyes, a black dye, and a clean nylon sample. We subtracted the fluorescence background from all data sets.

Several observations can be made:

- (i) Some of the Raman peaks of the nylon substrate appear to show up in some of the dyed fabrics Raman spectra. However, not all of them are apparent.
- (ii) The pure AY49 dyed fabric has no discernable Raman spectrum for 532 nm.
- (iii) The fabrics containing AR337 have a clear Raman signal, even at concentrations as low as 7%.
- (iv) The black fabric contains AR337.

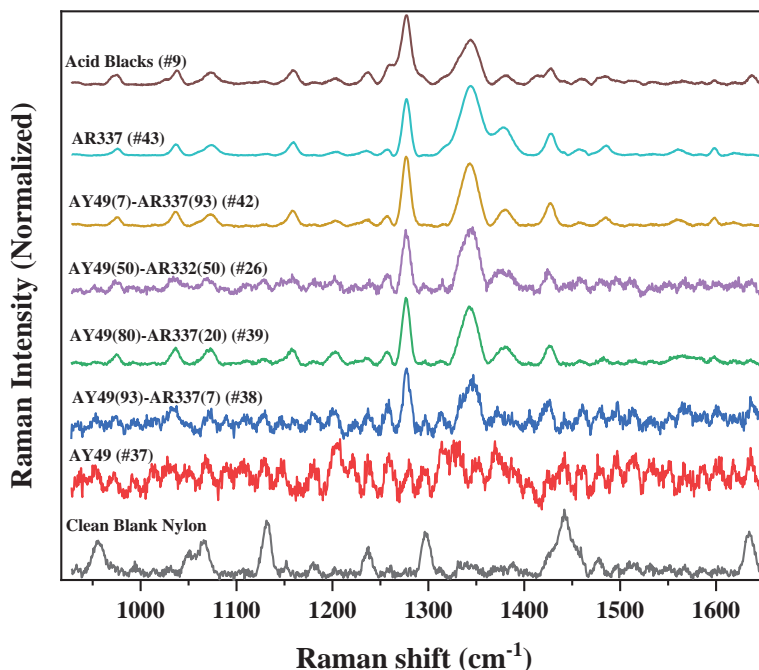


Figure 67. Standard 532 nm Raman measurements of various dyed nylon fabric swatches.

To get a better understanding of why the pure AR337 and AY49 fabric swatches have such different Raman signals, we performed additional Raman measurements on the individual dye powders, and their solutions (50% methanol, 50% water). Figure 68 shows the standard 532 nm Raman spectra of the AR337 powder, AR337 in solution, and AR337 dyed nylon. To achieve sufficient S/N, the measurements required significant acquisition times: 10 minutes for the powder, 5 minutes for the solution, and 3 minutes for the fabric, with the latter yielding the best results. The normalized plot highlights the different S/N levels and differences in peak position, peak width, and relative peak intensities, although the overall structures of the spectra are very similar.

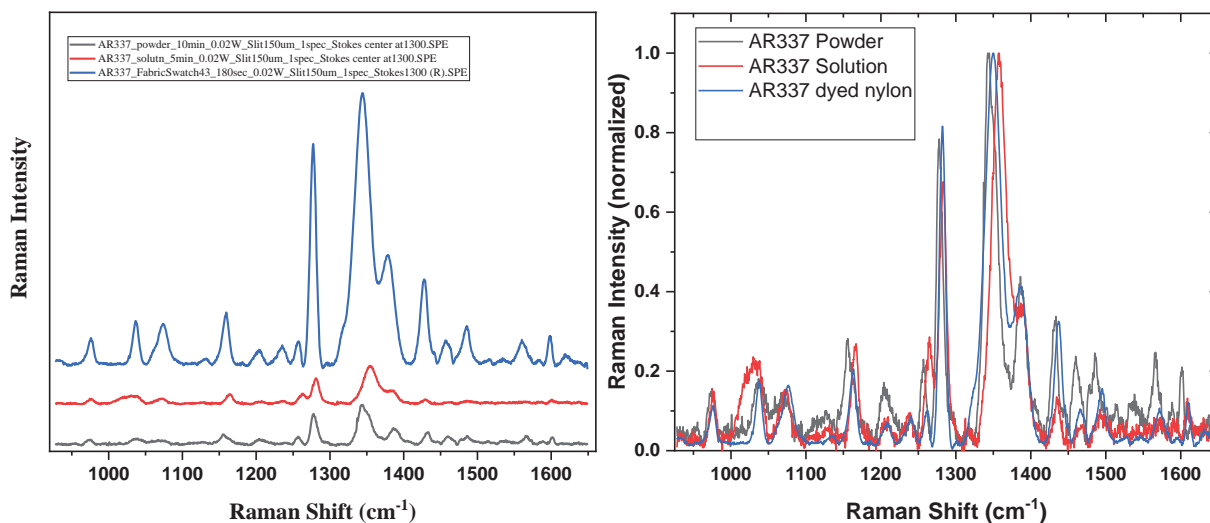


Figure 68. Standard 532 nm Raman spectra of AR337 powder, solution, and dye fabric, as measured (right) and normalized (left).

Figure 69 shows the same type of data for AY49. Again, to achieve sufficient S/N, the measurements required significant acquisition times: 1 minute for the powder and 5 minutes for the solution. Signal from the fabric sample could be collected only for 6 seconds before the fluorescence signal overwhelmed the detector response. Because of the short acquisition time, no discernable Raman peaks can be identified in the fabric sample. On the other hand, the signal from the solution shows a very good S/N with clearly defined peaks. The signal from the powder is in between, with some discernable structure.

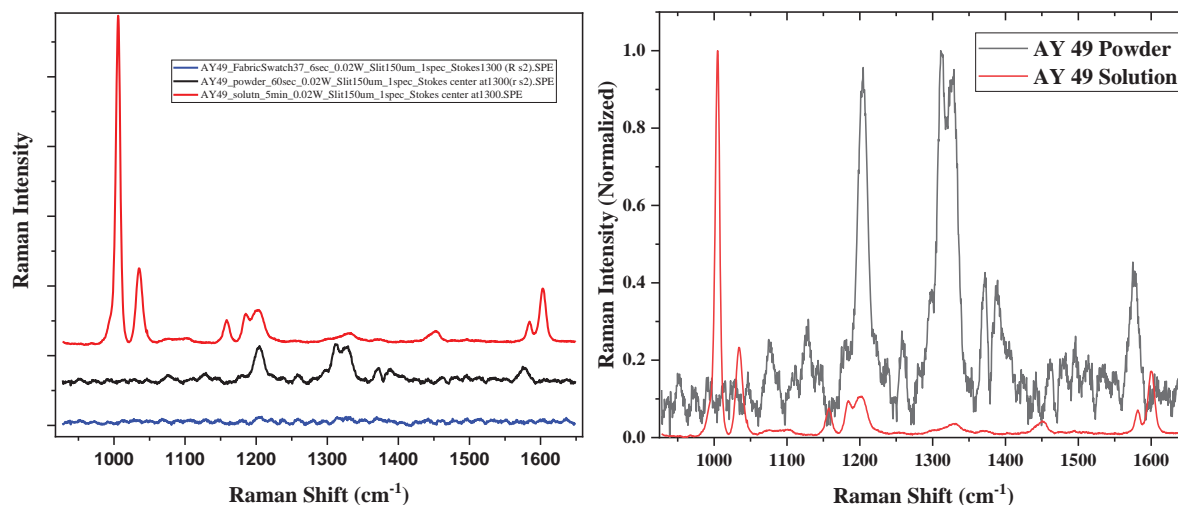


Figure 69. Standard 532 nm Raman spectra of AY49 powder, solution, and dye fabric, as measured (right) and normalized AY49 powder and solution spectra (left).

The observed differences highlight the general challenges related to the characterization of dyes. Interestingly, the spectra of the powder and the solution show significant differences for AY 49 and some of the peaks are clearly associated with the liquid phase while others are clearly associated with the solid phase. The peak near 1000 cm^{-1} could be associated with the C-O stretch mode of methanol, but then it would be surprising why this peak does not appear in the AR 337 solution spectrum, although some of the methanol could have evaporated.

Fluorescence Measurements

After measuring multiple dyes using standard Raman measurements, we down-selected two dyes for additional measurements: AR337 and AY049. Both dyes are found to have significant fluorescence, which interferes with Raman measurements at 532 nm. To get a better sense of the extent of the dye's fluorescence spectra we measured both dyes doped into nylon fibers using a standard fluorescence spectrometer using 355 nm excitation. Figure 70 shows the resulting fluorescence spectra.

From Figure 70 we find that both dyes have broad fluorescence peaks covering a significant portion of the visible spectrum. This is consistent with our previous observation of significant fluorescence emission during Raman measurements using 532 nm excitation. Note that for AR337 the broad peak centered near 620 nm is due to the dye, while the peak at 420 nm is most likely due to background optics fluorescence. The reason why it shows up in the AR337 spectra and not the AY049 spectra is that AY049's fluorescence is found to be significantly brighter than AR337, so we get better signal-to-background than with the AR337. These dye measurements suggest that DUV Raman could completely eliminate the contribution of fluorescence.

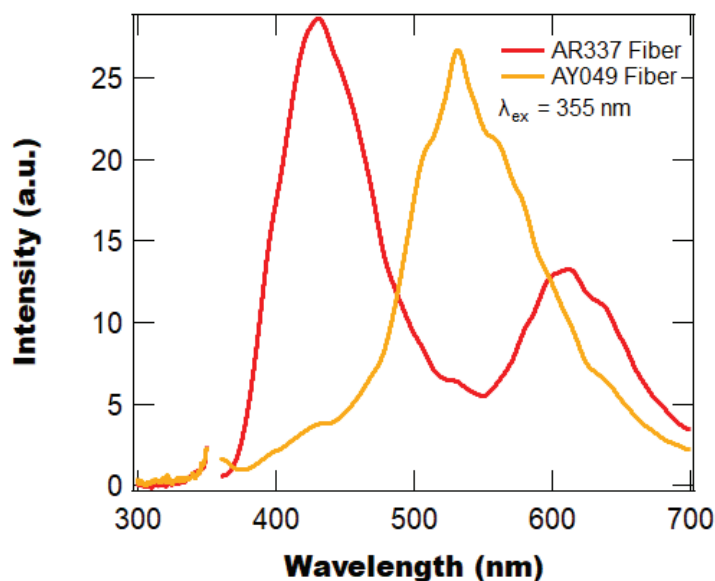


Figure 70. Filtered fluorescence spectra of nylon fibers dyed with AR337 and AY049.

Optical Cavity

In the previous reporting period, we prepared two different optical cavities using Aerosil, one in Sep 2020 (average reflectivity of 98.7%) and one in December (average reflectivity of 99.75%). In our testing with both cavities, we were unable to get good signal from the cavity due to poor output coupling from the cavity as we were directly coupling into a fiber without any lenses. To improve coupling efficiency, we therefore designed a “peep hole” optical coupler consisting of three concave lenses and one convex lens. The three concave lenses collect a wide angle of light into a collimated beam which is then focused into a fiber using the convex lens. Figure 71 shows a schematic ray diagram of the lens system.

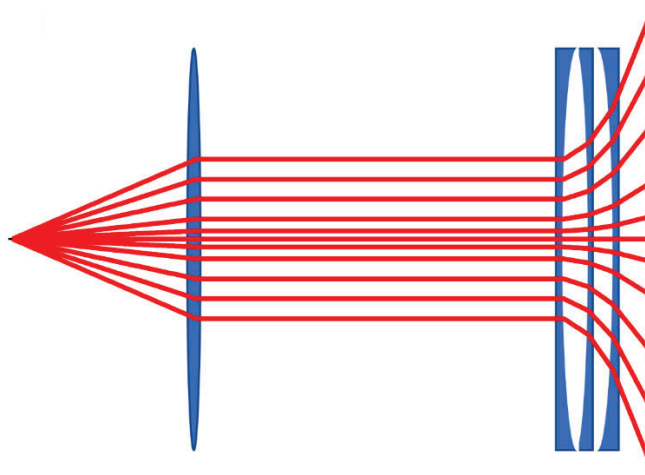


Figure 71. Ray trace diagram of lens stack.

Using ray matrix formalism, we can calculate the acceptance angle for the concave lens stack which couples into the fiber with an axis angle θ :

$$\Phi = \frac{f_1(d^2 + 4df + 3f^2)}{f^3}$$

Where d is the spacing between concave lenses, f is the concave lenses' focal length, and f_1 is the convex lens' focal length.

For our lens assembly we purchased four 6 mm diameter UV Fused silica lenses (3 with $f = -10$ mm and one with $f = 15$ mm), quartz O-ring spacers (1 mm thickness, 6 mm OD, 4 mm ID), SM05 mountings for coupling into the fiber, and a 355 nm long pass filter to keep pump light from entering the fiber. Initially we used scotch tape to hold the concave lenses and spacers together, but testing revealed significant fluorescence from the scotch tape. We then tested electrical tape (e. tape) and found less fluorescence (see Figure 72 for a comparison of both tapes), but even this amount of fluorescence was too great to resolve other signals. We therefore redesigned the lens assembly to use a Norland Optical Adhesive 63 (NOA63). Direct measurements of this new adhesive showed no discernable fluorescence.

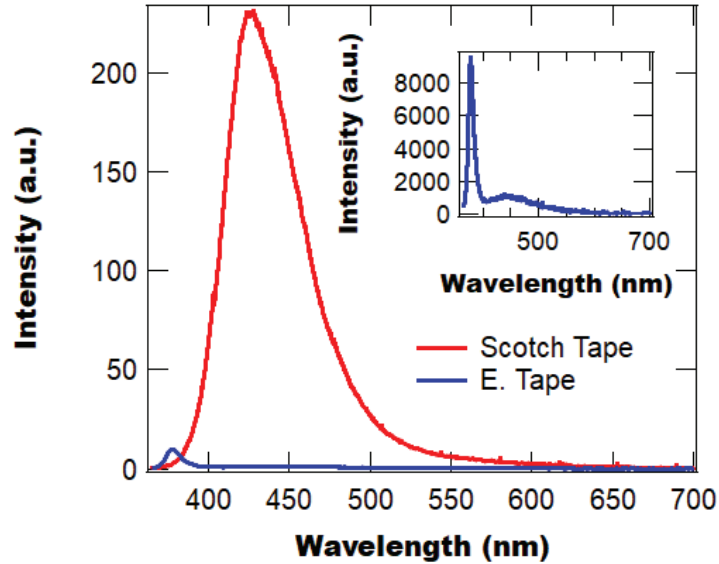


Figure 72. Fluorescence spectra of tape.

Once the new lens assembly design was assembled using the new adhesive, we once again measured the fluorescence background of the cavity, with disappointing results. While the adhesive by itself displayed no discernable fluorescence, the cavity still showed fluorescence. At first we believed this to be due to residual contamination of the electrical tape adhesive, but upon closer inspection we realized that the UV peak for the most recent cavity does not line up with the peak associated with the electrical tape adhesive, as shown in Figure 73. Further work is required to understand the source of this fluorescence.

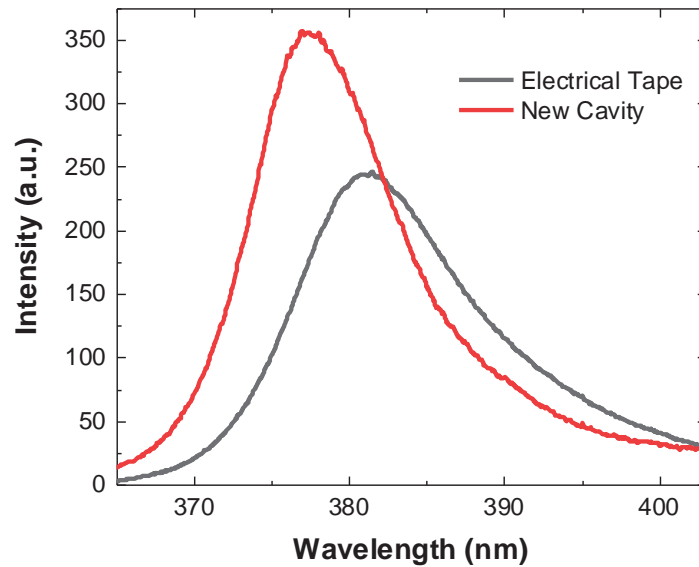


Figure 73. Comparison of cavity and electrical tape fluorescence demonstrating that the peaks are not the same.

Cavity Ringdown with Lens Assembly

Given the change in the interior surface area of the cavity (due to a larger hole for the lens assembly) we anticipate that the average reflectivity of the cavity will not be the same as measured before. We therefore reperformed the cavity ringdown measurements with the modified cavity and find a new reflectivity of

99.58%, which is less than the previous value of 99.75%. While this appears to be a small change in reflectivity, it results in a rather significant drop in cavity enhancement. For the 99.75% cavity we predict an enhancement of $\approx 300x$, while the 99.58% value is predicted to have an enhancement of $\approx 178x$. Note that we may be able to reduce the impact of the larger output coupler by using a larger cavity.

Cavity Raman/Fluorescence Measurements

Having assembled a working cavity (albeit still with some fluorescence issues) we next performed optical spectroscopy measurements on three different samples (two dyes and BaSO₄). The first dye sample tested was a DO11 dye-doped polymer on a quartz slide, which was previously measured using the fiber-only coupling design.

Figure 74a shows the fluorescence spectra measured using a standard spectroscopy system and the cavity system with the sample lying flat on the bottom of the cavity and also angled against the wall (so that it is not laying flat). While we found that the new cavity coupling design provided significantly improved signal and that angling the sample improved our signal, these spectra are still significantly less intense than the standard spectroscopy system.

Also of interest is that the spectral shape changes between the standard and cavity measurements, as shown in Figure 74b. From Figure 74 b we find that peak appears to have red-shifted. This shift is due to self-absorption of the fluorescence by the dye sample and is normally only observed in long pathlength samples. This confirms that the cavity is successfully increasing the optical pathlength, however this improvement is still not sufficient to overcome losses related to coupling efficiency.

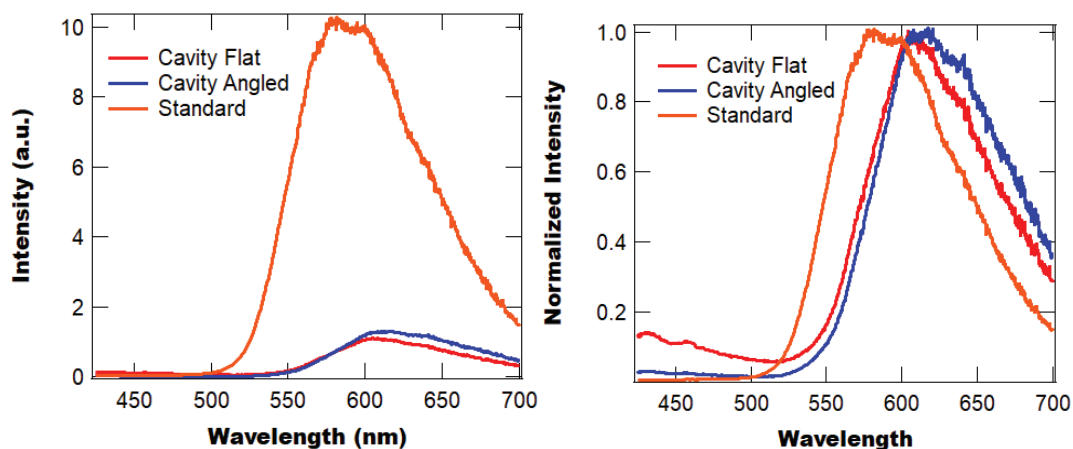


Figure 74. Fluorescence spectra of DO11 dye-doped polymer measured using cavity and standard spectrometer.

While the dye measurements using DO11 dye-doped polymer did not reveal any improvement over the standard spectroscopy system, we did observe some improvement when we tested AY049 dissolved in a methanol solution. Figure 75 shows the fluorescence spectra measured for the AY049 solution using both the standard and cavity spectroscopy setups. While the spectra are more intense from the cavity, there are also some anomalies that are still under investigation. Namely there is a sharp peak near 680 nm that arises from the quartz crucible holding the dye solution and an unexpected intensity offset. Measurements of the empty crucible show negligible background intensity from 550 nm to 660 nm, so we would expect the tail of the AY049 peak to go to zero, but we find an offset.

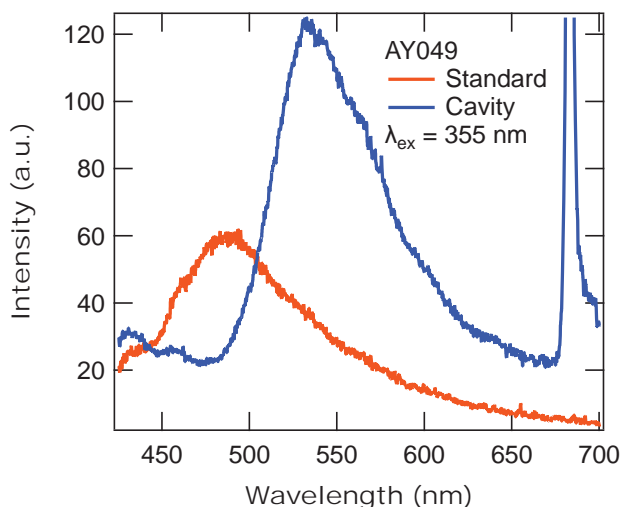


Figure 75. Fluorescence spectra of AY049 dissolved in methanol measured using the standard spectroscopy system and the cavity system. Note that the sharp peak near 680 nm arises from the crucible.

Additionally, for the standard spectroscopy measurement we observe a peak near 490 nm, which is significantly blue shifted from the peaks observed in the cavity measurement and in the dye-doped nylon fibers. This may be due to significant self-absorption in the cavity (which may also be replicated by high concentrations in the nylon fibers), but further work is needed to determine the mechanism definitively.

Finally, we attempted to perform Raman spectral measurements on BaSO₄ in the optical cavity. This proved a significant challenge due to all the other signals coming from the cavity materials in the spectral region of interest. Figure 76 shows the emitted spectra from the cavity both with and without BaSO₄ and there is no clear Raman peak near 1000 cm⁻¹ (BaSO₄'s strongest peak). However, after performing some scaling and subtraction of the two spectra we successfully found a Raman peak near 1000 cm⁻¹, but this is significantly weaker than standard measurements.

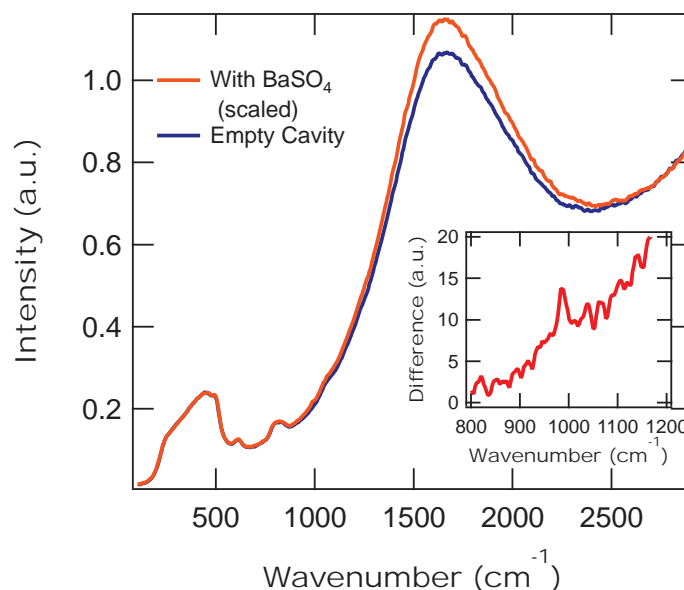


Figure 76. Emission measured from empty cavity and cavity containing BaSO₄. Inset: difference spectra showing weak BaSO₄ Raman peak.

Raman Measurements

During the current reporting period, we modified our existing Raman setup to extend the spectral range into the terahertz (THz) region (i.e., wavenumbers below 200 cm⁻¹). We used a reflective Bragg filter (RBF) to narrow the laser line width and Bragg Notch Filters (BNF) to narrow the spectral region for the blocking of scattered laser light, see Figure 77 and Table 27.

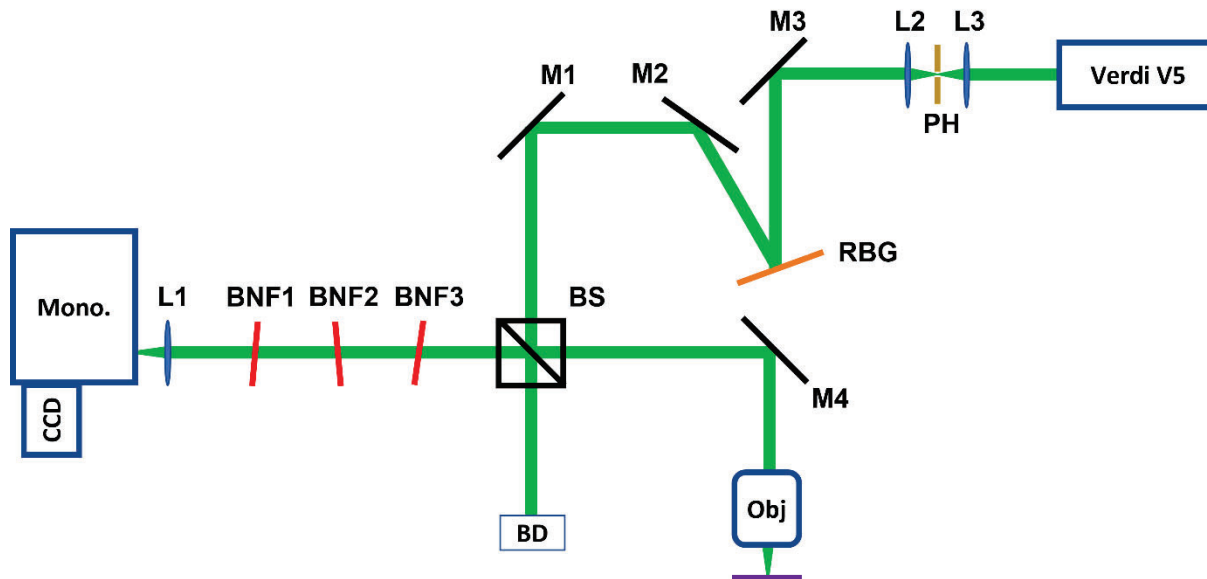


Figure 77. Schematic of THz Raman spectrometer. The Reflective Bragg Grating (RBG) narrows the laser line and has a peak efficiency at a 20-degree incidence angle and a spec'd spectral bandwidth of $< 7 \text{ cm}^{-1}$. Each Bragg Notch Filter (BNF) is spec'd to be OD3 with a notch width of $< 10 \text{ cm}^{-1}$.

Table 27. Relevant specs for spectrometer components.

Item	Relevant Specs
Verdi V5	5 W, $\lambda_0 = 532 \text{ nm}$, $\Delta\nu < 5 \text{ MHz}$ ($1.668 \times 10^{-4} \text{ cm}^{-1}$), 2.25 mm diameter
RBG	$\lambda_0 = 532 \text{ nm}$, $\Delta\nu < 7 \text{ cm}^{-1}$, 90% efficiency
BNF	$\lambda_0 = 532 \text{ nm}$, $\Delta\nu < 10 \text{ cm}^{-1}$, OD 3

To characterize the spectrometer's wavelength calibration, we measured emission lines from both a Hg and Ne lamp in the 500 nm – 600 nm range. Table 28 lists the measured wavelength errors for the different lines. The absolute average wavelength error is 0.011 nm, which corresponds to 0.335 cm^{-1} . Note that some of the lines are second order diffractions from the UV.

Table 28. Measured wavelength errors for lines of Hg and Ne in the 500 nm - 600 nm range. The average error is 0.011 nm (0.335 cm^{-1}) and the rms error is 0.003 nm.

Ion	Line Wavelength		Measured Error	
	nm	Rel. cm^{-1} ($\lambda = 532 \text{ nm}$)	nm	cm^{-1}
Hg	507.3034	-915.077	-0.00563	-0.22
Hg	530.408	-56.4185	0.007218	0.26
Hg	530.735	-44.8024	0.007126	0.25
Ne	533.078	38.01162	0.009778	0.34
Ne	534.109	74.22241	0.009953	0.35
Ne	540.056	280.3942	0.011416	0.39
Hg	546.075	484.4896	0.01733	0.58
Hg	576.961	1464.798	0.011731	0.35
Hg	579.067	1527.834	0.009738	0.29
Ne	585.249	1710.248	-0.01928	-0.56
Ne	588.19	1795.683	-0.01509	-0.44

Hg	593.456	1946.544	-0.00775	-0.22
Ne	594.483	1975.654	-0.00858	-0.24
Ne	597.553	2062.075	-0.00674	-0.19

After calibrating the spectrometer, we measured the laser line's spectrum, see Figure 78, and find that it is not centered at 532 nm as expected, but is actually centered near 532.05 nm. This difference is outside of the calibration error, which means that this is a real offset and not just a calibration error. Also, we find that the measured spectrum's linewidth is spectrometer limited to near 0.04 nm, which is the predicted resolution of the spectrometer.

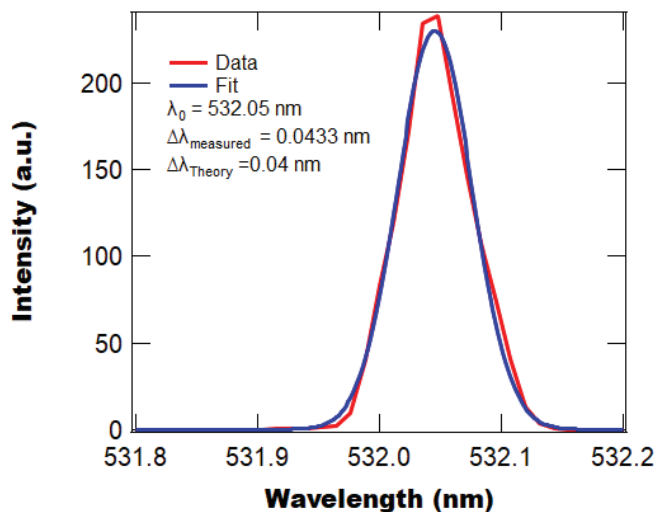


Figure 78. Laser line spectrum. The bandwidth is spectrometer limited.

We also measure the BNF filters transmission spectrum to characterize the notch filter. Figure 79 shows the transmission spectrum and laser line spectrum from which we find a FWHM of the notch filter to be 12.8 cm^{-1} , which is slightly larger than spec ($< 10 \text{ cm}^{-1}$). Interestingly, while the notch filter significantly reduces the laser line, the transmission (when measured using a white light source) only shows an OD of 2.

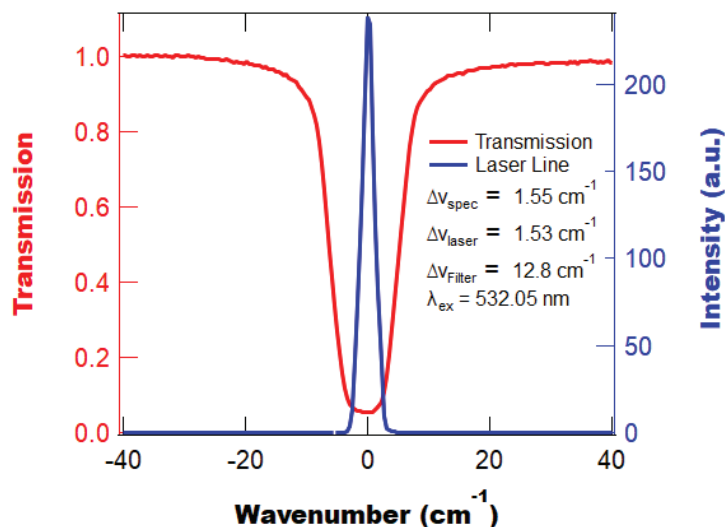


Figure 79. Transmission curve for bandpass filters and laser line for reference.

To test the THz system, we measured several crystalline samples, see Figure 80. The spectra show all the expected bands and demonstrate the ability to perform Raman measurements in the THz region.

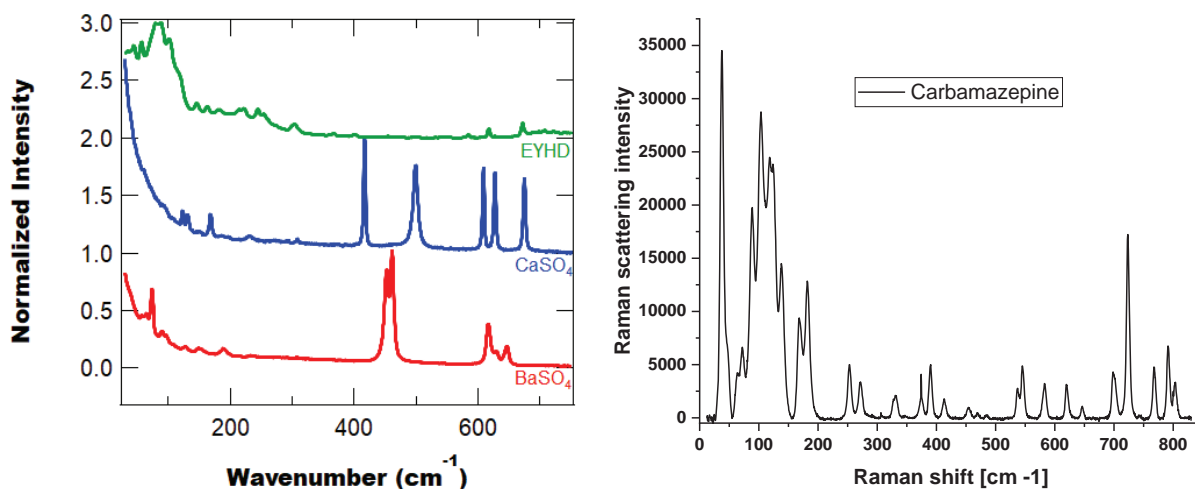


Figure 80. THz Raman spectra of several crystalline test samples.

Using this setup, we measured high-resolution Raman spectra of multiple dyed fabric swatches, dye powders, dye solutions, and references, including:

Fabric Swatches

1. Acid Black
2. Acid Blue 62 (1%), Blue 90 (99%)
3. Acid Blue 62 (20%), Blue 90 (80%)
4. Acid Blue 62 (50%), Blue 90 (50%)
5. AB 260
6. AB 62
7. AO 67

8. AR 337
9. AY 49
10. AY 49 (7%), AR 337 (93%)
11. AY 49 (50%), AR 337 (50%)
12. AY 49 (80%), AR 337 (20%)
13. AY 49 (93%), AR 337 (7%)
14. Black Permalon (provided by Standard Colors)
15. Black Permasil (provided by Standard Colors)
16. Blue Permabril (provided by Standard Colors)
17. Blue Permalon (provided by Standard Colors)
18. Blue Permasil (provided by Standard Colors)
19. Clean blank nylon
20. Clean blank polyester
21. Dispersive Black(V)
22. Dispersive Black (X)
23. DR 153 (1%), DR 60 (99%)
24. DR 153 (20%), DR 60 (80%)
25. DR 153 (50%), DR 60 (50%)
26. DY211-DX64_TerasilYellow4G (1%)_DianixYellowE-3G (99%)
27. DY211-DX64_TerasilYellow4G (20%)_DianixYellowE-3G (80%)
28. DY211-DX64_TerasilYellow4G (50%)_DianixYellowE-3G (50%)
29. Orange Permabril
30. R Blue 4
31. R Red 2
32. R Red 123
33. R Yellow 86
34. Red Permabril
35. Red Permalon
36. Red Permasil
37. Yellow Permalon
38. Yellow Permasil

Other

1. AB 260 powder
2. AR 337 powder
3. AY 49 powder
4. AR 337 in 50/50 MeOH/DI water
5. AY 49 in 50/50 MeOH/DI water
6. MeOH/DI water

Figure 81 shows THz Raman spectra of several dyed nylon samples as well as of the background.

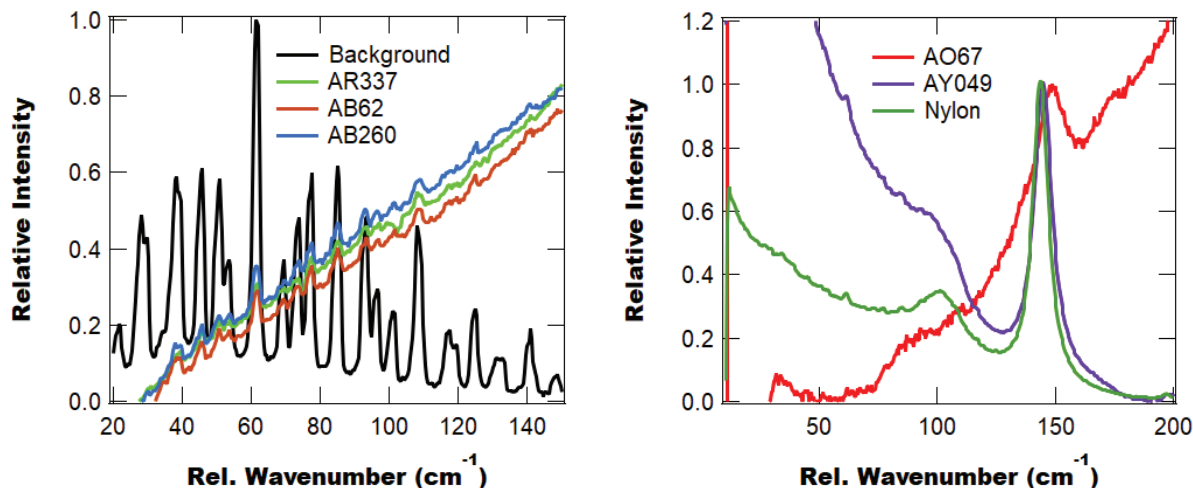


Figure 81. Example THz Raman spectra from different dyed nylon samples. The observed peaks are consistent with either the background (air) or nylon peaks.

The following discussion focuses on AR 337 dyed nylon and AY 49 dyed nylon. These two acid dyes contain R-SO₃⁻ functional groups which electrostatically interact with the protonated terminal amino groups R-NH₃⁺ of nylon, see Figure 82.

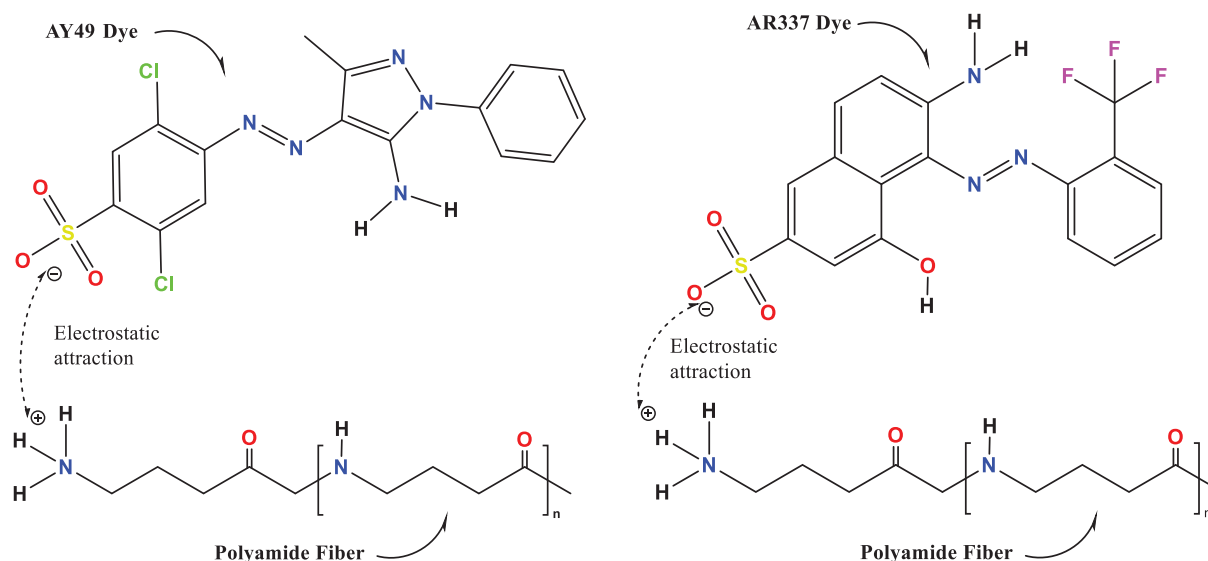


Figure 82. Bonding between AY 49 with nylon (left) and AR 337 with nylon (right).

Figure 83 shows the Raman spectra of clean blank nylon and nylon fabrics dyed with different amounts of AY 49 and AR 337: AY 49 (100%), AY 49 (80%)-AR 337 (20%), AY 49 (50%)-AR 337 (50%), AY 49 (7%)-AR 337 (93%), and AR 337 (100%). Note that the following measurements assume a laser peak position of 532.0 nm. The clean blank nylon sample has a strong band at 141.00 cm⁻¹ (THz) while the bands in the fingerprint (above 200 cm⁻¹) region are of relatively low intensity. The Raman spectrum of the AY 49 (100%) sample shows a similar behavior, with the strongest peak near 141 cm⁻¹ and a few small-intensity bands in the fingerprint region. The Raman spectrum of the AR 337 (100%) also has a strong peak near 141 cm⁻¹, but also shows strong peaks throughout the fingerprint region. The Raman spectra of the remaining samples, which are mixtures of AY 49 and AR 337, also show a strong peak in the THz region

as well as bands throughout the fingerprint region, indicating that these spectra are dominated by the AR 337 dye.

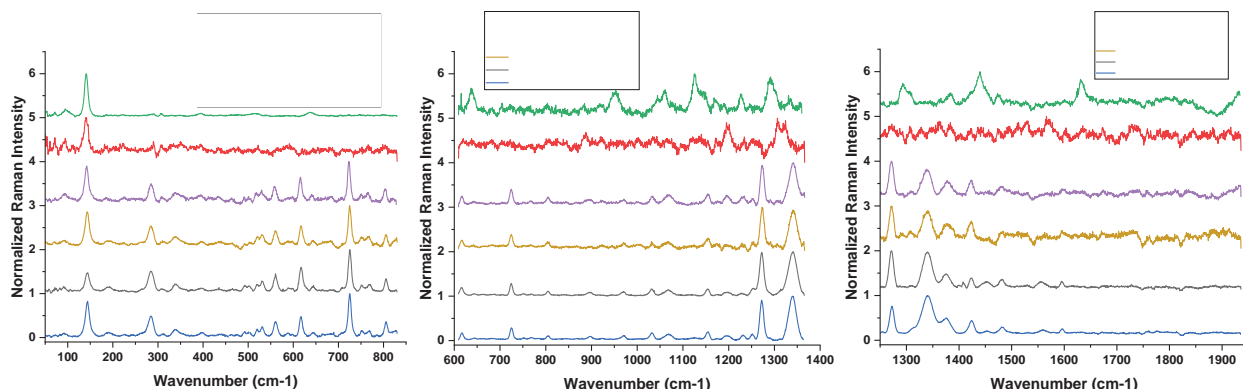


Figure 83. Normalized Raman spectra of clean blank nylon and various AY 49 and AR 337 dyed nylon samples.

Using a Lorentzian profile, we fitted the peaks to determine their peak positions. The Raman spectrum of the clean blank nylon sample is dominated by a strong band in the terahertz (THz) region at 141.00 cm^{-1} , corresponding to C-C torsions of the nylon backbone [ref]. Unlike the bands in the fingerprint region, the band at 141.00 cm^{-1} shows a clear shift when dye molecules bind with the nylon. When nylon is dyed with pure AR 337, this peak blue-shifts to 143.64 cm^{-1} , however, when nylon is dyed with pure AY 49, this peak red-shifts to 140.58 cm^{-1} . With increasing addition of AY 49 to AR 337, the blue-shifted peak at 143.64 cm^{-1} shifts back to lower energies, see Figure 84.

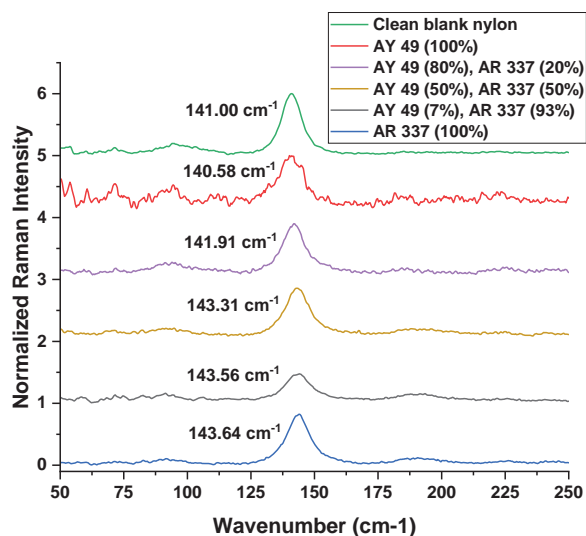


Figure 84. Peak positions based on Lorentzian fits.

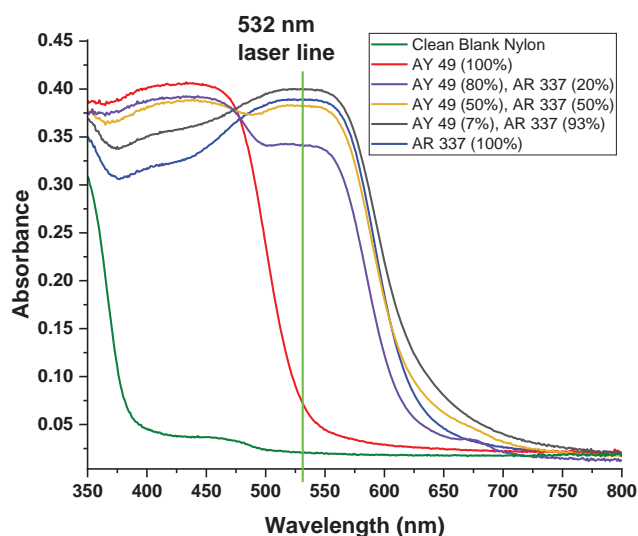


Figure 85. Visible absorption spectra of nylon and dyed nylon samples.

The red-shift observed for AY 49 dyed nylon indicates that most likely the dihedral angle for the nylon C-C backbone increased, while the blue-shift observed for the AR 337 dyed sample indicates that most likely the dihedral angle for the nylon C-C backbone decreased. The absorption spectra of the various dye samples, see Figure 85, indicates that AY 49 only minimally absorbs the 532 nm Raman laser light while AR 337 shows strong absorbance of the laser light. It therefore seems possible that we are observing a resonance effect in the AR 337 dyed samples in which the excited state configuration of the AR 337 molecule has a

stronger impact on the torsion of the C-C nylon backbone than the ground state configuration of the AY 49 dye.

To better understand the differences between the two dyes, we dissolved them in 50% MeOH/50% DI water and measured the Raman spectra of these solutions, see Figure 86. All three samples show a strong band at about 1000 cm^{-1} which can be attributed to MeOH. As we have already observed for the fabric samples, AR 337 shows a stronger and more pronounced Raman response than AY 49.

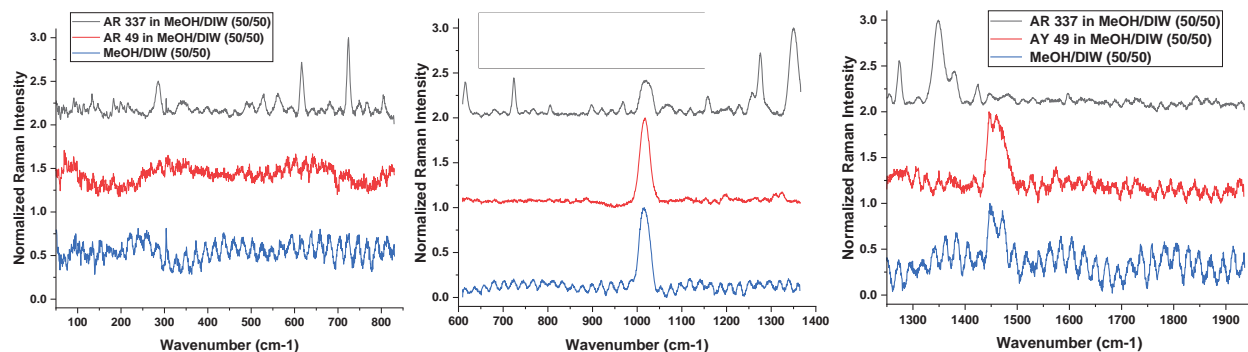


Figure 86. Raman spectra of Ar 337 and AY 49 in 50% MeOH/50% DI water and the solvent without a dye.

The measurements for AR 337 were done with a laser power of 20 mW, while those for samples containing AY 49 were done with a laser power of 50 mW. When the laser power was increased to 100 mW, the response from some of the dyed fabric samples changed, see Figure 87. With lower laser powers, the Raman scattering strength from AY 49 is significantly poorer than that from AR 337. As the laser power is increased, the Raman scattering of AY 49 increases significantly, while that of AR 337 decreases. This effect may be due to laser-induced fluorescence quenching which has been observed for other dyes.

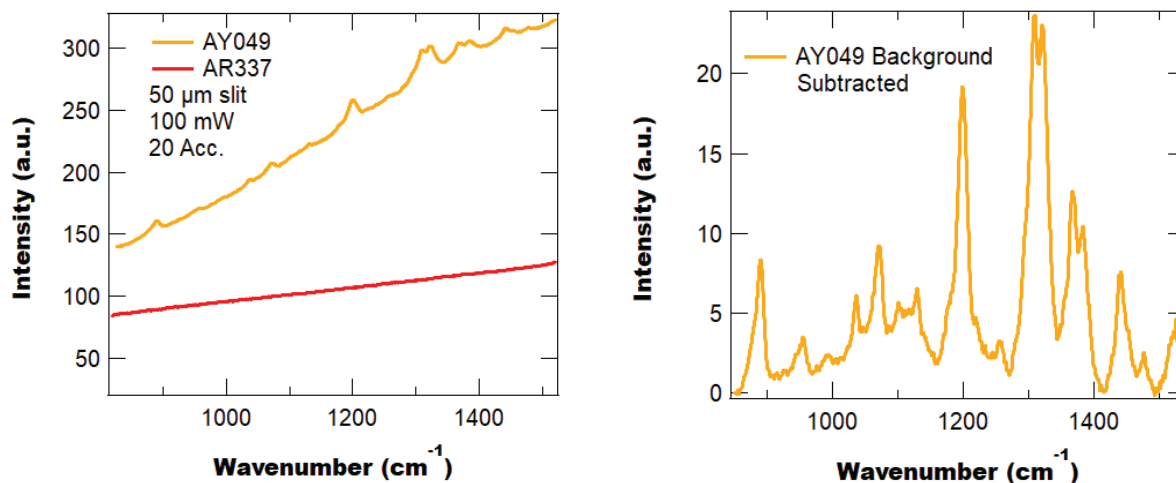


Figure 87. Raw spectra collected from AR337 and AY049 fibers using 100 mW of 532 nm excitation (left). Background subtracted Raman spectra for AY049 (right). In this set of experiments the AY049 provided excellent Raman signal, while the AR337 signal was overwhelmed by fluorescence. This result is opposite to experiments with lower laser powers.

Fluorescence Measurements

In the previous reporting period, we reported on the observation of spectral interference from fluorescence originating somewhere in the Aerosil cavity system. During this current reporting period we performed various measurements to try and identify the source of the unwanted fluorescence and discovered that its primary source is most likely due to the ground glass edges of the Thorlabs lenses we are using in the output coupling lens assembly. Figure 88 shows the normalized fluorescence measured from exciting the ground glass edges using 355 nm excitation. Interestingly, in the center of the lens there is no observable fluorescence. While it is unclear why the edges are fluorescent, we are going to attempt to overcome this issue by purchasing lenses from other vendors to see if these other vendors lenses work better.

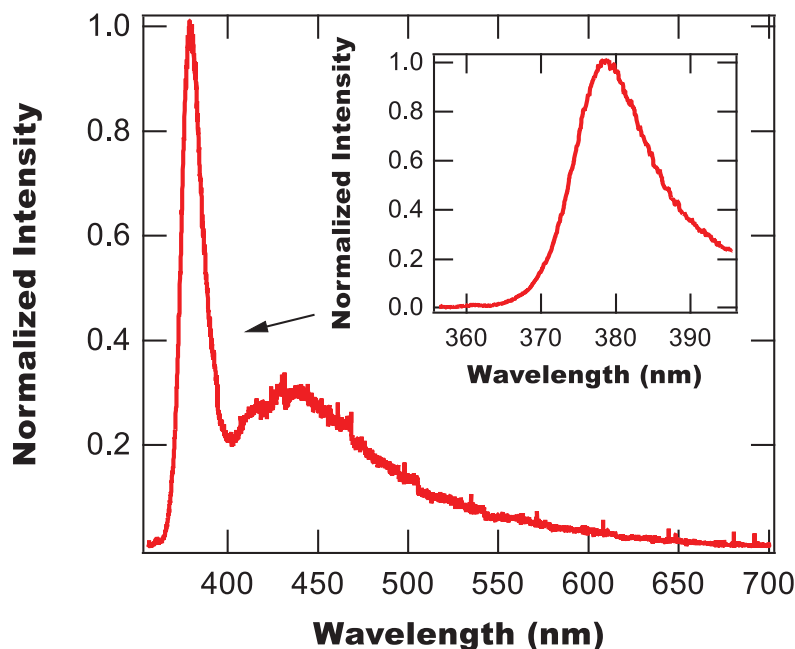


Figure 88. Fluorescence measured from edge of Thorlabs lens.

Optical Cavity

To date we have been unable to obtain good Raman results with dye samples in our cavity due to anomalous fluorescence and issues that could be related to the dyes' absorbance bands. Therefore, to demonstrate our cavity in the best-case scenario, we use it to measure the Raman signal of air using 532 nm excitation. Figure 89 shows the resulting Raman signal from the cavity with a broad background and several broad peaks most likely corresponding to scattering in the cavity, possible fluorescence from aerosols, and the input/output fibers. However, there is a small peak at 2329 cm^{-1} corresponding to Raman scattering from N_2 , which is shown in the inset. Note that we are unable to resolve a peak for O_2 at 1555 cm^{-1} as it is buried in noise. Also, while the Aerosil cavity can measure a peak from the N_2 in the cavity, it is very weak compared to the other spectral features in Figure 89 and is only slightly larger than the noise of the measurement.

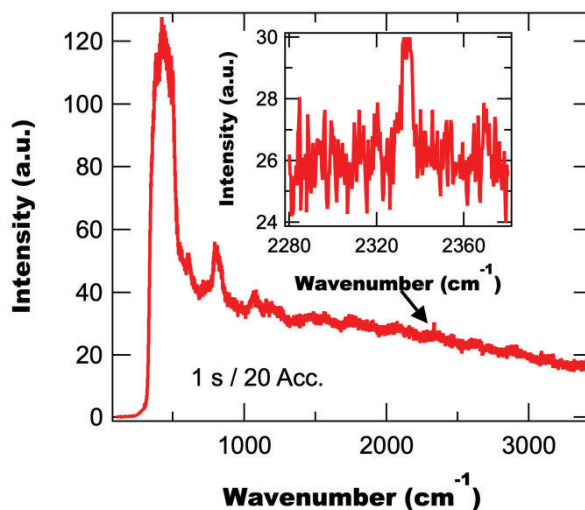


Figure 89. Emission spectrum measured from empty Aerosil cavity excited at 532 nm. Inset: small peak at 2329 cm^{-1} , which is associated with atmospheric nitrogen.

To gain a better understanding of how the Aerosil cavities performance compares to other techniques we perform measurements on air inside of a commercially available Spectralon cavity (Thorlabs) as well as in a regular Raman spectrometer. Figure 90 shows the N_2 peak measured using the two cavities for the same spectrometer settings. From Figure 90 we find that the Aerosil cavity has a larger signal-to-noise ratio than the Thorlabs cavity, which suggests that the Aerosil cavity has better performance than the Spectralon. However, the Aerosil cavity is 222.9 cm^3 in volume, whereas the Thorlabs cavity is 68.7 cm^3 . This increase in sample volume could explain a portion of this improvement.

In addition to the cavity measurements, we perform measurements using a standard Raman spectrometer. To compare between the cavity and standard Raman spectrometer we perform background subtraction and compare the peaks' relative intensity, which are shown in Figure 91. Note that this comparison is not ideal as the spectrometers used are different and the laser power is significantly different. For the cavity measurement the power incident from the fiber was 50 mW, while for the standard measurement the power was 250 mW. Also, if we estimate the interaction volume as being a cylinder with a diameter equal to the spot size ($0.7 \mu\text{m}$) and a length equal to the depth of focus ($1.7 \mu\text{m}$), the sample volume is $0.654 \mu\text{m}^3$, which is 2.93×10^{-15} times smaller than the Aerosil's sample volume.

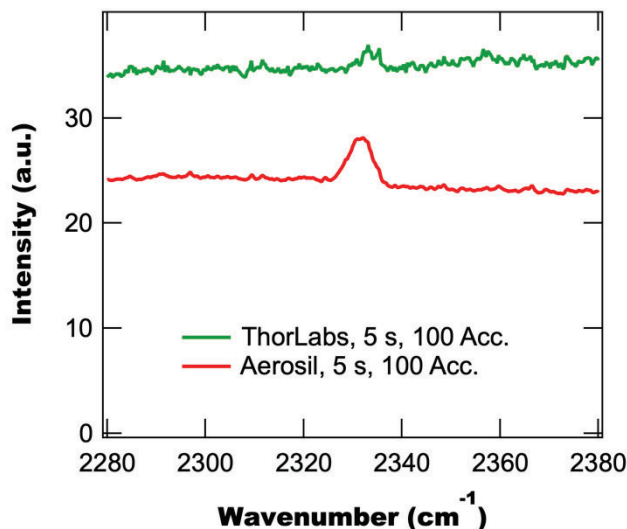


Figure 90. Comparison of nitrogen peaks measured using Thorlabs Spectralon cavity and our Aerosil cavity. Note that while the Aerosil cavity appears to have a better signal to noise ratio than the Thorlabs cavity, its volume is also 3.25 times larger, which means that there is more air (sample) in the cavity.

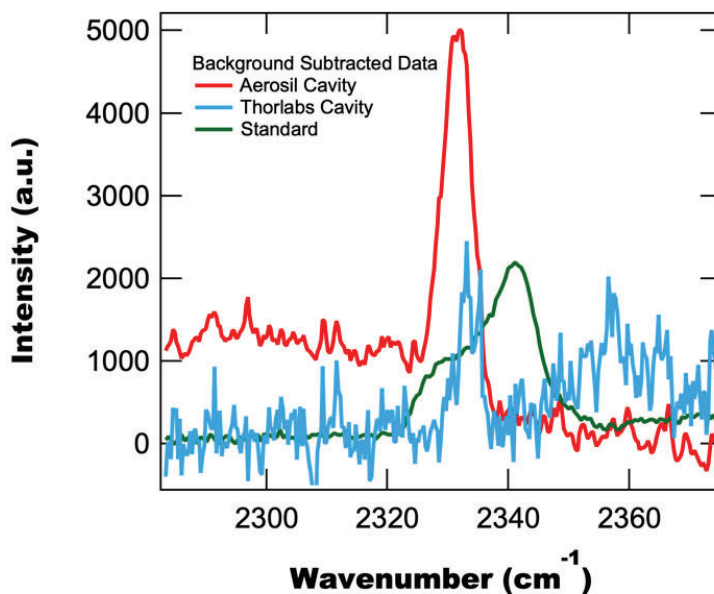


Figure 91. Comparison of background subtracted nitrogen peaks for Aerosil and Thorlabs cavity as well as in a standard spectrometer. Note that while the cavity measurements used the same spectrometer, the standard measurements used a different spectrometer, so direct comparisons are not easy.

As a further test of the cavity using 532 nm excitation, we performed measurements on BaSO₄ placed in a quartz crucible inside of the cavity and using a standard Raman spectrometer. Figure 90 shows the spectra measured from the empty cavity, the cavity containing sample, their difference, and the spectra from the standard Raman spectrometer. From Figure 92 we find that we do observe signal from the BaSO₄ in the cavity, though it is weak and almost 10 times smaller than the background. Additionally, it is not as clear

as the spectrum measured by the standard Raman spectrometer. Note that for these measurements we used the same power and spectrometer.

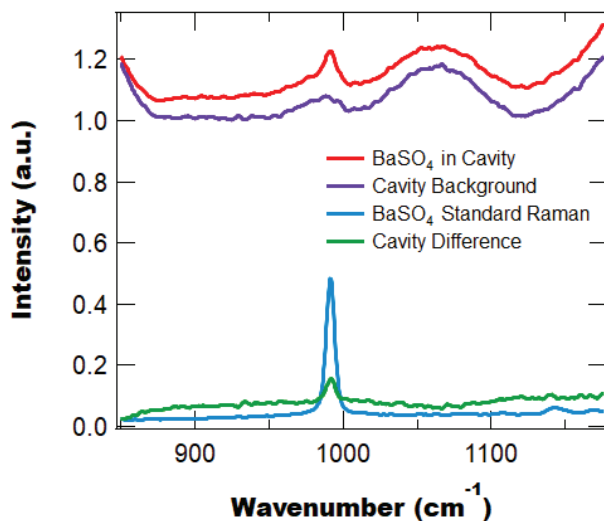


Figure 92. Raman spectra measured from different configurations. The cavity difference spectrum is determined by subtracting the BaSO₄ spectra from the background measurements.

As there is a large background in the cavity, which needs to be removed to obtain a sample's spectrum, it is necessary to be able to obtain a good repeatable background measurement. To test the reproducibility of the background we take the cavity apart five times and reassemble it and then measure the background spectra, which are normalized and shown in Figure 93. From the figure we find that the backgrounds are not consistent from run-to-run, which presents a significant problem for the usefulness of the cavity in measuring small signals.

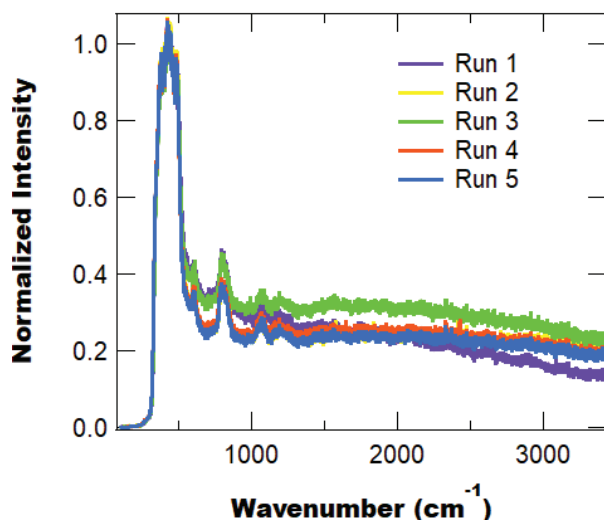


Figure 93. Comparison of cavity background for 5 different assemblies.

Cavity Work

During this reporting period we returned to working on the cavity fluorescence issue, which we previously identified as being due to the Thorlabs lenses. To demonstrate this again we measured the cavity emission both with and without the cavity lenses in place, with the spectra shown in Figure 94. From Figure 94 we see an emission peak at about 378 nm that clearly comes from the Thorlabs lenses.

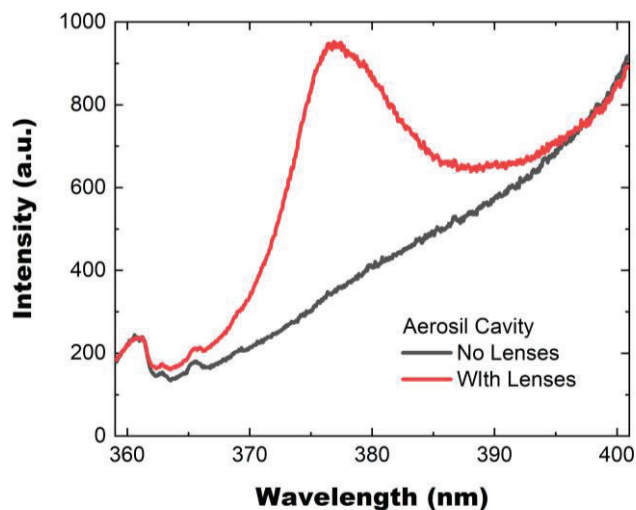


Figure 94. Emission from NIJ cavity both with and without Thorlabs lenses.

To address the issue of the emission from the Thorlabs lenses we purchased similar lenses from alternative vendors (Edmund Optics and Newport) and found that the lenses from Newport still display a broad fluorescence, but do not have a similar peak, which was the primary issue with the Thorlabs lenses. Figure 95 shows example PL spectra from both the Thorlabs lenses and Newport lenses and demonstrates the superior performance of the Newport lenses.

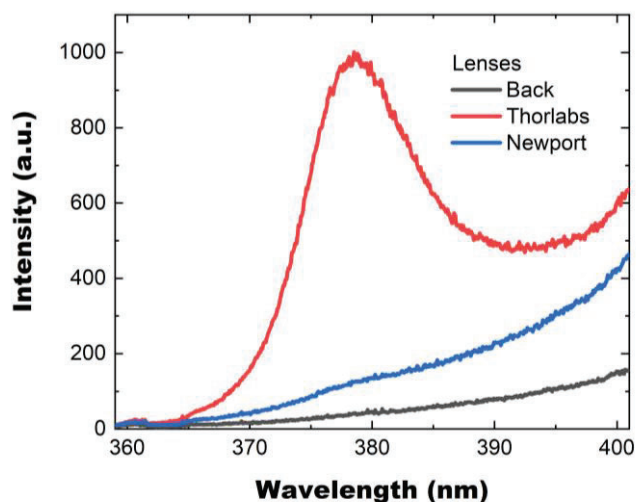


Figure 95. Comparison of emission from lenses from different vendor.

While the coupling lenses were determined to be the main challenge with regards to background, we also revisited our measurements of the Aerosil material at different levels of production: green body pellet, sintered, and sintered and endmilled, with Figure 96 showing the emission spectra. From Figure 96 we find that the green body has significant emission and a peak near 395 nm, which most likely arises due to the

use of polymeric binder in the Aerosil. After sintering the pellet loses the majority of its emission, however end milling seems to return some emission. It is not clear if this is due to contamination from the mill or if it is related to the surface quality difference between the two pellets.

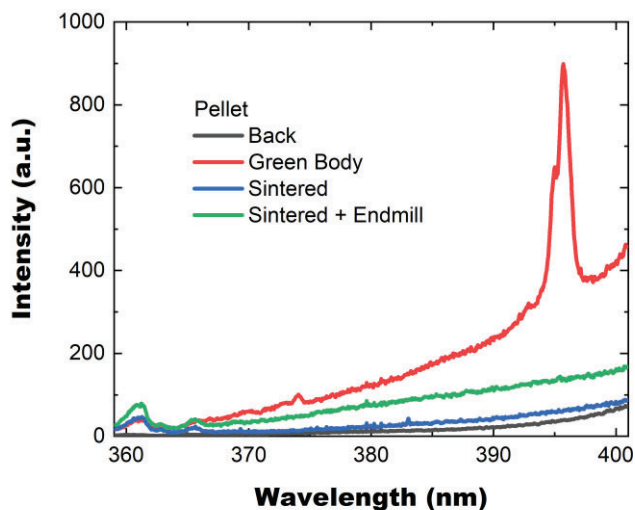


Figure 96. Emission from different Aerosil pellets.

Cavity Top Design

For the current reporting period we began our cavity work by setting up a new lens tube system for coupling out of the cavity using the Newport lenses and better alignment. While these changes improved our acceptance angle, we surprisingly found that the throughput is worse. As a demonstration we measured fluorescence from a dye-doped polymer in the cavity with different lens configurations, with the resulting spectra shown in Figure 97. From Figure 97 we find that sticking the fiber directly into the cavity and using a coupling lens have approximately the same intensity, while using the concave lens stack (which increases the acceptance angle) is found to lower the measured intensity. This is surprising as we would expect the greater acceptance angle to achieve greater throughput, however this is not the case. Therefore, we have removed the lens stack for the remaining cavity work.

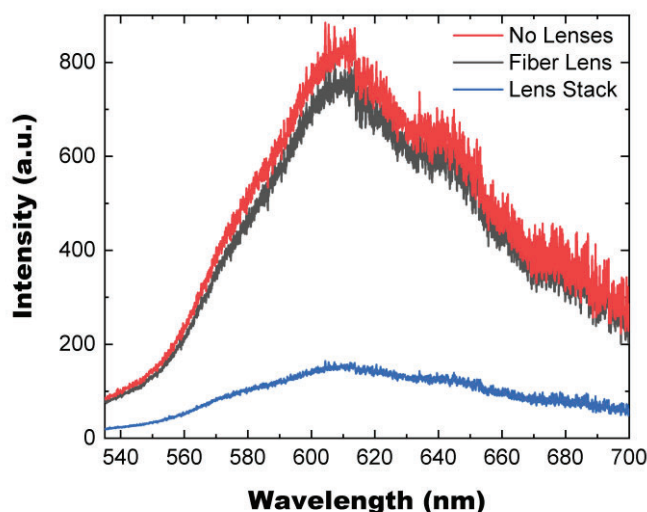


Figure 97. Fluorescence spectra of dye-doped polymer with different lens configurations.

Reconditioning Cavity

After working on the cavity top design, we next checked the cavity's reflectivity as the cavity has been sitting in open air for some time and collected some dust contamination and may have absorbed some water. Doing so we found that the reflectivity dropped to $R = 98.600 \pm 0.070$, which is below the 99% reflectivity threshold we determined for sufficient cavity enhancement. Given the observed decrease in reflectivity we next cleaned and baked out the cavity, which resulted in improved reflectivity $R = 99.460 \pm 0.065$. See Figure 98 for a comparison of ringdown pulses before and after reconditioning of the cavity.

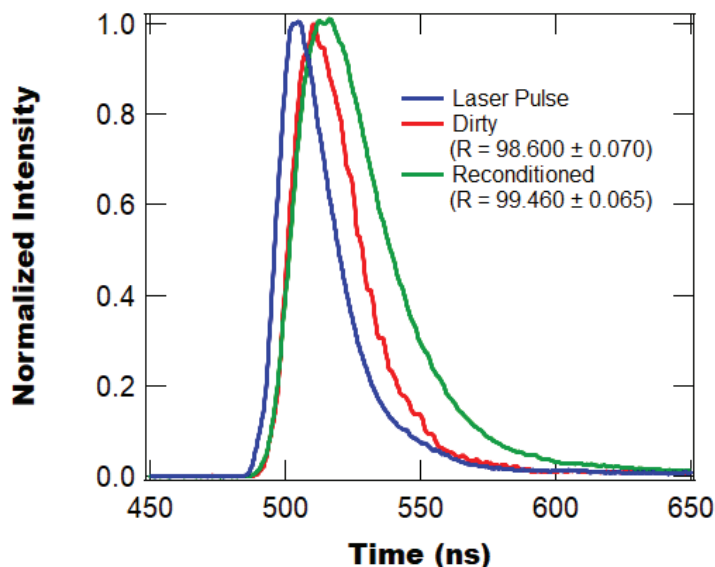


Figure 99. Comparison of ringdown measurements before and after cavity reconditioning.

Influence of Fiber Raman Scattering

Given the continued challenges with background in the integrating cavity we decided to revisit the influence of Raman scattering in the input/output fibers. Both fibers are made of fused silica and are found to display typical fused silica Raman spectra (see Figure 100) ²³.

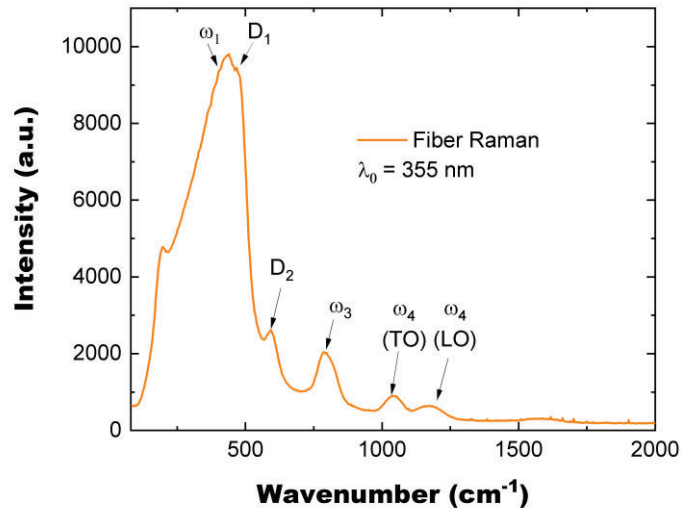


Figure 100. Raman spectrum from input fiber which displays all the typical features of fused silica ²³.

When measuring the Fiber's Raman spectra directly out of the fiber, we find significant intensity due to the geometry. However, determining how the fibers Raman spectrum contributes to the spectra measured by the cavity is difficult as the cavity is also made of silica, so both spectra are essentially the same. To differentiate the contribution of the fibers vs the contribution of the cavity we performed measurements where we used no filters, one longpass filter on the output and a bandpass filter on the input and a longpass filter on the output. Note that for these measurements we included a crucible of sugar water as this in theory should provide a reference Raman signal to scale the total intensity of our measurements. In this way we are able to remove the contributions of the fibers from the measured spectra. Figure 101 shows the resulting Raman spectra scaled such that the intensities of the sugar's Raman peaks are the same for all three configurations.

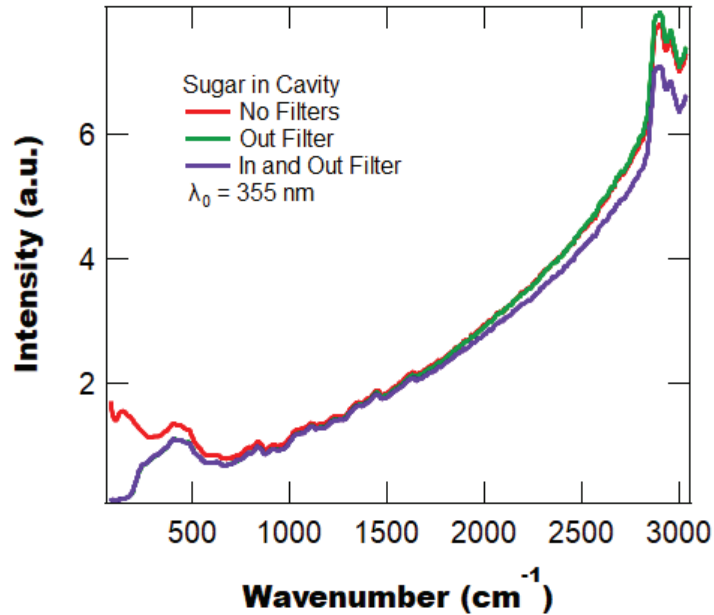


Figure 101. Raman spectra of sugar water in cavity with either no filters, 355 nm notch filter on output fiber, or a 355 nm bandpass filter on the input fiber and 355 nm longpass filter on output fiber.

From Figure 101 we find that the addition of the longpass filter in the output fiber removes signal from the low wavenumber region while not having much of an impact on the rest of the spectrum (as expected). With the inclusion of the filter on the incident fiber we see a small change in the spectra, but not a large enough difference to conclude that the incident fibers Raman scattering is causing significant interference. Instead, it looks like there is not much coupling of Raman signal from the incident fiber to the output fiber, this suggests that the majority of the signal from the empty cavity is due to Raman scattering from the cavity material, and not due to the input/output fiber.

iCERS of Dyed Fabrics

After working through the cavity fluorescence issue and finding a satisfactory cavity configuration we next attempted iCERS measurements of dyed fabrics using both 532 nm and 355 nm excitation. Figure 102 shows the resulting raw spectra for both excitation wavelengths with the cavity empty, with neat nylon, with AY049-dyed nylon, and with AR337-dyed nylon. Note that the nylon samples were small 1 cm x 1 cm swatches of fabric.

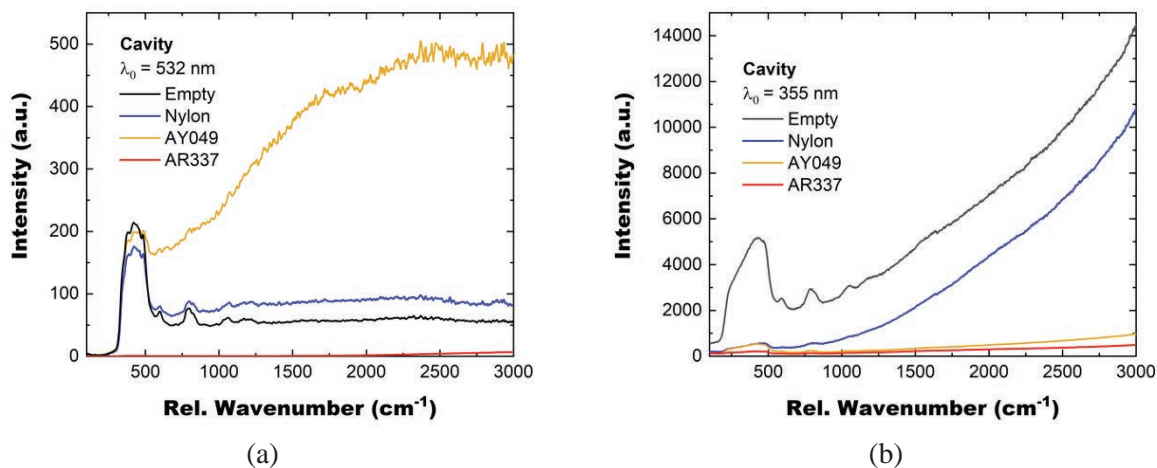


Figure 102. Raw Raman spectra of various fibers in cavity for 532 nm (a) and 355 nm (b) excitation.

From Figure 102a we find that when using 532 nm excitation the empty cavity and cavity with neat nylon have similar spectra, which are primarily attributed to the fused silica material of the cavity. In the case of AY049-doped nylon we find a strong fluorescence signal that overwhelms any Raman signal, which is similar to standard Raman measurements. On the other hand, the cavity with AR337-dyed nylon has barely any signal, which we attribute to its strong absorption at 532 nm. Since the AR337 absorbs strongly at 532 nm we do not obtain significant cavity enhancement as the light is quickly absorbed by the fabric. On the other hand, the AY049 (which has little absorbance at 532 nm) does display some cavity enhancement. However, we run into the same issue as with the standard Raman spectroscopy setup where the fluorescence overwhelms the Raman signal.

Moving onto 355 nm excitation, from Figure 102b we find that both dyed fibers have little signal and that even the neat nylon reduces the signal from the empty cavity. This is due to both dyes and the nylon material itself absorbing at 355 nm, which “snuffs out” any possible cavity enhancement. From these measurements it is clear that the iCERS scheme will not work with absorbing materials. Note that we could avoid the absorption of these materials by moving to the NIR, but we then run into the problem of the cavity material’s reflectivity being too poor to obtain enhancement. In order to make this experiment work in the NIR we would need a new cavity material.

iCERS of Transparent Materials

Given the failure of the iCERS technique with the dyed fabrics, we decided to test the technique with transparent materials to make sure that our cavity was working appropriately. For this purpose, we used sugar water at two different concentrations: 30% and 3%. The resulting background subtracted spectra are shown in Figure 103 for both the cavity measurement and a measurement using a standard Raman system (both at 355 nm). From Figure 103 we find that there is significant improvement in the signal for the cavity measurements as we have had to amplify standard system’s spectra to clearly display both curves on the

same scale. Based on these results it appears that the iCERS technique could be a useful spectroscopic technique for non-absorbing samples. However, the introduction of absorption makes the technique no longer useful.

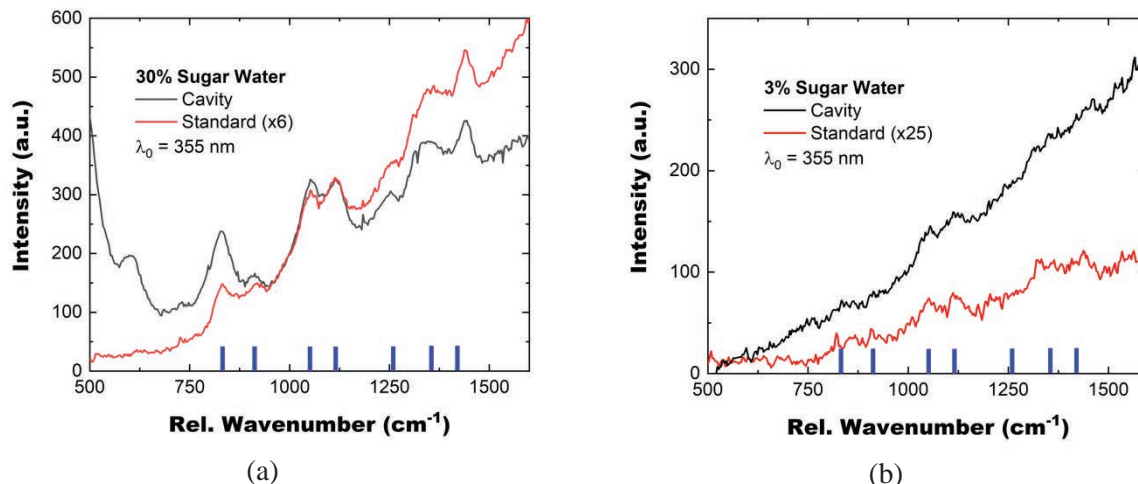


Figure 103. Comparison of standard and cavity Raman spectra for sugar water at 30% (a) and 3% (b) w/v concentration. Note that the cavity signal is significantly brighter demonstrating the cavity enhancement effect.

DUV Measurements

Given the challenges associated with the iCERS measurement with dyed fabrics, we also decided to test DUV Raman spectroscopy as another technique to obtain Raman spectra, while avoiding the fluorescence from the dyes. For this purpose, we tested two different 266 nm lasers: a pulsed ns OPO and the third harmonic from a tuned MIRA Ti-Sapphire oscillator. Neither system is ideal for Raman measurements as the OPO's bandwidth at 266 nm is 7 cm^{-1} (210 GHz) and the femtosecond third harmonic's bandwidth is 70 cm^{-1} (2.1 THz), whereas the CW green laser we use has a bandwidth of $<5 \text{ MHz}$. However, these are the systems we have available in this wavelength range and therefore they are the lasers we have to work with.

To get a sense of how the Raman spectra look using 266 nm excitation and the broader bandwidths, we measure Raman spectra of both BaSO_4 and Spectralon with the resulting spectra shown in Figure 104. From Figure 104 we find that the OPO allows for enough resolution to discern the individual peaks of the materials, however for the MIRA the peaks are merged together due to the broad bandwidth of the laser.

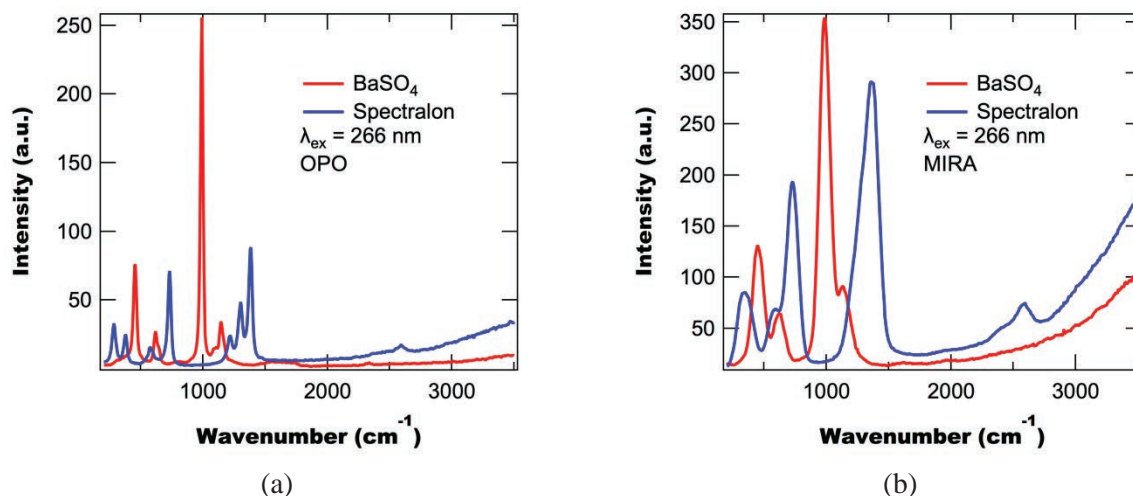
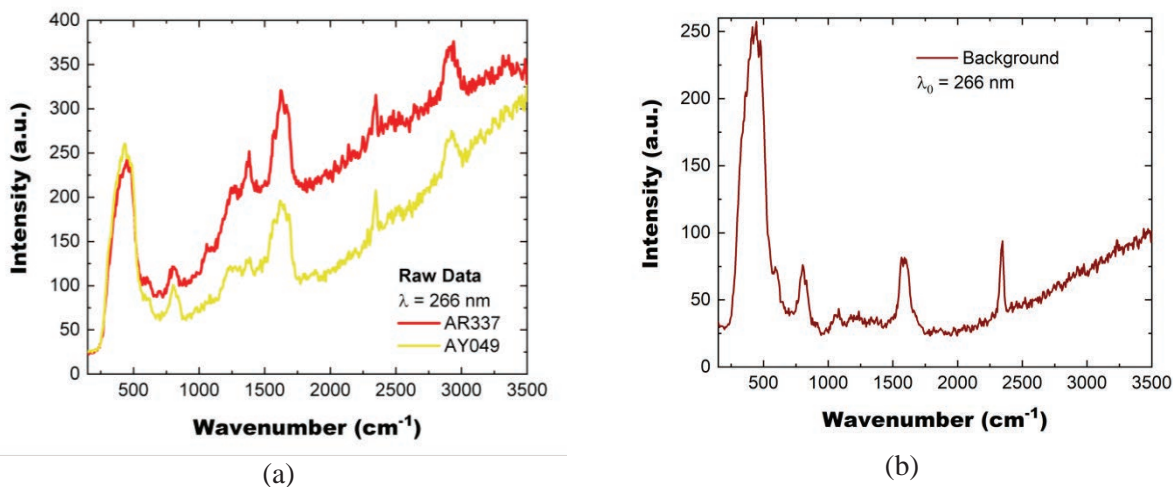
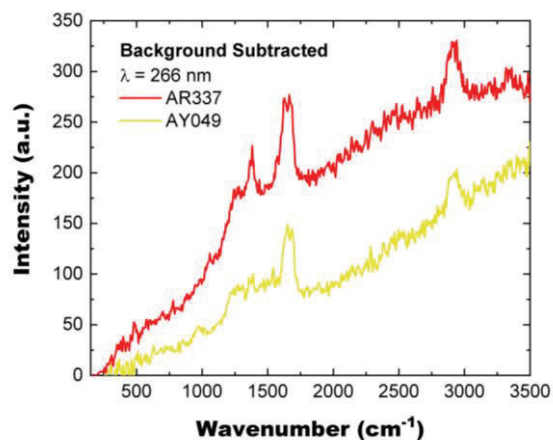


Figure 104. DUV Raman spectra of reference materials using OPO (a) and THG from MIRA (b). The peaks using the MIRA laser system are significantly broadened due the laser being a femtosecond system.

Pulsed DUV Raman

Having tested both DUV lasers with Raman reference materials, we next measured the dyed-fiber samples. Figure 105a shows the raw Raman spectra measured from the fibers, which displays multiple peaks not associated with the dyed fibers. To better understand the source of these peaks we performed measurements without the fibers, with the resulting spectrum shown in Figure 105b. The peaks in Figure 105b can be attributed to either UV Fused Silica (which makes up the optics) or atmospheric oxygen ($\sim 1555\text{ cm}^{-1}$) and nitrogen ($\sim 2400\text{ cm}^{-1}$).





(c)

Figure 105. Raw (a), background (b), and background subtracted (c) Raman spectra from dye-doped nylon using 266 nm excitation.

We next calculate the background subtracted spectra from the fibers, which are shown in Figure 105c. Looking at the spectra in Figure 105c we do not see any of the expected peaks for the dye-doped fibers and instead see other peaks, including: several broad peaks in the 1250 cm^{-1} to 1500 cm^{-1} range, a peak at $\sim 1670 \text{ cm}^{-1}$ that could be due to an amide group (N-C=O), and a peak near 2900 cm^{-1} that corresponds to the nylon. Given the observation of the peak $\sim 1670 \text{ cm}^{-1}$, we may be measuring the products of the dyes photobleaching via photooxidation (hence the C=O bond). In this case the broad peaks in the 1250 cm^{-1} to 1600 cm^{-1} then would correspond to the photodegraded dye with possible bonds being: C=C, C-H₂, and C-H₃.

DUV Background

As mentioned above our pulsed DUV measurements display Raman signal originating from the UVFS optics and the air, both of which are typically not observed in our standard Raman measurements. These differences could be due to the change in wavelength, change to pulsed excitation, or a combination of both. To better understand the underlying mechanisms, we next tested the pulsed setup using 532 nm light, with Figure 106 comparing the background Raman spectra for 266 nm and 532 nm pulsed excitation. From Figure 106 we find that the 532 nm measurement also displays the UVFS peaks, but not the atmospheric peaks. We hypothesize that the difference is due to the 266 nm resonantly interacting with the atmospheric oxygen and nitrogen, whereas the 532 nm light does not. These results suggest that the signal from the UVFS optics is arising due to the pulsed measurements, while the atmospheric signal is due to the change in wavelength.

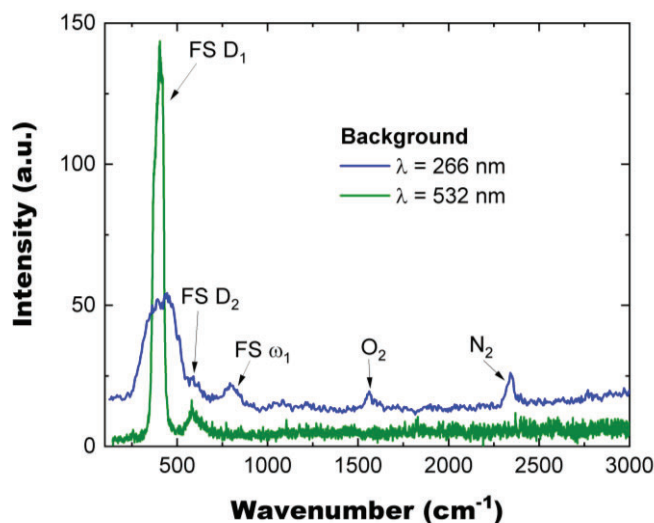


Figure 106. Comparison of background measurements using different excitation wavelengths.

Quasi-cw DUV Raman

Given the high probability that the pulsed DUV laser photobleaching the dyed fibers during measurement, we next try using the frequency tripled MIRA oscillator, which has lower powers than the OPO. Note that the OPO has a peak power of ~ 1 MW and an average power of 100 mW, whereas the MIRA has a peak power of ~ 526 W and an average power of 5 mW.

We first measured the background spectrum using the MIRA, with the resulting spectrum shown in Figure 107. From Figure 107 we observe a similar background spectrum to the OPOs spectrum, with peaks due to atmospheric gases and the UV Fused Silica optics.

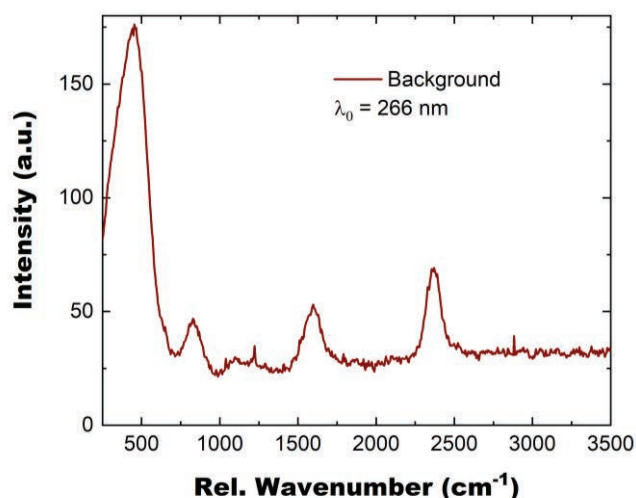


Figure 107. Background measured using MIRA third harmonic at 266 nm.

After measuring the background, we next measured the dye-doped nylon the MIRA, with Figure 108a showing the resulting baseline-subtracted spectra. From Figure 108a we find that all three spectra look very

similar, despite being different materials. Due to this observation, we initially theorized that the nylon fiber's Raman was overwhelming the signal from the dye (thereby making them all look the same). However, we then measured the dye powder (see Figure 108b) and find that the spectra still look very similar (minus the nylon peak near 1900 cm^{-1}).

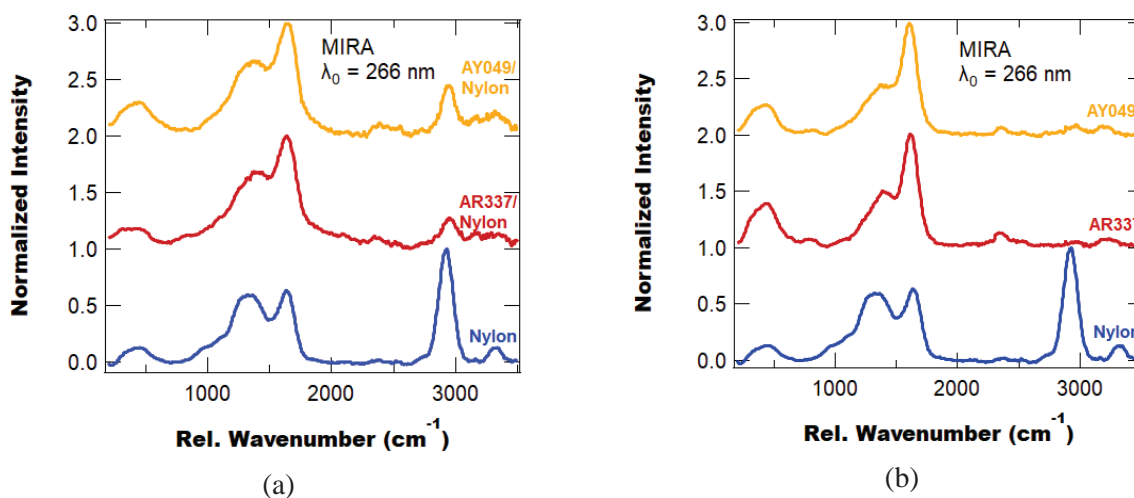
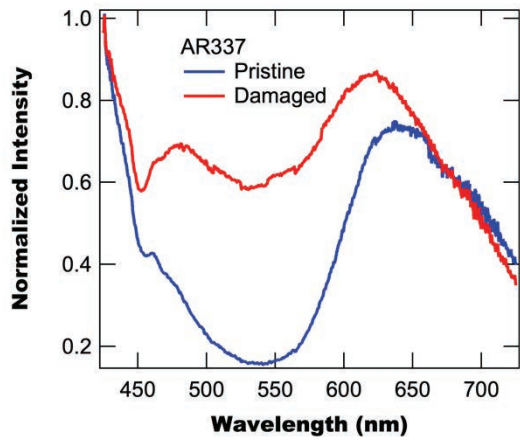


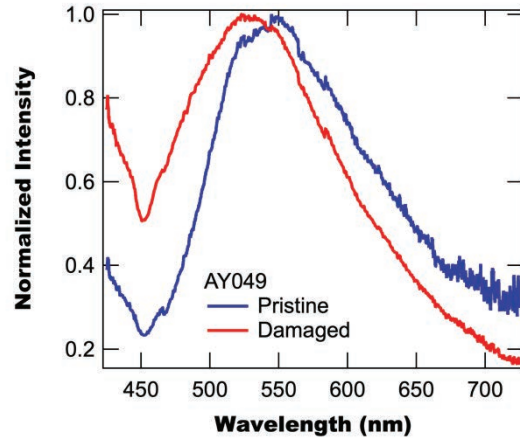
Figure 108. DUV Raman spectra of nylon fibers (a) and dye powders (b) with clean nylon's spectra for reference.

The similarity of the DUV Raman spectra for all the materials below 2000 cm^{-1} is unexpected and does not have a clear explanation at this time. One hypothesis is that the DUV wavelength is damaging the dyes and nylons in such a way that the resulting products have similar Raman spectrum, at least within the limited resolution of these measurements. Note that we attempted to perform higher resolution measurements on the damaged fabrics using 355 nm and 532 nm excitation, but neither wavelength produced a noticeable Raman signal. It appears that the damaged products have resonance enhancement with 266 nm excitation, but not with 355 nm nor 532 nm.

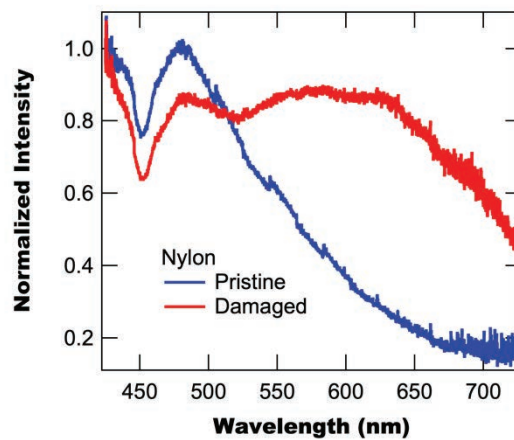
While we were unable to observe Raman peaks from the damaged fabrics using 355 nm, we were able to observe changes in their fluorescence. In general, the damaged fabrics displayed greater fluorescence intensity and broader emission peaks. Figure 109 displays the normalized fluorescence intensity from the both the pristine and damaged fabrics to demonstrate how the spectral shapes change.



(a)



(b)



(c)

Figure 109. Comparison of fluorescence from pristine and photodamaged fabrics for AR337-dyed nylon (a), AY049-dyed nylon (b) and neat nylon (c).

REFERENCES

1. Trace Evidence. <https://www.nij.gov/topics/forensics/evidence/trace/pages/welcome.aspx?tags=trace> (accessed 03/12/2018).
2. Deedrick, D. W. Forensic Science Communications, Hairs, Fibers, Crime, and Evidence Part 2: Fiber Evidence. <https://archives.fbi.gov/archives/about-us/lab/forensic-science-communications/fsc/july2000/deedric3.htm> (accessed 3/26/2018).
3. Goodpaster, J. V.; Liszewski, E. A., Forensic analysis of dyed textile fibers. *Analytical and Bioanalytical Chemistry* **2009**, 394 (8), 2009-2018.
4. Buzzini, P., The characterization of textile fibers and other miscellaneous trace materials. In *Annual Meeting of the American Forensic Society*, Seattle, 2018.
5. Buzzini, P.; Massonnet, G., The Analysis of Colored Acrylic, Cotton, and Wool Textile Fibers Using Micro-Raman Spectroscopy. Part 2: Comparison with the Traditional Methods of Fiber Examination. *J Forensic Sci* **2015**, 60 (3), 712-720.
6. Massonnet, G.; Buzzini, P.; Monard, F.; Jochem, G.; Fido, L.; Bell, S.; Stauber, M.; Coyle, T.; Roux, C.; Hemmings, J.; Leijenhorst, H.; Van Zanten, Z.; Wiggins, K.; Smith, C.; Chabli, S.; Sauneuf, T.; Rosengarten, A.; Meile, C.; Ketterer, S.; Blumer, A., Raman spectroscopy and microspectrophotometry of reactive dyes on cotton fibres: Analysis and detection limits. *Forensic Sci Int* **2012**, 222 (1-3), 200-207.
7. Robertson, J.; Roux, C.; Wiggins, K. G., *Forensic examination of fibres*. CRC Press: 2017.
8. Burnip, M. R. Forensic Characterization of Dyes from Synthetic Textile Fibers exposed to outdoor and laundering effects by ultra-performance liquid chromatography and spectral analysis. University of South Carolina, University of South Carolina, 2016.
9. Dockery, C. R.; Stefan, A. R.; Nieuwland, A. A.; Roberson, S. N.; Baguley, B. M.; Hendrix, J. E.; Morgan, S. L., Automated extraction of direct, reactive, and vat dyes from cellulosic fibers for forensic analysis by capillary electrophoresis. *Analytical and Bioanalytical Chemistry* **2009**, 394 (8), 2095-2103.
10. Morgan, S. L. *Validation of Forensic Characterization and Chemical Identification of Dyes Extracted from Millimeter-length Fibers*; Department of Chemistry and Biochemistry, University of South Carolina: 2015.
11. Stefan, A. R.; Dockery, C. R.; Baguley, B. M.; Vann, B. C.; Nieuwland, A. A.; Hendrix, J. E.; Morgan, S. L., Microextraction, capillary electrophoresis, and mass spectrometry for forensic analysis of azo and methine basic dyes from acrylic fibers. *Analytical and Bioanalytical Chemistry* **2009**, 394 (8), 2087-2094.
12. Stefan, A. R.; Dockery, C. R.; Nieuwland, A. A.; Roberson, S. N.; Baguley, B. M.; Hendrix, J. E.; Morgan, S. L., Forensic analysis of anthraquinone, azo, and metal complex acid dyes from nylon fibers by micro-extraction and capillary electrophoresis. *Analytical and Bioanalytical Chemistry* **2009**, 394 (8), 2077-2085.

13. Abbott, L. C.; Batchelor, S. N.; Smith, J. R. L.; Moore, J. N., Resonance Raman and UV-visible spectroscopy of black dyes on textiles. *Forensic Sci Int* **2010**, *202* (1-3), 54-63.
14. Buzzini, P.; Massonnet, G., The Discrimination of Colored Acrylic, Cotton, and Wool Textile Fibers Using Micro-Raman Spectroscopy. Part 1: In situ Detection and Characterization of Dyes. *J Forensic Sci* **2013**, *58* (6), 1593-1600.
15. Lepot, L.; De Wael, K.; Gason, F.; Gilbert, B., Application of Raman spectroscopy to forensic fibre cases. *Sci Justice* **2008**, *48* (3), 109-117.
16. Massonnet, G.; Buzzini, P.; Jochem, G.; Stauber, M.; Coyle, T.; Roux, C.; Thomas, J.; Leijenhurst, H.; Van Zanten, Z.; Wiggins, K.; Russell, C.; Chabli, S.; Rosengarten, A., Evaluation of Raman Spectroscopy for the analysis of colored fibers: A collaborative study. *J Forensic Sci* **2005**, *50* (5), 1028-1038.
17. Massonnet, G.; Buzzini, P.; Monard, F.; Jochem, G.; Fido, L.; Bell, S.; Stauber, M.; Coyle, T.; Roux, C.; Hemmings, J.; Leijenhurst, H.; Van Zanten, Z.; Wiggins, K.; Smith, C.; Chabli, S.; Sauneuf, T.; Rosengarten, A.; Meile, C.; Ketterer, S.; Blumer, A., Raman Spectroscopy and Microspectrophometry of reactive dyes on cotton fibres-Analysis and detection limits. *Forensic Sci Int* **2012**, *222*, 200-207.
18. Was-Gubala, J.; Starczak, R., Nondestructive Identification of Dye Mixtures in Polyester and Cotton Fibers Using Raman Spectroscopy and Ultraviolet-Visible (UV-Vis) Microspectrophotometry. *Appl. Spectrosc.* **2015**, *69* (2), 296-303.
19. Anderson, B. R.; Gunawidjaja, R.; Eilers, H., Photodegradation and self-healing in a Rhodamine 6G dye and Y2O3 nanoparticle-doped polyurethane random laser. *Appl Phys B-Lasers O* **2015**, *120* (1), 1-12.
20. Thomas, J.; Buzzini, P.; Massonnet, G.; Reedy, B.; Roux, C., Raman spectroscopy and the forensic analysis of black/grey and blue cotton fibres - Part 1. Investigation of the effects of varying laser wavelength. *Forensic Sci Int* **2005**, *152* (2-3), 189-197.
21. Bixler, J. N. Integrating Cavity Enhanced Spectroscopy for Liquid and Gas Sensing . Texas A&M, 2015.
22. Cone, M. T. A New Diffuse Reflecting Material with Applications including Integration Cavity Ring-Down Spectroscopy. Texan A&M, Texan A&M, 2014.
23. Little, D. J.; Ams, M.; Dekker, P.; Marshall, G. D.; Dawes, J. M.; Withford, M. J., Femtosecond laser modification of fused silica: the effect of writing polarization on Si-O ring structure. *Opt Express* **2008**, *16* (24), 20029-37.